

**Search for a variation of the proton–electron mass ratio
from molecular hydrogen and methanol**

VRIJE UNIVERSITEIT

**Search for a variation of the proton–electron mass ratio
from molecular hydrogen and methanol**

ACADEMISCH PROEFSCHRIFT

ter verkrijging van de graad Doctor aan
de Vrije Universiteit Amsterdam,
op gezag van de rector magnificus
prof.dr. F.A. van der Duyn Schouten,
in het openbaar de verdedigen
ten overstaan van de promotiecommissie
van de Faculteit der Exacte Wetenschappen
op dinsdag 7 april 2015 om 13.45 uur
in de aula van de universiteit,
De Boelelaan 1105

door

Julija Bagdonaitė

geboren te Vilnius, Litouwen

promotoren: prof.dr. W.M.G. Ubachs
prof.dr. L. Kaper
copromotor: prof.dr. M.T. Murphy

This thesis was approved by the members of the reviewing committee:

dr. H.L. Bethlem (Vrije Universiteit Amsterdam)
prof.dr. E.F. van Dishoeck (Sterrewacht Leiden)
prof.dr. P. Molaro (Astronomical Observatory Trieste, Italy)
prof.dr. F.F.S. van der Tak (Universiteit Groningen)
prof.dr. R.A.M.J. Wijers (Anton Pannekoek Instituut)



The work described in this thesis was carried out at the VU University Amsterdam and was supported by the Foundation for Fundamental Research on Matter (FOM), which is part of the Netherlands Organisation for Scientific Research (NWO).

The cover of this thesis is based on an image of the molecular cloud IRAS 16562–3959. Credit: ESO/VVV Team/A. Guzmán.
Digital design by T. D. Rotteveel and J. Bagdonaitė.

ISBN: 978-94-6259-593-4

Printed by: Ipskamp Drukkers B.V.

Contents

1	Introduction	1
1.1	Fundamental constants	2
1.2	Current theories of varying fundamental constants	2
1.3	Local constraints	4
1.4	Astronomical constraints	5
1.5	Outline of thesis	16
2	Constraint on a variation of the proton-to-electron mass ratio from H₂ absorption toward quasar Q2348–011	19
2.1	Introduction	20
2.2	Data	21
2.3	The comprehensive fitting method	22
2.4	Analysis	23
2.5	Conclusions	32
3	Analysis of H₂ absorption toward QSO B0642–5038 for a varying proton-to-electron mass ratio	33
3.1	Introduction	34
3.2	Method	36
3.3	Data	40
3.4	Analysis	41
3.5	Systematic uncertainty	51
3.6	Discussion	58
4	Constraint on a varying proton–electron mass ratio 1.5 billion years after the Big Bang	69
5	Limits on a gravitational field dependence of the proton–electron mass ratio from H₂ in white dwarf stars	91
6	A stringent limit on a drifting proton-to-electron mass ratio from alcohol in the early universe	105

CONTENTS

7 Robust constraint on a drifting proton-to-electron mass ratio at $z = 0.89$ from methanol observation at three radio telescopes	115
Bibliography	127
Publication list	145
Summary	147
Samenvatting	151
Acknowledgments	155

Introduction

For a long time scientific thought has been strongly rooted in a notion that the laws of nature are universally immutable: they are the rules responsible for the evolution of every part of the universe but they are never a subject to a change themselves. The immutability of physical laws can be tested via the so-called fundamental constants that appear in those laws. These constants are regarded as fundamental because they can only be measured, and there is no operational theory which would allow us to calculate their values. Thus, due to the lack of understanding of their origin, both the constants and the corresponding laws are most often regarded as invariable.

Back in 1937, Dirac was one of the first who started questioning whether the constants are simply mathematical numbers or if they can be decoded and understood within a context of a deeper cosmological theory [1]. This idea caused a stir among theorists that inspired and continues to inspire diverse proposals as to which of the constants are fundamental, why they should or should not vary, and what are the cosmological consequences of their possible variation. Several important milestones were achieved in the domain of observational astrophysics, such as establishing the alkali-doublet method to probe the constancy of the fine structure constant α [2], followed by the more general and more accurate many-multiplet method [3, 4]. Moreover, in 1975, Thompson suggested that the wavelengths of molecular hydrogen transitions could be used to probe a possible variation of the ratio of proton–electron inertial mass [5]. The development of the 8-10 m class optical telescopes constituted an instrumental basis required to implement the aforementioned methods in extragalactic studies. Today, given the substantial body of theoretical and experimental work produced over the past couple of decades, the immutability of physical laws hardly classifies as an axiom anymore, but rather is a testable scientific question with exciting implications.

1.1 Fundamental constants

The main focus of this thesis is on a variation of the proton–electron mass ratio μ , whose value from local experiments is known with a 4×10^{-10} relative precision:¹

$$\mu \equiv \frac{m_{\text{p}}}{m_{\text{e}}} = 1836.152\,672\,45(75). \quad (1.1)$$

Since the gluon field that binds quarks inside the proton is responsible for most of its mass, the μ constant is sensitive to the ratio of the chromodynamic scale with respect to the electroweak scale [7]. Another fundamental constant often targeted as a testground for detecting variations is the fine-structure constant α that sets the electrodynamic scale:¹

$$\alpha \equiv \frac{e^2}{4\pi\epsilon_0\hbar c} = \frac{1}{137.035\,999\,074(44)}. \quad (1.2)$$

The standard model of particle physics contains the following constants: 3 gauge couplings, 2 Higgs parameters, including the Higgs mass and Higgs vacuum expectation value, 6 quark masses, 3 quark mixing angles, 1 imaginary quark phase, 3 lepton masses, 1 strong charge parity parameter, and up to 9 more parameters if massive neutrinos are included. Unrelated to the standard model, the cosmological constant Λ and the gravitational constant G are also regarded as fundamental constants. For various reasons, dimensionless combinations of these constants are favored in experiments aimed to search for their variability (see e.g. [8]). Throughout this thesis, a definition of a relative change in μ is adopted via

$$\frac{\Delta\mu}{\mu} = \frac{\mu_z - \mu_{\text{lab}}}{\mu_{\text{lab}}}, \quad (1.3)$$

where μ_z refers to the proton–electron mass ratio in the probed system and μ_{lab} is a reference laboratory value. A positive $\Delta\mu/\mu$ indicates a larger μ in the probed system as compared to the laboratory value.

1.2 Current theories of varying fundamental constants

The concept of cosmologically varying constants can be found in at least two classes of theories: unification theories that include extra dimensions and theories embracing fundamental scalar fields. While the theories briefly outlined

¹From the CODATA 2010 release of the recommended values of the fundamental physical constants: <http://physics.nist.gov/cuu/index.html>; accessed in October 2014. A four-fold improvement over the precision of the current recommended value of μ was reported recently [6], leading to $\mu = 1836.152\,673\,77(17)$.

here primarily target the fine structure constant α , they usually predict a specific (model-dependent) relation between α and the variation of the proton–electron mass ratio μ [7, 9]. A more extensive overview of the theoretical studies of varying constants is provided in [10].

The first class of theories deals with bridging gravity with quantum mechanics by postulating additional spacetime dimensions. The Kaluza-Klein theory is known as the first unified field theory of electromagnetism and gravity [11, 12], which was formulated in 5 dimensions. It preceded a number of different string theories developed more recently, which can be formulated in as many as ten dimensions (see [13] for a broad overview). Our perceivable universe is 4-dimensional; thus, the extra dimensions must be very compact. Since the fundamental theory encompasses all the postulated dimensions, the conventional 4-dimensional theory is a consequence of the dimensional reduction. Thereby, the conventional constants appear as the projected effective parameters that depend on the multidimensional constants and on the scale length of the additional dimensions. The latter parameter may be easily varied within the context of cosmological evolution of the universe, resulting in variations of the effective constants. Since the same scale length affects all the effective constants, theoretical models predict correlations between variations of different constants – for example, in many models a variation in the fine structure constant α is linked to a variation in the gravitational constant G [14, 15]. It means that measuring variation of different 4-dimensional constants provides constraints on theories with extra dimensions.

The second class of theories was introduced with the work by Bekenstein [16], where a cosmological variation in the electric charge e is produced by an additional scalar field which is coupled to the matter density. A more general approach was proposed by Sandvik, Barrow, and Magueijo [17, 18], who created a self-consistent cosmological model with varying α . In this model, the scalar field is coupled to the matter energy density, and any substantial α changes are suppressed with the onset of dark energy domination. This allows one to reconcile stringent low redshift geophysical constraints with the indications of non-zero α obtained from quasar observations at medium-to-high redshifts. Barrow and Magueijo [19] developed a theory that, by inducing variations in the mass parameter for the electron, specifically addresses variation of μ . Constrained by the local tests of the weak equivalence principle of general relativity, the theory predicts that any μ variation at redshift $z \sim 1$ would be of the order of $< 10^{-9}$, which is still below the current best constraints [20, 21]. In all of these theories, variation of constants is driven by varying matter density in the universe. This led to developing the so-called chameleon scenarios where inhomogeneities in the constants could be observed by probing environments with very low local mass densities, with no variation of constants able to be measured in the high-density environment of Earth-based experiments [22, 23].

1.3 Local constraints

The local constraints on the fundamental constants include limits derived from laboratory, geophysical, and meteoritic measurements. Laboratory experiments mostly rely on atomic clocks where frequencies of two transitions are compared over a period of time, with the primary goal to set better frequency standards. A good control over most systematic effects is granted but the usual time base extends only over a couple of years and hence high sensitivity measurements are required to probe the oscillatory temporal and gradual spatial variations of fundamental constants [24, 25]. The best laboratory constraints on α and μ have been recently determined by measuring two optical transitions in $^{171}\text{Yb}^+$ ions [26] (also see a similar analysis where cesium clocks are used as a reference [27]). Assuming a linear drift rate, constraints of $\frac{\dot{\mu}}{\mu} = (-0.2 \pm 1.1) \times 10^{-16} \text{ yr}^{-1}$ and $\frac{\dot{\alpha}}{\alpha} = (-0.7 \pm 2.1) \times 10^{-17} \text{ yr}^{-1}$ were derived. However, in this measurement some model dependence remains as the nuclear magnetic moments were treated as constant to eliminate their codependence with μ . A model-independent μ constraint was derived from an experiment where a rovibrational transition in the SF_6 molecule was compared to a cesium clock over a time period of two years, resulting in $\frac{\dot{\mu}}{\mu} = (-3.8 \pm 5.6) \times 10^{-14} \text{ yr}^{-1}$ [28]. The best current model-free α constraint has been derived by comparing optical transitions in Hg^+ and Al^+ ions, which resulted in a drift rate of $\frac{\dot{\alpha}}{\alpha} = (-1.6 \pm 2.3) \times 10^{-17} \text{ yr}^{-1}$ [29].

Oklo is a uranium mine, located in Gabon, Central Africa, in which a natural nuclear reactor operated ~ 1.9 billion years ago (corresponding to a redshift of ~ 0.14). A rich uranium deposit was submerged in a flow of underground water which helped to sustain a nuclear chain reaction for several million years. To constrain a variation in α , the present day abundance ratio between ^{149}Sm and ^{150}Sm isotopes found at Oklo can be used since the rate of neutron capture depends on the value of α (although the dependence is not straightforward and thus the constraints are model-dependent). One of the most recent analyses resulted in a constraint on α variation of $-0.7 \times 10^{-9} < \frac{\Delta\alpha}{\alpha} < 1.0 \times 10^{-8}$ for a lookback time of 1.9 billion years [30].

Meteorite dating is another way of providing bounds on the variation of fundamental constants. In particular, a slight change in the fine structure constant can destabilize certain isotopes and hence one can extract limits on the time variation of α by comparing the decay rates from meteoritic samples to corresponding laboratory or geophysical values. Since formation of the meteorites dates back to the birth of the solar system, this method gives access to lookback times of 4–5 billion years or an average redshift of ~ 0.4 . For instance, the $^{187}\text{Re}/^{187}\text{Os}$ abundance ratio in iron meteorites has been analyzed to determine the radioactive lifetime of ^{187}Re , which resulted in a $|\Delta\alpha/\alpha|$ constraint of $< 3 \times 10^{-7}$ at redshift $z = 0.45$ [31].

1.4 Astronomical constraints

While the laboratory, geophysical, and meteoritic measurements result in accurate limits on varying fundamental constants, those measurements are temporally and spatially confined, in the best case, to the age and the extent of the solar system. Observations of distant quasars provide access to much earlier times, as well as to vastly different spatial locations and environmental conditions. An example of a quasar spectrum is shown in Fig. 1.1. Spectroscopic measurements of various molecular or atomic species detected in quasar sightlines provide a means to put constraints on a varying μ and α , respectively. Specific methods regarding variation of α include the alkali-doublet method [2, 32], and the many-multiplet method [3, 4, 33, 34]. The alkali-doublet method makes use of the fact that the relative wavelength spacing of the doublet is proportional to α^2 , while the many-multiplet model is a generalization of the former over many different atomic species. The many-multiplet method takes into account that the ground state levels have higher sensitivity to any variation in α when compared to excited levels, and that a wider range of sensitivity coefficients can be employed by comparing transitions in high- and low-mass ions. Several studies reported strong indications of a temporally and spatially varying α at the level of several parts per million [34, 35, 36]. However, these findings seem inconclusive as of yet, especially due to recently uncovered instrument-related systematic effects [37, 38].

Besides μ and α , various combinations of constants have been probed via spectroscopy of the extragalactic interstellar and/or intergalactic medium [10]. For example, by comparing the ultraviolet (UV) transitions of heavy elements with the hyperfine H I transition at a 21-cm rest wavelength allows to extract limits on $x = \alpha^2 g_p / \mu$, where g_p is the gyromagnetic factor of the proton [39]. To make such a comparison, one must take into account the fact that quasars can have frequency-dependent structure, which may result in different sightlines being probed at the UV/optical and radio wavelengths. An application of this particular method led to a $|\Delta x/x|$ constraint at the level of $\lesssim 1.7 \times 10^{-6}$ for redshift $z = 3.174$ [40]. In the following we discuss possibilities of putting limits on varying constants in the earliest stages of the universe and methods that pertain exclusively to variation of μ .

Early universe constraints

The highest redshift constraints on the fundamental constants come from the cosmic microwave background (CMB) radiation and the Big Bang nucleosynthesis (BBN). The CMB radiation consists of photons that were last scattered when the universe was 380 000 years old ($z \sim 1100$). The hot plasma of electrons and protons then cooled, recombined, and became transparent for the

photons to travel freely. The present day CMB is an almost perfect fit to a black-body model of $T_{\text{CMB}} = 2.723$ K, with anisotropies of the order of μK . It appears that these anisotropies depend on the gravitational constant G , the fine-structure constant α , and the mass of the electron, m_e [10]. Constraints of the order of $< 1 \times 10^{-3}$ have been derived on the relative variation of α and m_e based on the data of the Wilkinson Microwave Anisotropy Probe [41].

The BBN refers to the process of light element production in the early universe ($z \sim 10^8$). In fact, all of the elements heavier than lithium and beryllium were created through the process of stellar nucleosynthesis which started happening much later. The theory of BBN yields quantitative predictions for the abundances of deuterium, helium-3, helium-4, and lithium-7, which are compared against the corresponding abundances measured in isolated chemically unevolved interstellar clouds. One of the more notable discrepancies between the BBN theory and spectroscopic observations – the overprediction of the abundance of lithium-7 – has been considered in the context of varying

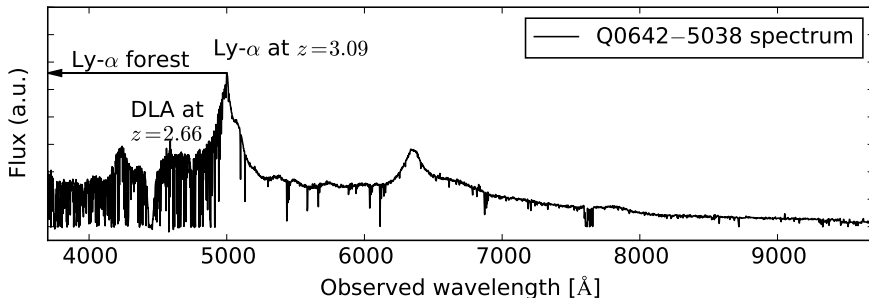


Figure 1.1: The optical spectrum of a quasar at $z = 3.09$ obtained by the Ultraviolet and Visual Echelle Spectrograph (UVES) mounted at the ESO Very Large Telescope (VLT). The quasar spectrum includes the characteristic broad emission line profiles produced by e.g. Lyman- α of H I, and C IV. The Lyman- α forest arises as the light from the quasar crosses multiple neutral hydrogen clouds/galaxies lying in the line of sight. A damped Lyman- α system at $z_{\text{DLA}} = 2.66$ causes a series of very strong absorption lines starting at $(z_{\text{DLA}} + 1) \times 1216 \text{ \AA} = 4450 \text{ \AA}$, and absorbs all the flux at $< (z_{\text{DLA}} + 1) \times 912 \text{ \AA} = 3340 \text{ \AA}$ producing a so-called Lyman break (outside the range of this plot). Since the rest wavelengths of H₂ are in the UV ($< 1114 \text{ \AA}$) they are found in the Lyman- α forest. The absorption lines to the right from the Lyman- α emission are due to metallic ions (C IV, Fe II, Si IV *etc*) at various redshifts, including that of the DLA.

constants [42]. However, since the BBN theory encompasses almost all of the fundamental constants, it becomes difficult to extract constraints on individual constants [10].

$\Delta\mu/\mu$ from molecular hydrogen

As has been first pointed out by Thompson [5] the value of μ defines the relative pattern of the rovibronic transitions in molecular hydrogen (H_2). The energies of the Lyman and Werner band H_2 transitions ($\lambda_{\text{lab}} \sim 900\text{--}1100 \text{ \AA}$) depend on μ as:

$$E_i = c_{\text{elec}} + c_{\text{vibr}} \times \mu^{-1/2} + c_{\text{rot}} \times \mu^{-1}, \quad (1.4)$$

where c_{elec} , c_{vibr} , and c_{rot} are, respectively, the electronic, vibrational, and rotational energies of the i th transition. The observed wavelength of the i th transition is then defined as:

$$\lambda_i = \lambda_{\text{lab}}(1+z)\left(1 + K_i \frac{\Delta\mu}{\mu}\right), \quad (1.5)$$

where λ_{lab} is a corresponding rest wavelength, z is the redshift of the absorber, and K_i is the sensitivity coefficient, different for each transition. At redshifts $z \gtrsim 2$, the rest UV wavelengths of H_2 are shifted to the visible and near UV range ($\gtrsim 3000 \text{ \AA}$) which is accessible from ground-based observatories.

The sensitivity coefficients for the H_2 transitions from the ground vibrational state were derived by making use of *ab initio* calculations of the hydrogen molecule [43] and, independently, based on a Dunham representation of ground state and excited state level energies [44]. Recently, calculations of the sensitivity coefficients of the H_2 transitions from the excited vibrational states were performed, driven by the need to probe hotter environments [45]. The coefficients of the Lyman and Werner bands range from -0.03 to $+0.05$ and are known with an uncertainty of 1% or better. The corresponding laboratory wavelengths are known with a relative precision of $< 8 \times 10^{-7}$ [44, 45] and in the past and current studies of varying μ they can be considered exact.

Even though H_2 is the most abundant molecule in the universe, its detections are rather scarce outside the Local Group: the current quasar census from the Sloan Digital Sky Survey (SDSS) [46] includes more than 150 000 quasars with only some twenty of those sightlines containing H_2 absorption at column densities $\log N[\text{H}_2/\text{cm}^{-2}] > 19$ [47]. As a rule, molecular hydrogen absorption is associated with damped Lyman- α systems (DLAs) which are huge reservoirs of neutral hydrogen gas with $\log N[\text{H I}/\text{cm}^{-2}] \geq 20.3$. In a recent study of 86 medium-to-high resolution quasar spectra that contain DLAs, only 1% detection rate of H_2 was reported for $\log N[\text{H}_2/\text{cm}^{-2}] > 17.5$ [48]. Moreover, not every H_2 detection proves to be useful in the analysis of μ variation – some can

be discarded because observational requirements are currently too challenging or particular absorbing systems have unsuitable intrinsic properties. An ideal system should have:

- a bright background source so that a high-resolution spectrum with a signal-to-noise ratio in the continuum of about 50 per 2.5 km/s pixel could be obtained within, e.g. 15–20 hours at an 8-10 m class optical telescope,
- a column density of H₂ in the range between $\log N[\text{H}_2/\text{cm}^{-2}] \sim 14$ and 18; a column density outside this range would either yield a small number of detectable H₂ transitions or a high number of saturated transitions; neither of these situations is desirable since the precision with which $\Delta\mu/\mu$ can be measured depends on the number of strong but unsaturated transitions,
- an absorption redshift of at least $z = 2$ or larger to assure that a sufficient number of lines (typically > 40) will shift beyond the atmospheric cut-off at 3000 Å,
- absorption profiles of H₂ with simple substructure: see Fig. 1.2 for examples of different absorption profiles; while fitting multiple Voigt components to an H₂ absorption profile is feasible and can be justified (see Chapters 2 to 4), a simpler absorption substructure is preferred.

A system that obeys these requirements would yield a $\Delta\mu/\mu$ constraint with a precision of several parts per million. Table 1.1 contains a list of the eight best H₂ systems that have been already analyzed for μ variation, and 19 additional systems whose properties are less suitable for a varying- μ analysis. Relevant details, such as absorption and emission redshifts, position on the sky, the known column densities for H₂, deuterated molecular hydrogen, HD, carbon monoxide, CO, and neutral atomic hydrogen, HI, and the magnitude are provided as well. With similar K_i sensitivities as those of H₂, the rovibronic transitions of HD and CO provide a way to independently crosscheck $\Delta\mu/\mu$ constraints from H₂ [49, 50]. However, the column densities of HD and CO are usually $\sim 10^5$ times smaller than $N(\text{H}_2)$, leading to a much smaller number of detections and fewer transitions in case of detection. Combining the results of the 8 high-quality systems of H₂ that have been analyzed so far (see Fig. 4.4 in Chapter 4) shows that for a redshift range $z \sim 2.0 - 4.3$ the relative change in proton–electron mass ratio is $\Delta\mu/\mu = (3.3 \pm 1.9) \times 10^{-6}$. At a significance of 1.7- σ , this result provides only weak evidence for varying μ .

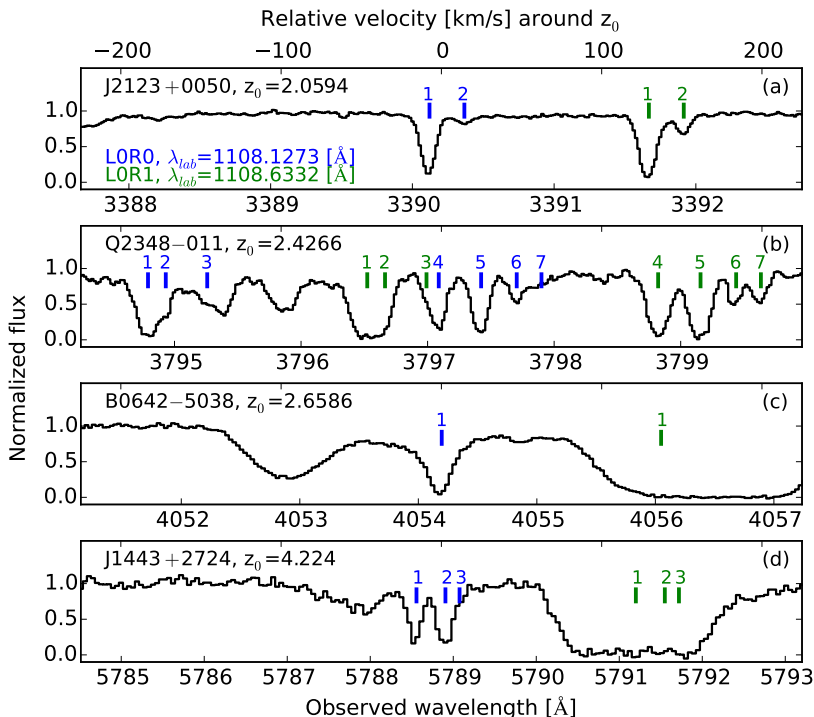


Figure 1.2: Two H₂ transitions seen at different redshifts toward four quasars (observed with the VLT/UVES): (a) in the J2123+0050 spectrum, each transition is imprinted in two velocity features which means that the light from the quasar crossed two clouds of H₂ at slightly different redshifts (within the same galaxy); the region is rather clean from the lines of the Lyman- α forest, (b) in the Q2348-011 spectrum, a very complex H₂ absorption system is observed, containing seven visually distinguishable velocity features; this particular region is overlapped by a number of H I lines at the observed wavelengths of ~ 3795.5 – 3796.0 Å, (c) toward the quasar B0642-5038, H₂ absorption is detected in a single velocity feature; the LOR1 transition is completely overlapped by a strong H I feature of the Lyman- α forest, (d) in the J1443+2724 spectrum, the H₂ transition is observed in three velocity features, two of which are blended; again, the LOR1 transition is not detected because of the Lyman- α forest. The widths of the H₂ features are usually much smaller (~ 2 km s⁻¹) than those of H I (> 10 km s⁻¹). Depending on the morphology of the absorbing cloud(s), a single velocity feature can consist of multiple closely spaced components.

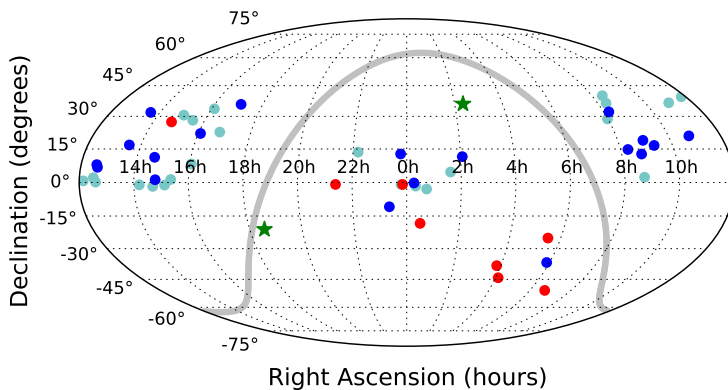


Figure 1.3: Sky map in equatorial coordinates (J2000) showing currently known quasar sightlines containing molecular absorbers at intermediate-to-high redshifts. The red points correspond to the 8 H_2 absorbers that have been analyzed for a variation of μ , while the blue points mark confirmed H_2 targets that might be used in future analyses (see Table 1.1). The light blue points correspond to a sample of candidate H_2 absorption systems found through the Sloan Digital Sky Survey [47]. The green stars indicate the sightlines toward PKS1830–211 and B0218+357 where μ variation was measured from CH_3OH and NH_3 , or only from NH_3 , respectively. The grey line indicates the galactic plane.

Table 1.1: List of known moderate-to-high redshift H_2 absorption systems with some relevant parameters. Bessel R magnitude taken from the SuperCOSMOS Sky Survey [51]. The eight high-quality systems analyzed so far are offset. The column densities $N(H_2)$, $N(HD)$, $N(CO)$ and $N(HI)$ are given on a \log_{10} scale in cm^{-2} .

Quasar	z_{abs}	z_{em}	RA (J2000)	Decl. (J2000)	$N(H_2)$	$N(HD)$	$N(CO)$	$N(HI)$	R_{mag}	Ref.
HE0027-1836	2.42	2.55	00:30:23.62	-18:19:56.0	17.3			21.7	17.37	[54, 37]
Q0347-383	3.02	3.21	03:49:43.64	-38:10:30.6	14.5			20.6	17.48	[55, 56]
Q0405-443	2.59	3.00	04:07:18.08	-44:10:13.9	18.2			20.9	17.34	[55, 56]
Q0528-250	2.81	2.81	05:30:07.95	-25:03:29.7	18.2	13.3		21.1	17.37	[56, 57]
Q0642-5038	2.66	3.09	06:43:26.99	-50:41:12.7	18.4			21.0	18.06	[58, 59, 60]
J1443+2724	4.22	4.42	14:43:31.18	+27:24:36.4	18.3			21.0	18.81	[61], Ch. 4
J2123-0050	2.06	2.26	21:23:29.46	-00:50:52.9	17.6	13.8		19.2	15.83	[62, 63]
Q2348-011	2.42	3.02	23:50:57.87	-00:52:09.9	18.4			20.5	18.31	[64, 65, 66]
Q0013-004	1.97	2.09	00:16:02.40	-00:12:25.0	18.9			20.8	17.89	[67]
Q0201+113	3.39	3.61	02:03:46.66	+11:34:45.4	≤ 16.4			21.3	19.41	[68]
Q0551-366	1.96	2.32	05:52:46.18	-36:37:27.5	17.4			20.5	17.79	[69]
J0812+3208	2.63	2.70	08:12:40.68	+32:08:08.6	19.9	15.4		21.4	17.88	[70, 71]
J0816+1446^a	3.29	3.85	08:16:34.39	+14:46:12.5	18.66			22.0	19.20	[72]
Q0841+129	2.37	2.48	08:44:24.24	+12:45:46.5	14.5			20.6	17.64	[73]
J0857+1855	1.72	1.89	08:57:26.79	+18:55:24.4			13.5		17.32	[53]
J0918+1636	2.58	3.07	09:18:26.1	+16:36:09	≤ 19.0			21.0	19.49	[74]
J1047+2057^b	1.77	2.01	10:47:05.8	+20:57:34			14.7		19.96	[53]
Q1232+082	2.34	2.57	12:34:37.58	+07:58:43.6	19.7			20.9	18.40	[75, 76]
J1237+064^c	2.69	2.78	12:37:14.60	+06:47:59.5	19.2		14.2	20.0	18.21	[77]
Q1331+170	1.78	1.78	13:33:35.81	+16:49:03.7	19.7	14.8		21.2	16.26	[71, 78]
J1337+3152	3.17	3.17	13:37:24.69	+31:52:54.6	14.1			21.4	18.08	[40]

Continued on next page.

Table 1.1 – *continued from previous page.*

Quasar	z_{abs}	z_{em}	RA (J2000)	Decl. (J2000)	$N(\text{H}_2)$	$N(\text{HD})$	$N(\text{CO})$	$N(\text{HI})$	R_{mag}	Ref.
J1439+1117	2.42	2.58	14:39:12.04	+11:17:40.5	19.4	14.9	13.9	20.1	18.07	[79, 80]
Q1444+014	2.08	2.21	14:46:53.04	+01:13:56.0	18.3			20.1	18.10	[81]
J1604+2203^d	1.64	1.98	16:04:57.49	+22:03:00.7			14.6		19.09	[82]
J1705+3543^e	2.04	2.02 ^f	17:05:42.91	+35:43:40.3			14.1		19.42	[53]
Q2318–111	1.99	2.56	23:21:28.69	–10:51:22.5	15.5			20.7	17.67	[54]
Q2343+125	2.43	2.52	23:46:25.42	+12:47:43.9	13.7			20.4	20.18	[83, 84]

^a SDSS J081634.40+144612.9, ^b SDSS J104705.75+205734.5, ^c SDSS J123714.60+064759.5,

^d SDSS J160457.50+220300.5, ^e SDSS J170542+354340, ^f z_{em} reported by [52] is smaller than z_{abs} from [53].

To tackle the question of a possible spatial variation of μ , one needs an evenly spread distribution of as many $\Delta\mu/\mu$ measurements as possible across the sky. For comparison, limits on the spatial variation of α were determined from more than 300 measurements of ionized metallic gas systems [36]. Compared to that, the current sample of $\Delta\mu/\mu$ measurements is too small to fit a spatial model. Fig. 1.3 shows how the quasar sightlines with H₂/HD/CO detections are distributed. A sample of candidate H₂ systems detected in a recent study of the SDSS data [47] is displayed in addition to the confirmed sample from Table 1.1. Besides those detections, some ten lower redshift ($0.05 \lesssim z \lesssim 0.7$) molecular hydrogen absorbers have been discovered in the archival Hubble Space Telescope/Cosmic Origins Spectrograph spectra (at $\log N[\text{H}_2/\text{cm}^{-2}] > 14.4$, [85]). This sample may offer an interesting opportunity to obtain independent $\Delta\mu/\mu$ constraints at similar redshifts as those accessible through meteoritic and geophysical methods. The H₂ incidence rate at low redshifts was found to be at least double the corresponding rate at high redshifts [58, 48]. This finding is in agreement with a general trend of higher fraction of cold neutral medium found in galaxies at lower redshifts [86].

Besides quasars, the brief and very luminous gamma-ray burst (GRB) afterglows can also be used in searches for extragalactic H₂ absorption. GRBs are thought to mark the violent death of (very) massive stars leaving black holes or strongly magnetized neutron stars. Contrary to QSO sight lines, the GRB DLA usually refers to the (star-forming) host galaxy. Only four detections of H₂ absorption in GRB-DLAs are known so far, including GRB 080607 at $z = 3.04$ [87], GRB 120815A at $z = 2.36$ [88], GRB 120327A at $z = 2.81$ [89], and GRB 121024A at $z = 2.30$ [90]. While the quality of the current GRB spectra containing H₂ is not sufficient to obtain competitive $\Delta\mu/\mu$ constraints, GRBs can in principle give access to more H₂ (and CO) detections at redshifts as high as $z \gtrsim 4$. QSOs become very rare at redshifts larger than 6.

Discovery of H₂ molecules in the atmosphere of a white dwarf [91] allowed for probing μ dependence on the strength of gravitational fields [45]. H₂ molecules on a white dwarf are exposed to a $\sim 10^4$ times stronger gravitational field when compared to that at the Earth's surface. The study resulted in $|\Delta\mu/\mu|$ limits of the order of $< 5 \times 10^{-5}$ and it constitutes Chapter 5 of the present thesis. A similar analysis on varying α was performed using a white dwarf spectrum of iron and nickel ions [92]. The resulting $\Delta\alpha/\alpha$ constraints do not indicate a detection of variation, however, better precision of the laboratory wavelengths of the iron and nickel transitions is needed to draw definite conclusions.

$\Delta\mu/\mu$ from ammonia and methanol

While the rovibronic H_2 transitions have been implemented in putting limits on varying μ at moderate-to-high redshifts, the most stringent $\Delta\mu/\mu$ constraints are derived from methanol (CH_3OH) and ammonia (NH_3) at redshifts $z \sim 0.6 - 0.9$.

In NH_3 , which is a symmetric top molecule with a finite energy barrier of its double-well potential, the nitrogen atom can undergo a quantum mechanical tunneling through the plane of H atoms that results in a rovibrational microwave spectrum. These inversion transition energies scale with μ as $E_{\text{inv}} \sim \mu^{-4.46}$ [93, 94], which makes NH_3 a two orders of magnitude more sensitive probe to varying μ than H_2 . Given that a single sensitivity is shared by a number of NH_3 transitions, a comparison to transitions with a different sensitivity has to be made to solve for a degeneracy with redshift. Usually, the $K_i = -1$ rotational transitions of other molecular species are picked as the reference transitions, and it is assumed that the multiple species occupy exactly the same physical location. Currently, two instances of NH_3 absorption are known outside the local universe: at $z = 0.69$ towards B0218+357 and at $z = 0.89$ towards PKS1830–211. Measurements of NH_3 resulted in $3\text{-}\sigma$ limits of $|\Delta\mu/\mu| < 1.8 \times 10^{-6}$ in the former sightline [95] and $< 1.4 \times 10^{-6}$ in the latter [96].

A recent work by Spirko [97] took into account that the rotational energy levels of NH_3 exhibit a non-negligible centrifugal distortion dependence, which was disregarded in previous calculations. With this correction, a single sensitivity coefficient of $K_i = -4.46$ is replaced with a range of K_i coefficients from -4.9 to -4.2 . From these calculations and the spectroscopic measurements of NH_3 at redshift $z = 0.89$ [98], we derive a new independent limit of $\Delta\mu/\mu = (-1.1 \pm 7.0) \times 10^{-6}$, which is free from assumptions pertaining to multi-species measurements. See Fig. 1.4 for a graphical representation of the result.

Methanol is an even more sensitive probe of varying μ , with K_i sensitivities ranging from -33 to $+19$ [99, 100]. Besides purely rotational transitions, the microwave spectrum of CH_3OH includes rotation-tunneling transitions arising via the hindered rotation of the OH group that show enhanced sensitivity to μ . In fact, the most stringent current $|\Delta\mu/\mu|$ constraints at the level of $< 1.1 \times 10^{-7}$ ($1\text{-}\sigma$) are derived from a combination of these CH_3OH absorption lines at redshift $z = 0.89$ towards PKS1830–211 [20, 21, 101]; also see Chapter 6 and 7 of the present thesis. As opposed to the NH_3 method, where a comparison with other molecular species is often used, methanol offers an advantage of a test based on a single species.

Compared to H_2 , the CH_3OH and NH_3 methods are favored because of their enhanced sensitivity. However, only two intermediate redshift $\text{NH}_3/\text{CH}_3\text{OH}$

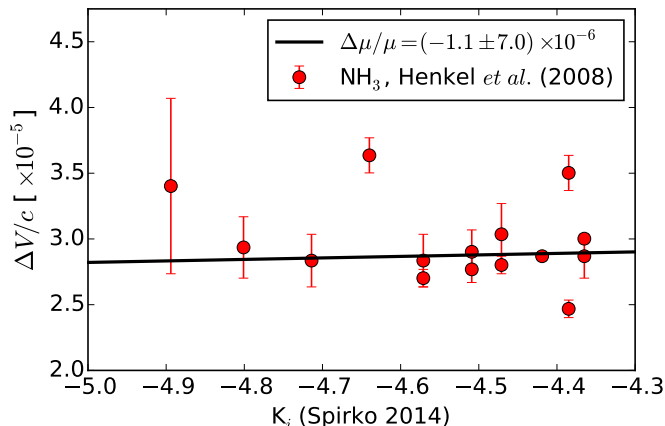


Figure 1.4: A new constraint of $\Delta\mu/\mu$ is derived based on the updated values of K_i sensitivity coefficients of the inversion transitions in NH_3 [97]. The line positions, ΔV , taken from Table 6 of [98] are plotted on the y -axis in units of c . A relation of the form $\Delta V/c = -K_i \times \Delta\mu/\mu$ was used to extract a 1- σ constraint of $\Delta\mu/\mu = (-1.1 \pm 7.0) \times 10^{-6}$.

absorbers are known currently. More probes with highly sensitive radio transitions have been proposed, including methyl mercaptan CH_3SH [102], various internal rotor molecules [103], ethylene glycol $\text{C}_2\text{H}_6\text{O}_2$ [104], acetone $(\text{CH}_3)_2\text{CO}$ [105], H_2^+ , D_2^+ , and He_2^+ ions [106], certain linear poly-atomic molecules [107], methylidyne CH [108, 109], methylamine CH_3NH_2 [110], hydrogen peroxide H_2O_2 [111], and hydronium H_3O^+ [112]. Some of these species (*e.g.*, methylidyne, acetone) have been detected in the Galactic interstellar clouds but detections at moderate-to-high redshifts are lacking.² In fact, there are five known sightlines at redshifts $z = 0.25\text{--}0.89$ that have molecular absorption lines in the radio range. Apart from PKS1830–211 and B0218+357, there is PKS1413+357 with absorption at $z = 0.247$ [113], B1504+377 with absorption at $z = 0.672$ [114], and PMN J0134–0931 with absorption at $z = 0.765$ [115]. Three out of the five known systems are gravitationally lensed objects: PKS1830–211, B0218+357, and PMN J0134–0931. The high detection-rate of gravitationally lensed objects is a selection bias because lensing amplifies the flux of the background quasar. It is expected that with the recently inaugurated and planned radioastronomical facilities, such as the Ata-

²See <http://www.astro.uni-koeln.de/cdms/molecules> for a list of molecules detected in the Galactic and extragalactic interstellar clouds.

cama Large Millimeter/submillimeter Array or the Square Kilometre Array, more detections of extragalactic molecular absorption will be found in the foreseeable future. The enhanced sensitivity of the new cm- and mm-wave telescopes will allow finding weaker radio sources, and the broad bandwidths of the new spectrometers will permit extensive molecular line surveys at high redshift.

1.5 Outline of thesis

In this thesis, the possibility of a varying proton–electron mass ratio is studied via spectroscopic measurements of sensitive transitions in methanol and molecular hydrogen molecules found in distant galaxies and in white dwarf atmospheres. Besides the introduction, this thesis consists of 6 chapters, each of which is published or submitted for publication as a self-contained article. The spectroscopic data used in the presented studies were collected with the following astronomical facilities: Chapters 2 to 4 are based on high-redshift quasar observations with the Very Large Telescope/Ultraviolet and Visual Echelle Spectrograph; Chapter 5 is based on the Hubble Space Telescope/Cosmic Origins Spectrograph archival data of two white dwarf stars; for Chapter 6, a radio spectrum of redshifted methanol absorption was obtained with the Effelsberg telescope; for Chapter 7, additional spectra of methanol were obtained with the Institut de Radio Astronomie Millimétrique 30-m telescope and the Atacama Large Millimeter/submillimeter Array.

In Chapter 2, a $\Delta\mu/\mu$ constraint is obtained from the most complex currently known H_2 absorption system which is found at redshift $z = 2.426$ toward Q2348–011. Seven distinct absorption features per H_2 transition, and the overlapping HI transitions from the Lyman- α forest are modeled simultaneously by employing a so-called comprehensive fitting method, yielding a constraint of $\Delta\mu/\mu = (-0.68 \pm 2.78) \times 10^{-5}$.

In Chapter 3, an analysis of an H_2 absorption system at redshift $z = 2.659$ toward the background quasar B0642–5038 is presented, delivering a constraint of $\Delta\mu/\mu = (12.7 \pm 4.5_{\text{stat}} \pm 4.2_{\text{sys}}) \times 10^{-6}$. A detailed account of various systematics is provided, including a new important systematic error related to wavelength calibration of the ESO Ultraviolet and Visual Echelle Spectrograph mounted on the Very Large Telescope.

Chapter 4 focuses on an H_2 absorbing system at the highest redshift so far, namely, $z = 4.224$ corresponding to a lookback time of 12.4 billion years. A constraint of $\Delta\mu/\mu = (-9.5 \pm 5.4_{\text{stat}} \pm 5.3_{\text{sys}}) \times 10^{-6}$ is obtained.

In Chapter 5, μ dependence on the gravitational potential is tested by analyzing multiple H_2 absorption transitions found in the atmosphere of two white dwarfs: GD133 and G29–38. Compared to cold clouds observed in

the sightlines toward quasars, a different range of H_2 transitions is detected at high temperatures of $> 11\,000$ K. Based on new calculations of sensitivity coefficients, the analysis of the white dwarf GD133 yields a $\Delta\mu/\mu$ constraint of $(-2.7 \pm 4.7_{\text{stat}} \pm 0.2_{\text{sys}}) \times 10^{-5}$ for a local environment of a gravitational potential $\phi \sim 10^4 \phi_{\text{Earth}}$, while that of G29–38 yields $\Delta\mu/\mu = (-5.8 \pm 3.8_{\text{stat}} \pm 0.3_{\text{sys}}) \times 10^{-5}$ for a potential of $2 \times 10^4 \phi_{\text{Earth}}$.

Chapter 6 presents a study of methanol absorption at redshift $z = 0.89$, observed in a gravitational lens toward PKS1830–211. While only four transitions of methanol were measured, their enhanced sensitivity to μ variation results in a high-precision constraint at the level of $|\Delta\mu/\mu| \leq 1.0 \times 10^{-7}$.

Chapter 7 is a subsequent study of methanol toward PKS1830–211 where as many as ten different methanol transitions were observed at three different radio telescopes. With a larger sample of transitions, systematic effects such as chemical segregation, excitation temperature, and time variability of the background source are quantified. A constraint of $\Delta\mu/\mu = (-1.0 \pm 0.8_{\text{stat}} \pm 1.0_{\text{sys}}) \times 10^{-7}$ is obtained.

Constraint on a variation of the proton-to-electron mass ratio from H₂ absorption toward quasar Q2348–011

*Bagdonaite, J., Murphy, M. T., Kaper, L. & Ubachs, W.
Mon. Not. Roy. Astron. Soc. 421, 419–425 (2012).*

Abstract

Molecular hydrogen (H₂) absorption features observed in the line-of-sight to Q2348–011 at redshift $z_{\text{abs}} \simeq 2.426$ are analyzed for the purpose of detecting a possible variation of the proton-to-electron mass ratio $\mu \equiv m_{\text{p}}/m_{\text{e}}$. By its structure, Q2348–011 is the most complex analyzed H₂ absorption system at high redshift so far, featuring at least seven distinctly visible molecular velocity components. The multiple velocity components associated with each transition of H₂ were modeled simultaneously by means of a comprehensive fitting method. The fiducial model resulted in $\Delta\mu/\mu = (-0.68 \pm 2.78) \times 10^{-5}$, showing no sign that μ in this particular absorber is different from its current laboratory value. Although not as tight a constraint as other absorbers have recently provided, this result is consistent with the results from all previously analyzed H₂-bearing sightlines. Combining all such measurements yields a constraint of $|\Delta\mu/\mu| \leq 10^{-5}$ for the redshift range $z = 2-3$.

2.1 Introduction

The spectrum of molecular hydrogen is known to be a testing ground to search for temporal variation of the proton-electron mass ratio, $\mu \equiv m_p/m_e$, on cosmological timescales [5]. The spectral lines of the Lyman and Werner absorption bands of H₂ shift into an atmospheric transmission window ($\lambda > 3050 \text{ \AA}$) for absorption systems at redshift $z \gtrsim 2$, and thus become observable with ground-based optical telescopes. Wavelengths of H₂ spectral lines as observed in high redshift absorption systems are compared to the wavelengths measured in the laboratory for which now very accurate calibrations exist [116, 117, 118] as well as for the HD isotopologue [49, 119], which is currently also detected at high redshift. Values for the sensitivity coefficients, K_i , expressing the shift of each spectral line as a result of a drifting μ , have been established to sufficient accuracy for H₂ [43, 44]. Hence a condition is accomplished that searches for cosmological μ variation via H₂ spectra solely depend on the accuracy of the astrophysical data.

From the large number of damped Lyman- α systems (DLAs) identified only some 20 are known to harbor detectable H₂ spectral features [81, 120, 44]. As was discussed recently [121] only a handful of those high-redshift absorption systems can deliver an H₂ spectrum of sufficient quality, *i.e.* a reasonable signal-to-noise (S/N) ratio on the continuum level to be obtained in reasonable data collection times at large-dish telescopes, and a large number of H₂ transitions ($\gtrsim 50$). The high quality spectra of Q0347–383 and Q0405–443 systems obtained with the European Southern Observatory (ESO) Very Large Telescope (VLT) equipped with the high-resolution Ultraviolet and Visible Echelle Spectrograph (UVES) initially yielded an indication for a possible drift in μ , which is expressed via $\Delta\mu/\mu \equiv (\mu_z - \mu_{\text{lab}})/\mu_{\text{lab}}$ [55]. A more sophisticated reanalysis of the same spectra by the so-called comprehensive fitting method, also invoking an improved thorium-argon (Th-Ar) calibration, reduced the initial finding of a $4\text{-}\sigma$ effect of a positive $\Delta\mu/\mu$ to a $1.5\text{--}2.0\text{-}\sigma$ effect [56]. The same spectra were also reanalyzed by [122] and by [123], while [124] reobserved Q0347–383 with VLT/UVES to find a $1.5\text{-}\sigma$ effect. The highest quality system observed so far is J2123–0050. Observations with both the Keck Telescope [62] and VLT [63] were incorporated in a μ -variation analysis. The two studies yielded constraints on $\Delta\mu/\mu$ which are in very good agreement with each other. The averaged constraint for J2123–0050 is $\Delta\mu/\mu = (7.6 \pm 3.5) \times 10^{-6}$. The system Q0528–250 has been at the heart of μ -variation analyses since the first attempts by [125] to derive a constraint on $\Delta\mu/\mu$ from a low-resolution spectrum. [56] derived a tight constraint from a comprehensive fitting analysis of a VLT spectrum of Q0528–250; a recent reobservation of this high-quality system, again at the VLT, confirmed the previous conclusion of a tight constraint on $\Delta\mu/\mu$ [57]. On the basis of the combined results derived from high-redshift

hydrogen absorbers it can be concluded that $|\Delta\mu/\mu| < 1 \times 10^{-5}$ for redshifts $z = 2-3$.

The present study presents a detailed analysis of the search for μ -variation of an absorber system toward the quasar Q2348–011. The physical conditions of this system had been investigated before based on data from the VLT [83, 64, 65]. Q2348–011 was shown to be an exceptional sightline, with a number of DLAs and sub-DLAs present, and a very complex velocity structure in the major H₂ absorbing system at $z \simeq 2.426$. At least seven distinctly visible absorption features are associated with each H₂ transition in this system, while in other quasar sightlines H₂ absorption (if detected) exhibits much simpler profiles consisting typically of one or two features. For the present study, dedicated observations were performed at VLT focusing on improvement of S/N and on wavelength calibration of the spectrum. A preliminary μ -variation analysis of this absorber was presented in [121]. The current work improves upon the analysis but the constraint on $\Delta\mu/\mu$ is of similar precision as presented previously. It is demonstrated that a complex velocity structure consisting of at least seven distinct H₂ velocity features can be disentangled by the method of comprehensive fitting [56, 62, 57].

2.2 Data

The new spectrum of the quasar Q2348–011 was obtained with the UVES spectrograph on the ESO VLT on four consecutive nights (2008 August 18–21). Q2348–011 is not a particularly bright object ($R = 18.31$) so a long exposure time was required. 15 exposures were taken, making up a combined total of 19.25 hours of observation. After each science exposure, without any intervening grating resets, a Th-Ar exposure was recorded for calibration purposes. Seeing was in the range between $0''.53$ and $2''.32$. Besides the exposures noted above, the final spectrum incorporates data obtained from the ESO data archive (observations from 2003 October 29 to 30). They contribute additional 4.50 hours but do not have the individually taken Th-Ar calibration frames.

The raw 2D exposures were bias-corrected, flat-fielded, and the quasar flux extracted using the Common Pipeline Language version of the UVES pipeline.¹ The wavelength calibration was established by extracting each Th-Ar frame using the object profile weights from its corresponding quasar exposure. Further details of the wavelength calibration procedure are described in [126]. The root-mean-square wavelength calibration residuals were typically $\approx 70 \text{ m s}^{-1}$ in the Lyman- α forest portion of the spectrum, where the H₂ lines fall. The wavelength scale of each quasar exposure was corrected from air to vacuum, and to the heliocentric reference frame, and the flux was redispersed onto a com-

¹http://www.eso.org/observing/dfo/quality/UVES/pipeline/pipe_reduc.html.

mon loglinear scale before being coadded, using UVES_POPLER,² a code specifically written to redisperse and combine reduced exposures from UVES.

The spectrum of Q2348–011 covers wavelengths 3572–9467 Å, with gaps at 4520–4621 and 7505–7665 Å. The final spectrum has a resolving power of $R \sim 57,000$ and 63,000, and the log-linear dispersion is set to 2.5 km s⁻¹ and 1.5 km s⁻¹ in the blue (< 4000 Å) and in the red (> 4000 Å) parts, respectively. CCD pixels were binned by a factor of 2 in both spatial and spectral directions for all exposures in the blue, and no binning was applied for the red exposures. In the blue part where H₂ features are detected the average S/N ratio is about 25.

2.3 The comprehensive fitting method

The main aim of the present analysis is to determine the spectral positions of the H₂ absorption features present in a quasar spectrum as accurately as possible since their overall pattern defines the value of $\Delta\mu/\mu$: each absorption line of the H₂ Lyman and Werner bands shows a unique shift for a given change of μ that depends on the vibrational and rotational quantum numbers of the upper and lower energy states. The shifted wavelength λ_i is related to the rest wavelength λ_0 by

$$\lambda_i = \lambda_0(1+z)(1 + K_i \frac{\Delta\mu}{\mu}), \quad (2.1)$$

where z is the redshift of the absorber, and K_i is the sensitivity coefficient, different for each line. To achieve this goal a so-called comprehensive fitting method can be applied. This method requires fitting the absorption profiles of multiple H₂ transitions simultaneously. It relies on a physical assumption that all transitions arise from the same cloud (collection of clouds) of molecular hydrogen and, therefore, they share the parameters describing the properties of the clouds (see e.g. [62]).

Each H₂ transition can be detected in one or several absorption features depending on how many molecular hydrogen clouds are penetrated by the light of the quasar. We refer to each fitted component as a velocity component, as they are situated closely in velocity space. It is assumed that a given velocity component has the same redshift, z_{abs} , and Doppler width, b , in all transitions independent of the rotational level, J . Each J level has a different population, represented by the column density N , but for a given velocity component it is the same for all transitions from the same J level. To analyze the spectrum we use the Voigt profile fitting program VPFIT,³ that permits to tie the free

²Developed and maintained by M. Murphy; see http://astronomy.swin.edu.au/~mmurphy/UVES_popler.

³<http://www.ast.cam.ac.uk/~rfc/vpfit.html>.

parameters between various transitions. The optimal model is found by fitting all suitable transitions at the same time.

The differential shifts of the molecular hydrogen lines are only known to be possible through the $\Delta\mu/\mu$ parameter (see Eq. 2.1). It is added as a free parameter after all other parameters have been optimized. The comprehensive fitting approach allows minimization of the number of free parameters in the fit and, thus, the reliability of the absorption model which eventually translates to the robustness of $\Delta\mu/\mu$ resulting from the model.

2.4 Analysis

The absorption system

The wavelengths covered by the VLT-UVES spectrum provide 58 H_2 transitions for rotational levels $J = 0\text{--}5$. All the observed lines arise from the Lyman band. In Fig. 2.1 a couple of H_2 transitions are displayed. No lines of HD were detected in this system. In the ideal case this spectrum would provide a sample of 58×7 molecular hydrogen absorption lines. However, not all of them are suitable for the analysis. First of all, the broad Lyman- β of an additional DLA at $z \simeq 2.62$ falls in the wavelength range where H_2 lines are detected, namely near 3710 Å. The break at ≤ 3590 Å might be produced by another absorber at $z \simeq 2.93$. These features make some of the H_2 transitions unavailable, and strongly damp some others. Also, the weaker HI absorbers of the Lyman- α forest contaminate many of the regions with H_2 lines. Generally, the sight-line of the Q2348–011 is rich in absorbing systems. The full list of detected metal absorbers is given in Table 2.1. Some of the absorbers have their metal absorption lines overlapped with H_2 lines. The metal absorption profiles are constrained by fitting their counterparts in the red part, e.g. Fe II $\lambda 1096$ Å of the $z \simeq 2.426$ absorber can be constrained by tying it with Fe II $\lambda 1608$ Å.

Since the velocity structure of H_2 consists of at least seven velocity features spread over ~ 250 km s $^{-1}$, nearby lying transitions exhibit mutual overlap of velocity components. The self-blending of the H_2 transitions was often the decisive factor when setting the boundaries of usable fitting regions (i.e. regions over which χ^2 was calculated): only rarely did they include just one transition (see Fig. 2.2 as an example).

Twenty-three regions with 32 different molecular hydrogen transitions and eight regions with relevant metal absorption profiles were selected for further analysis. Although the total number of H_2 transitions available in this spectrum is reduced due to blends with HI lines, the scarcity of information is at least partially compensated for by the presence of multiple velocity components associated with each transition. Altogether, each transition contributes a higher information content when it is imprinted in several velocity compo-

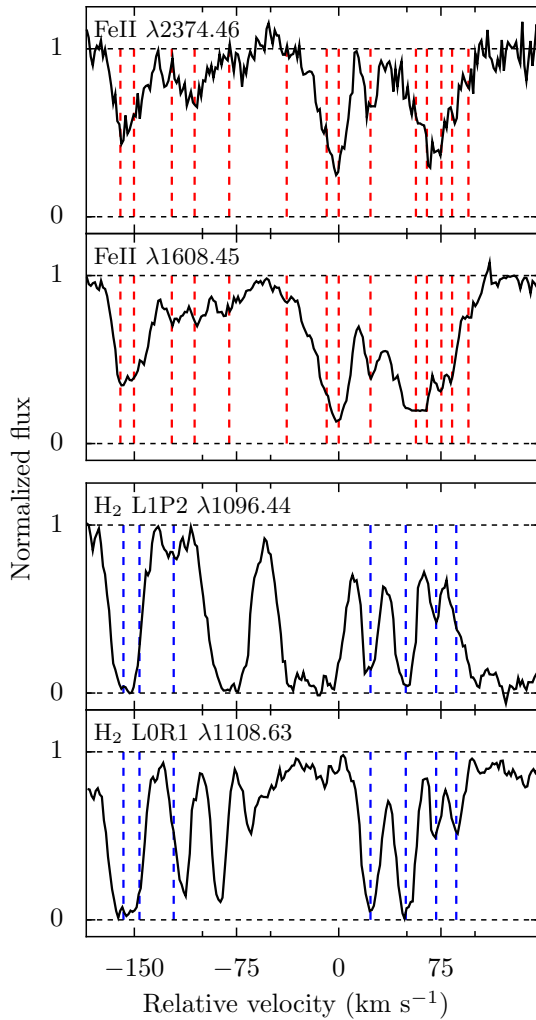


Figure 2.1: Two H₂ and two Fe II transitions are displayed on a common velocity scale, centered at $z_0 = 2.4263230$. In the H₂ velocity profile 7 distinct features are visible, while the Fe II profiles consist of at least 14. Note that, the third velocity component from the left in the H₂ L0R1 profile, and the right-most component in the H₂ L1P2 profile are blended with other intervening transitions in Lyman- α forest. Due to such blends, the signal of at least 7 absorption components is evident only when multiple H₂ transitions are explored simultaneously.

Table 2.1: A list of all the confirmed detections of metal absorbers in the spectrum of Q2348–011. Species whose transitions overlap some of the fitted H₂ regions are in bold.

Redshift	Species
0.774	Mg II
0.863	Mg II, Ca II
1.444	C IV , Mg II
2.426	C IV, Si IV, N V, C I, C I*, P II, Zn II, Al III, Fe II , S II, Si II
2.582	C IV, Si IV, Si II
2.615	C IV, Si IV, Fe II, Ni II, Cr II, Al II, Si II , O I , N I
2.739	C IV, O I
2.929	C IV, Si IV
2.969	C IV, N V

nents. A part of the spectrum with all available and all fitted H₂ transitions indicated is provided in Fig. 2.4.

Exploring the velocity structure of H₂

Seven absorption features can be distinguished by eye in the velocity structure of molecular hydrogen in the Q2348–011 spectrum (see Fig. 2.1, also [65]). However, as it was shown by [127], a single spectral feature might need to be modeled by more than one velocity component so it is plausible that in the case of Q2348–011 more than seven velocity components are actually required to produce a model which is both physically realistic and statistically acceptable. If a single Voigt profile is fitted to a feature which seems single but another weaker blending line is actually present, then the centroid returned from this fit will be shifted toward the blending line. The centroid wavelength of the fitted feature might be expressed as the intensity-weighted mean of the two blended lines. The positions of the lines play a crucial role in μ -variation analysis and this kind of underfitting may affect the results and therefore should be avoided.

The approach to reaching the optimal model of H₂ absorption is to keep adding velocity components until a statistically acceptable fit is achieved (e.g., [62, 57]). The initial absorption model included seven velocity components of H₂. Voigt profile parameters (z , b , N) of corresponding components are tied as described in Section 2.3. Each of the included regions was revisited and refined many times until an adequate fit was reached. By adequate we mean that the normalized residuals in each of the fitted regions are not too large or too small

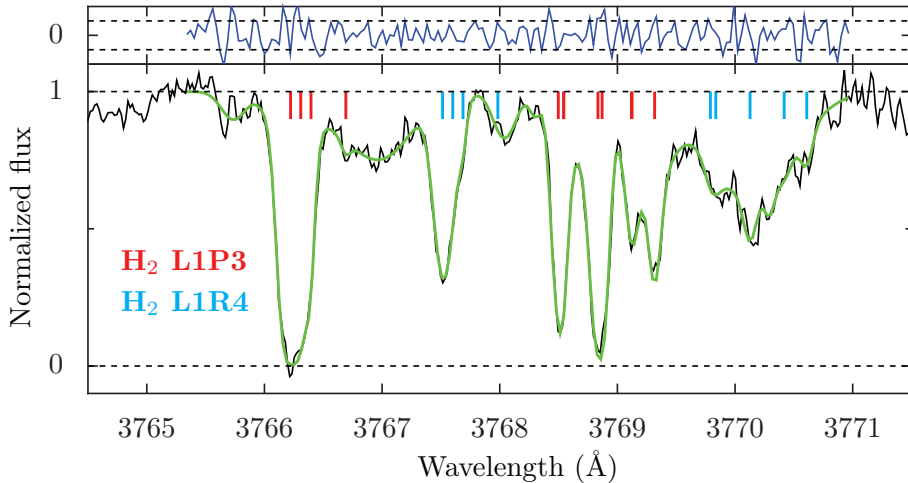


Figure 2.2: H₂ absorption profiles of two transitions: L1P3, and L1R4, as resulted from the fiducial model. Since the absorption arises in multiple widely spread components (indicated by the red tick marks for L1P3, and by the blue tick marks for L1R4), the two profiles overlap. The upper graph shows the normalized residuals of the fit; the dashed lines mark $\pm 1\text{-}\sigma$ limits.

Table 2.2: Resulting $\Delta\mu/\mu$ values and their statistical uncertainties from various consistency tests (referenced by i–iv in the section on exploring the velocity structure of H₂) performed on the 12 velocity component absorption model. The $b \neq F[J]$ and the $b = F[J]$ models are different in that the former has b parameters tied in all J levels of corresponding velocity components whilst in the latter they are only tied within every J level of corresponding velocity components. The last line of the table refers to a test, in which only the best exposures (calibration-wise) were included in the spectrum.

	b	Transitions	n_{trans}	Components	$\Delta\mu/\mu [\times 10^{-5}]$
	$\neq F[J]$	all	32	all	-0.68 ± 2.70
i		all	28	left	3.55 ± 4.34
i		all	22	right	-3.87 ± 3.43
ii		$J = [0, 1]$	11	all	-0.86 ± 3.50
ii		$J = [2 - 5]$	21	all	-0.46 ± 4.06
iii	$= F[J]$	all	32	all	-1.20 ± 3.03
iv	$\neq F[J]$	all	32	all	0.68 ± 3.45

(i.e. they are distributed around $[-1\sigma; +1\sigma]$), and no long range correlations are seen in them. Finally, after the fit was optimized, a value for $\Delta\mu/\mu$ was determined.

In a subsequent step an additional component was added to the left side of the absorption profile (at $\approx -150 \text{ km s}^{-1}$; see Fig. 2.1). The reduced chi-square, χ_ν^2 , of this model is slightly better than that of the initial one with 7 velocity components. The procedure of adding more components was continued further until they started to be rejected from most J levels (>12 component models). We note that several components get rejected from $J = 4$ and 5 transitions in all models. Generally, it is not unusual that weak components are omitted from the lowly populated J levels. The higher J levels are less populated than the lower J levels, so weak components of $J = 4$ and 5 transitions may not be detected. In addition, the Q2348–011 spectrum provides only a few useful regions with $J = 4$ and 5 transitions, which is not enough to amplify the signal of the weak components.

It should be emphasized that $\Delta\mu/\mu$ is always introduced as a single additional parameter after all the other free parameters of the given model have been optimized. This ensures that $\Delta\mu/\mu$ is not biased away from zero in the process of determining which velocity structure is statistically preferred. On the other hand, it could mean that $\Delta\mu/\mu$ might be slightly biased towards zero because the preferred velocity structure might have fitted away some of the relative shifts between transitions which a non-zero $\Delta\mu/\mu$ would have caused. However, given that many H_2 transitions are fitted simultaneously, the bias towards zero will be very weak.

Results of the various fitting runs are displayed in Fig. 2.3, together with the goodness-of-fit measure, χ_ν^2 . As it can be seen in Fig. 2.3, the χ_ν^2 monotonically decreases when more components are added. For models with 10, 11 and 12 components the difference in χ_ν^2 is very small though. This is also true for the derived $\Delta\mu/\mu$ values – they match well within $1\text{-}\sigma$. For further analysis the model with 12 velocity components has been adopted as fiducial.

When all available transitions are included in the 12 component model, the fit delivers $\Delta\mu/\mu = (-0.68 \pm 2.70_{\text{stat}}) \times 10^{-5}$. Next the fiducial model is tested for its robustness. In the process of creating the model, many assumptions and decisions have been made, e.g. how parameters are tied between transitions and which regions are fitted. It can be tested how sensitive the value of $\Delta\mu/\mu$ determined from the model is to certain choices made. A description of several performed tests is given below, while the outcome is summarized in Table 2.2.

- i The extended structure of the H_2 absorption profile can be divided into two parts. As it can be seen from velocity plots, the dividing line naturally falls at around 0 km s^{-1} (Fig. 2.1). When only the left part of the profile, which includes 4 H_2 velocity components, was used in the fitting, it resulted in

$\Delta\mu/\mu = (3.55 \pm 4.34_{\text{stat}}) \times 10^{-5}$. The right part with 8 velocity components delivered $\Delta\mu/\mu = (-3.87 \pm 3.43_{\text{stat}}) \times 10^{-5}$. The larger uncertainty of the left side result can be explained by the fact that several of the fitted transitions were saturated, thus their centroids are determined less accurately. Altogether, the two results are consistent within the combined 1.3- σ .

- ii Instead of allowing all transitions to contribute to a single $\Delta\mu/\mu$ value, within VPFIT it is possible to fit a different value of $\Delta\mu/\mu$ for each J -level or for J -levels grouped in some way. This kind of test allows to quantify the relative contributions different J -levels make to the final result. As not many transitions are available in the Q2348–011 absorber they were not investigated level by level. [44] have suggested that H₂ transitions can be divided into a $J \in [0, 1]$ set (cold states) and a $J \geq 2$ set (warm states) to examine the impact of temperature: due to the para-ortho distribution of H₂ the $J = 1$ state is significantly populated even at low temperatures. A test was performed where only transitions from the cold states or only those from the warm states were used to determine $\Delta\mu/\mu$. The two values of $\Delta\mu/\mu$ match within the uncertainty. It means that the two groups of transitions contribute similarly to the final combined value of $\Delta\mu/\mu$.
- iii All previously described tests were performed on absorption models which are based on the assumption that corresponding velocity components in all transitions have the same b -parameter, independent of rotational quantum state ($b \neq F[J]$). This assumption is relaxed to test what its effect is on $\Delta\mu/\mu$, i.e. in this run different J transitions are allowed to have different b -parameters in corresponding velocity components ($b = F[J]$). No significant discrepancy is found between the values determined from the $b \neq F[J]$ and the $b = F[J]$ models.
- iv The spectrum used in the analysis includes exposures from the older 2003 ESO archival data set that do not have the individually taken Th-Ar calibration frames. They make up 4.50 hrs compared to 19.25 hrs of more accurately calibrated data. In order to make sure that the final result is not affected by the additional (possibly less accurate) data, they were excluded in one of the fit optimizations. The newly determined value is $\Delta\mu/\mu = (0.68 \pm 3.45_{\text{stat}}) \times 10^{-5}$. The result is consistent with the one from the primary fit. The uncertainty is higher since the S/N of the spectrum used in this test is lower.

The performed tests show that the final result on $\Delta\mu/\mu$ determined from the 12 component model is not affected by a subclass of transitions, velocity components or data.

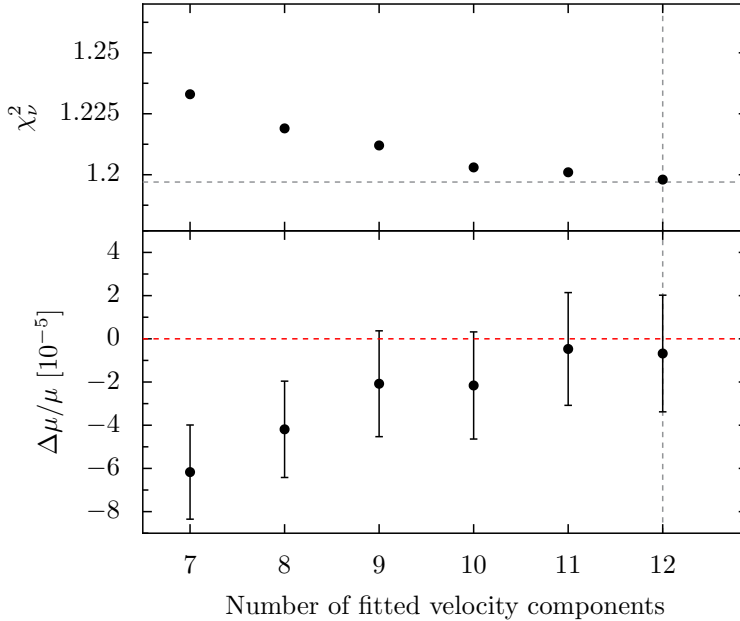


Figure 2.3: Lower graph: $\Delta\mu/\mu$ values as determined from various models. Error bars indicate estimated 1- σ statistical uncertainties. Upper graph: χ^2_ν of the fit decreases as more components are added. A model with 12 components has the lowest χ^2_ν . Adding more components caused inconsistencies in the fit.

Robustness of the model

Systematic errors

The statistical error of the fiducial result is larger than obtained in other recent studies of H₂ studies, e.g. [62, 57]. In those studies, systematic errors were found to be smaller than, but comparable in magnitude to, the statistical errors. Thus, while it is still important to consider systematic errors in the present study, it is not expected them to dominate the error budget.

Every echelle order included in the new Q2348–011 spectrum is calibrated using about 10 Th-Ar lines. The effect of the errors of individual Th-Ar lines is small (about 70 m s⁻¹) and random, so it will average out when many H₂ transitions spread over many orders are used. [126] have shown that possible systematic patterns in the Th-Ar calibration residuals result in a deviation of 30 m s⁻¹ at most. The K_i values used in the present analysis are in the range from -0.015 to +0.018. The effect of the systematic errors can be expressed

via: $\delta(\Delta\mu/\mu) = (\Delta v/c)/\Delta K_i$. A shift of 30 m s^{-1} translates to $\delta(\Delta\mu/\mu) = 0.3 \times 10^{-5}$ which is about 15% of the statistical uncertainty.

In a recent study targeted on the possible miscalibration of the wavelength scale of the UVES spectrograph it is reported that intraorder distortions of about 200 m s^{-1} in size may be present [128]. Their influence can be roughly estimated by dividing the distortion by the square root of the number of the H₂ transitions included in the fit: $200/\sqrt{32} \approx 35 \text{ m s}^{-1}$.

[62] have considered additional sources of possible systematic errors but they are all of the same order as the Th-Ar wavelength calibration uncertainties and are not expected to have substantial impact on the result of the present analysis. It is conservatively assumed that the systematic error is at most 25% of the statistical error of $\Delta\mu/\mu$ derived in the present analysis.

Results

On the basis of the results provided in Table 2.2,

$$\Delta\mu/\mu = (-0.68 \pm 2.70_{\text{stat}} \pm 0.66_{\text{sys}}) \times 10^{-5}$$

is adopted as the fiducial result for the analysis of molecular hydrogen absorption in the Q2348–011 spectrum (or $\Delta\mu/\mu = (-0.68 \pm 2.78) \times 10^{-5}$, adding the uncertainties in quadrature). The result is consistent with no change in μ at the 10^{-5} level.

The analysis of H₂ absorption in the Q2348–011 spectrum yields a result on $\Delta\mu/\mu$ which is less tight compared to the constraints from previous analyzes [121]. One of the major causes that led to the larger uncertainty is the relatively low S/N ratio of the spectrum. The second cause is that the number of lines is relatively small: 32 compared to e.g. 90 in the sightline of J2123–0050, which yields an order of magnitude more precise result on $\Delta\mu/\mu$ [62, 63]. Part of the H₂ spectrum in Q2348–011 is obscured by the neutral hydrogen features of the additional strong DLA at $z \simeq 2.615$ making some of the relevant transitions unavailable. The H₂ transitions falling at the short wavelength range of the spectrum are especially useful in μ -variation analysis, since they exhibit the larger sensitivity coefficients. In the spectrum of Q2348–011 they are not detected due to the H I absorption produced by the additional DLA and another strong absorber at $z \simeq 2.93$. However, the present analysis demonstrates that a complex absorption structure can be successfully modeled by means of the comprehensive fitting method.

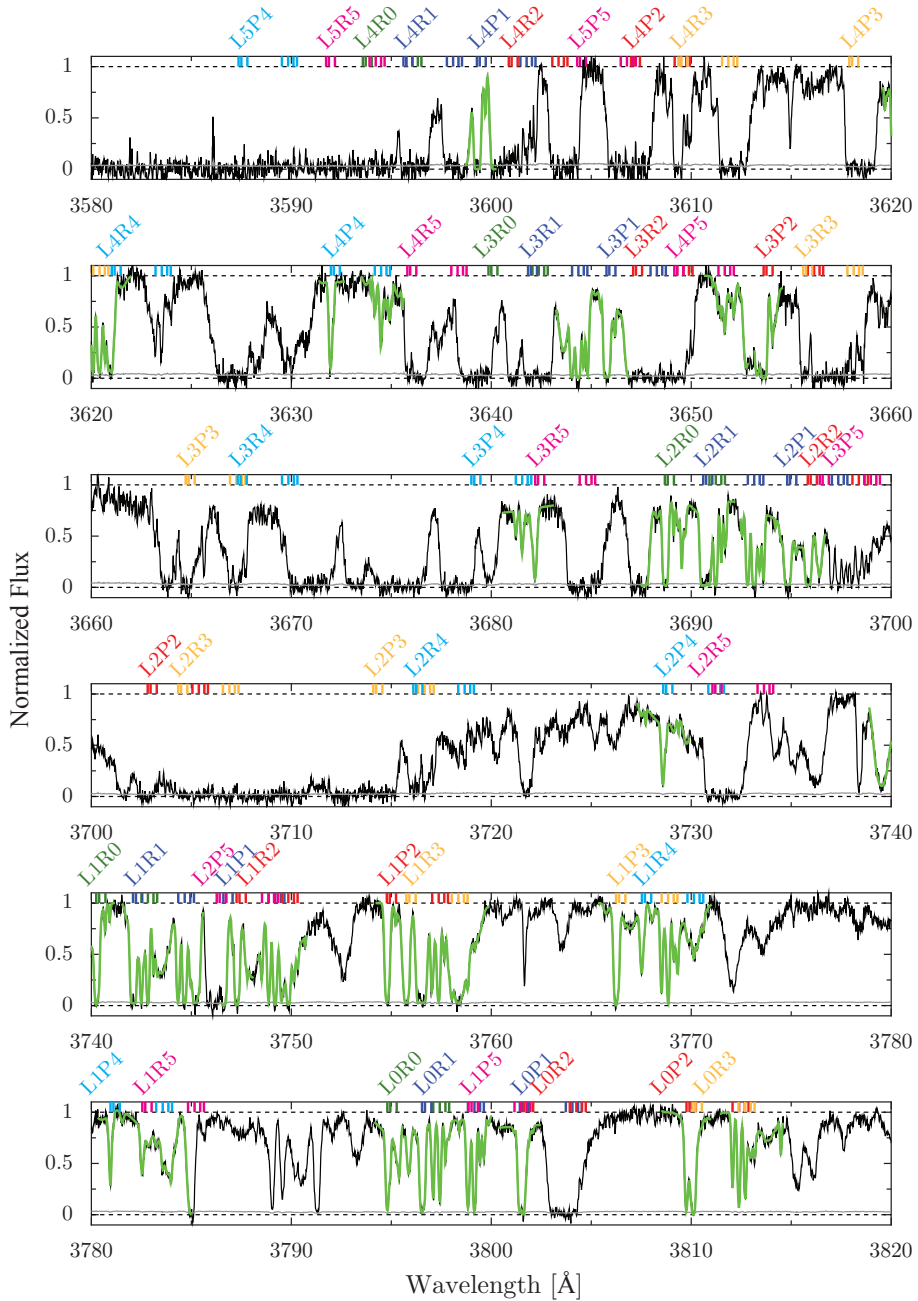
Figure 2.4: *Continued on next page.*

Figure 2.4: *Continued from previous page.* Part of the Q2348–011 spectrum containing H₂ transitions. Transitions from different J levels are labeled in different colours. The associated ticks show positions of the 7 (visually distinguishable) velocity components. The broad absorption feature at 3710 Å is the Lyman- β line of the H I absorber at $z \simeq 2.62$. The break at the shortest wavelengths is due to another H I absorber at $z \simeq 2.93$. The green line shows the fitted regions.

2.5 Conclusions

Molecular hydrogen features present at redshift $z_{abs} \simeq 2.426$ in the line-of-sight to the quasar Q2348–011 were analyzed to detect a possible variation of the proton-to-electron mass ratio on a cosmological timescale. The constraint derived in the analysis is $\Delta\mu/\mu = (-0.68 \pm 2.78) \times 10^{-5}$, showing no indication that μ in this particular absorber is different from μ measured in the laboratory. Although being less accurate than other recent H₂ constraints on $\Delta\mu/\mu$, the result is consistent with those results, which show that $|\Delta\mu/\mu| < 1 \times 10^{-5}$ at $z = 2-3$.

In the sample of known high-redshift H₂ absorbers, the structure of the absorber in the Q2348–011 spectrum is the most complex as it has 7 visually distinguishable velocity components, whilst 12 are justified statistically. The present analysis shows the applicability of the comprehensive fitting method in a case of such a complex structure. However, it also shows that in order to achieve a competitive result on $\Delta\mu/\mu$, the H₂ absorber/spectrum selected for analysis must obey several conditions among which are no occurrence of strong additional absorbers and a sufficiently high S/N ratio.

Acknowledgments

This work is based on observations carried out at the European Southern Observatory (ESO) under program ID 79.A-0404(A) (PI Ubachs), with the UVES spectrograph installed at the Kueyen UT2 on Cerro Paranal, Chile. Additional data from the ESO-archive were used from program ID 072.A-0346(A). JB would like to acknowledge F. van Weerdenburg and A. Malec, for assistance with using VPFIT and fruitful discussions. MTM thanks the Australian Research Council for a QEII Research Fellowship (DP0877998). WU acknowledges support from the Netherlands Foundation for Fundamental Research of Matter (FOM).

Analysis of H₂ absorption toward QSO B0642–5038 for a varying proton-to-electron mass ratio

Bagdonaitė, J., Ubachs, W., Murphy, M. T. & Whitmore, J. B.
Astroph. J. **782**, 10 (2014).

Abstract

Rovibronic molecular hydrogen (H₂) transitions at redshift $z \simeq 2.66$ toward the background quasar B0642–5038 are examined for a possible cosmological variation in the proton-to-electron mass ratio, μ . We utilize an archival spectrum from the Very Large Telescope/Ultraviolet and Visual Echelle Spectrograph (UVES) with a signal-to-noise ratio of ~ 35 per 2.5 km s^{-1} pixel at the observed H₂ wavelengths (335–410 nm). Some 111 H₂ transitions in the Lyman and Werner bands have been identified in the damped Lyman- α system for which a kinetic gas temperature of ~ 84 K and a molecular fraction $\log f = -2.18 \pm 0.08$ are determined. The H₂ absorption lines are included in a comprehensive fitting method, which allows us to extract a constraint on a variation of the proton–electron mass ratio, $\Delta\mu/\mu$, from all transitions at once. We obtain $\Delta\mu/\mu = (17.1 \pm 4.5_{\text{stat}} \pm 3.7_{\text{sys}}) \times 10^{-6}$. However, we find evidence

that this measurement has been affected by wavelength miscalibration errors recently identified in UVES. A correction based on observations of objects with solar-like spectra gives a smaller $\Delta\mu/\mu$ value and contributes to a larger systematic uncertainty: $\Delta\mu/\mu = (12.7 \pm 4.5_{\text{stat}} \pm 4.2_{\text{sys}}) \times 10^{-6}$.

3.1 Introduction

The fact that only 4 % of the energy density content in the universe can be explained within the current framework of particle physics suggests that the standard model is incomplete. In this context, observational attempts to detect variation of fundamental constants serve as one of the guiding tools for theoretical extensions in both cosmology and the standard model. For instance, the theories that intend to unify gravitation with the other three fundamental forces by introducing additional spatial dimensions accommodate cosmologically varying constants quite naturally [10]. Alternatively, additional quantum fields such as the dilaton field may be invoked predicting scenarios of varying constants complying with conservation of energy [129]. Experimental methods are established for probing dimensionless constants such as the fine structure constant $\alpha \equiv e^2/(4\pi\epsilon_0\hbar c)$, which sets the quantum electrodynamical scale, and the proton-to-electron mass ratio $\mu \equiv m_p/m_e$, which is sensitive to the ratio of the chromodynamic scale to the electroweak scale [7].

The redshifted spectra of quasars contain multiple absorption lines arising from cold gas along the line of sight to Earth. These absorption lines serve as a means to probe the high-redshift universe, also making it possible to study varying fundamental constants. In the case of varying μ and α , the absorbers that have the highest neutral hydrogen column densities, known as the damped Lyman- α (DLA) systems, are of particular interest since they are most likely to contain molecular and atomic species that have μ - or α -sensitive energy levels. If μ or α changes with redshift, the relative pattern of the transitions, which is known to a very high accuracy from laboratory experiments, is altered in a specific and calculable manner, different from the overall redshift.

A variation of μ can be detected through the Lyman and Werner bands of molecular hydrogen (H₂, $\lambda_{\text{rest}} < 1150$ Å), which are observable from ground-based observatories if absorption occurs at redshifts $z_{\text{abs}} > 2$ [5]. The proton-to-electron mass ratio at high redshift, μ_z , is measured as a shift with respect to the present-day value μ_0 : $\Delta\mu/\mu = (\mu_z - \mu_0)/\mu_0$. H₂ absorption is detected quite rarely – so far in some 20 DLAs, only few of which are suitable for high accuracy μ analysis, i.e. providing $\Delta\mu/\mu$ constraints at a level of $< 10^{-5}$ [121]. For comparison, the atomic species (Mg, Fe, Cr, Zn *etc.*) sensitive to a variation of α have been detected in some 300 absorption systems which has allowed the constant to be mapped over a broad spatial and temporal range and has yielded an indication of spatial variation [36]. As for μ , the H₂ absorbing systems

toward Q0347–383 at $z_{\text{abs}} = 3.02$, Q0405–443 at $z_{\text{abs}} = 2.59$, Q0528–250 at $z_{\text{abs}} = 2.81$, J2123–005 at $z_{\text{abs}} = 2.06$, Q2348–011 at $z_{\text{abs}} = 2.42$, and HE0027–1836 at $z_{\text{abs}} = 2.40$ have been analyzed thus far at high accuracy [56, 57, 62, 63, 130, 66, 37]. As a result of improving data quality and discussions on appropriate analysis methods, most of the absorbers have been studied more than once, sometimes leading to controversial outcomes. For example, the study by [131] on Q0347–383 and Q0405–443 yielded an indication of μ variation based on a laboratory-based H_2 absorption spectrum using classical spectroscopy. An updated extreme ultraviolet laser spectrum of H_2 by [55] provided extended evidence for such a possible variation of μ . However, a reanalysis of the astrophysical spectra of Q0347–383 and Q0405–443 by [56], using the so-called comprehensive fitting analysis also adopted in the present study, lowered the significance of the effect to a $<2\sigma$ deviation: $\Delta\mu/\mu = (8.2 \pm 7.4) \times 10^{-6}$ and $(10.1 \pm 6.2) \times 10^{-6}$ in the two sightlines, respectively.

In contrast, observations of the J2123–005 with Keck/High Resolution Echelle Spectrometer (HIRES) delivered a μ constraint [62] that was later reproduced by an independent revision (but the same spectral analysis method) using a Very Large Telescope (VLT)/UVES spectrum of the same object [63]. Altogether, the H_2 studies converge in a constraint on the variation of μ at the level of $\Delta\mu/\mu < 1 \times 10^{-5}$ in the redshift range $z = 2\text{--}3$. Given the sensitivity coefficients of H_2 ranging from -0.02 to $+0.05$, a substantially higher accuracy in $\Delta\mu/\mu$ can only be achieved by drastically improving the quality (signal-to-noise ratio (SNR)) of the spectra or by increasing the number of absorbers. The same holds true for the other two weak shifters: HD and CO molecules [49, 50].

As an alternative to H_2 , inversion transitions of ammonia and rotational transitions of methanol can be used for they are, respectively, two and three orders of magnitude more sensitive to $\Delta\mu/\mu$ variation compared to H_2 [94, 99, 100]. Detections of ammonia at redshifts $z_{\text{abs}} = 0.89$ and 0.69 are known presently, yielding 1σ constraints on μ at the level of $(1.0 \pm 4.7) \times 10^{-7}$ and $(-3.5 \pm 1.2) \times 10^{-7}$ [96, 132]. Further observations of the object at redshift $z_{\text{abs}} = 0.89$, a lensing galaxy toward the quasar PKS1830–211, has yielded a detection of methanol resulting in a stringent constraint of $\Delta\mu/\mu = (0.0 \pm 1.0) \times 10^{-7}$ [20]. Although ammonia and methanol are more favorable probes because of high sensitivity, their detections are extremely rare. Thus, molecular hydrogen remains a target molecule for μ variation studies, especially at high redshifts where no constraints from ammonia or methanol are available yet.

In the study presented here, molecular hydrogen transitions at redshift $z_{\text{abs}} = 2.659$ toward the background quasar B0642–5038 are analyzed in the search for a cosmological variation in the proton-to-electron mass ratio μ .

3.2 Method

Molecular hydrogen

For the i th transition of H₂ detected in a cloud at redshift z_{abs} , the observed wavelength is expressed as:

$$\lambda_i = \lambda_i^0 (1 + z_{\text{abs}}) \left(1 + K_i \frac{\Delta\mu}{\mu} \right), \quad (3.1)$$

where λ_i^0 is the rest wavelength of the transition, and K_i is a sensitivity coefficient of the transition, which expresses its shifting power and direction due to varying μ . As for H₂ transitions, we employ sensitivity coefficients K_i defined as

$$K_i = \frac{\mu}{\lambda_i} \frac{d\lambda_i}{d\mu}. \quad (3.2)$$

Note that this definition yields a different sign than usually adopted for the transitions in the radio domain, where a relation is defined in terms of frequency: $\Delta\nu/\nu = K_i \Delta\mu/\mu$. Nevertheless, the sign of $\Delta\mu/\mu$ remains unaffected, that is, direct comparison of the optical and radio constraints is possible. From Eq. (3.1) it follows that from two transitions of different sensitivities, one can determine both the redshift and $\Delta\mu/\mu$. In practice, it is desirable to use as many H₂ transitions as possible since the cumulative signal from multiple transitions is necessary to balance relatively small sensitivity coefficients. Compared to the uncertainties of line positions in the quasar spectrum, the laboratory wavelengths of H₂ at accuracies $\Delta\lambda/\lambda \sim 5 \times 10^{-8}$ can be considered to be exact for our purpose [133]. The K_i coefficients of H₂ have been calculated within a semi-empirical framework ([44], used in present analysis), including effects beyond the Born–Oppenheimer approximation, and from ab initio methods [43]. The K_i values from these two approaches are in agreement within 1%. A comprehensive list of laboratory wavelengths, K_i coefficients, oscillator strengths, and damping parameters of H₂/HD transitions is provided by [134] and implemented in this work (also see Fig. 3.1).

Fitting method

In this study we employ a fitting technique that relies on a number of physical assumptions allowing for simultaneous modeling of all H₂ transitions and nearby H I lines at once. This method is known as the “comprehensive fitting method” to distinguish it from a “line-by-line” method, in which, as its name suggests, each transition is fitted independently of the others. The former technique allows us to include more transitions than the latter, as the fitting of the surrounding Lyman- α forest is readily possible. Also, the line-by-line method

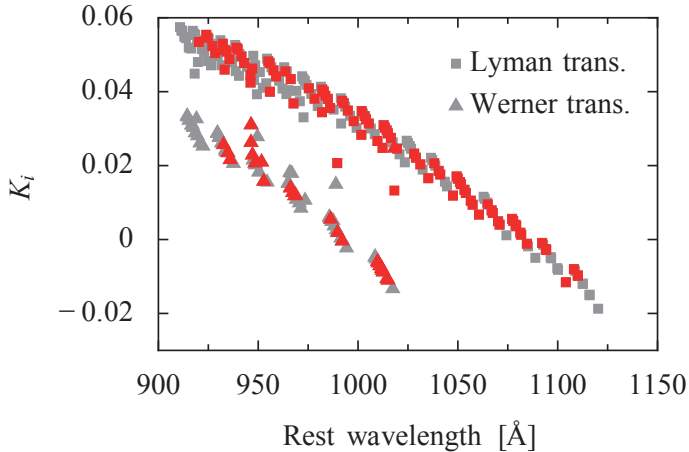


Figure 3.1: Sensitivity coefficients K_i of the Lyman and Werner transitions of H_2 plotted against the rest wavelength. The transitions that were suitable for the $\Delta\mu/\mu$ analysis are marked in red.

may not be applicable for the H_2 absorbers with complex profiles (multiple H_2 clouds distributed close to each other in velocity space). A more detailed comparison of these two fitting approaches is outlined by [56] and [62].

In short, the analysis of H_2 absorption spectra can be described as a three-step process:

1. selection of potentially usable transitions,
2. setting up and refining of the fit,
3. μ derivation and testing.

The analysis starts from visual inspection of the spectrum. The goal is to compose a list of spectral segments each containing an H_2 line and some surrounding buffer region so that any overlapping non- H_2 feature can be modeled too. Quite frequently two or more adjacent H_2 lines are included in a single region when they are too close to be fitted separately. Being distributed over the Lyman- α forest, most of the H_2 transitions unavoidably overlap with H I lines. In some cases a strongly saturated H I absorption may render overlapping H_2 line(s) useless, in which case they are neglected. Additionally, some H_2 transitions can be excluded because of an overlap with narrow metal or unidentified lines if these are unconstrainable (see Section 3.4). The number of selected H_2 lines is usually in the range between 40 and 100.

Once the list is complete, the nonlinear least-squares Voigt profile fitting program VPFIT 9.5¹ is used to model the absorption lines. A Voigt profile represents an absorption line that is broadened by Doppler and Lorentzian mechanisms, and convolved with an instrumental profile (assumed to be Gaussian). The Doppler broadening is caused by the thermal (or large-scale turbulent) motion of the molecules/atoms, while the Lorentzian broadening is due to the finite lifetimes of the excited states. All H₂ and surrounding neutral hydrogen lines are modeled simultaneously. For each transition, a Voigt profile is assigned by providing three adjustable parameters: the redshift of the transition, z , the column density, N , and the velocity width, b . Initial user-supplied parameter guesses for the considered lines are fed to VPFIT, which finds the best match between the model and data by minimizing the goodness-of-fit parameter χ^2 . At each iteration, VPFIT checks the change in the relative χ^2 and reports convergence once an improvement tolerance is met. The stopping criterion, the stepping size for each of the free parameters, and their limits are user defined. Further, the model is refined manually by adding or removing lines (i.e., H₂, H I Lyman- α , and/or metallic ion transitions) and again fitted with VPFIT. This process is repeated until a statistically acceptable fit is achieved. There are several main guidelines for a statistically acceptable model:

- The residuals of each fitted region should be well behaved; that is, they should be free from nonrandom trends. This is verified by inspecting each individual region by eye and by constructing a composite residual spectrum (CRS), which is an even more sensitive tool for systematic fitting problems. To compose a CRS, we select the cleanest H₂ transitions, normalize their residuals (fit minus data) by the flux error, and shift them to a common redshift/velocity scale, where they are averaged together. If any systematic underfitting is present, it becomes ‘amplified’ in the CRS.
- A statistically adequate fit should have a χ^2 per degree of freedom, χ^2_ν , around 1. For the entire fit with ν degrees of freedom,² a χ^2/ν is reported by VPFIT. Competing models can be rated according to their relative values of χ^2_ν .
- The statistically most adequate model has the lowest Akaike information criterion (for finite sample sizes abbreviated AICC; [136]). The AICC is

¹Developed by B. Carswell et al.; <http://www.ast.cam.ac.uk/~rfc/vpfit.html>. We use an upgraded version of VPFIT 9.5 in which the Gauss-Newton optimization algorithm is augmented with the Levenberg-Marquardt algorithm, and computing can be done in parallel on multiple cores. These changes were implemented by J. King (UNSW).

²The degrees of freedom in VPFIT are assumed to be $\nu = n - p$ where n is the number of data points fitted and p is the number of free parameters. However, ν is not defined in such way for a non-linear model. The rationale for this assumption was discussed by [135].

a method to validate the addition of absorption lines (or more often in our case, velocity components (VCs) of H₂). It is defined as:

$$\text{AICC} = \chi^2 + 2p + \frac{2p(p+1)}{n-p-1} \quad (3.3)$$

where n is the number of data points fitted and p is the number of free parameters. When comparing two models, the model with a lower AICC is statistically preferred. More precisely, $\Delta\text{AICC} > 5$ is considered strong evidence and $\Delta\text{AICC} > 10$ is considered very strong evidence for choosing the model with a lower AICC.

The number of so-called VCs is an important ingredient in deciding which model is the best to represent a H₂ spectrum. The light coming from a quasar can be absorbed by multiple H₂ clouds in the DLA (or a single cloud can contain clumps with varying density, turbulence, and temperature), resulting in multiple spectral features for every H₂ transition. At first, the number of VCs is estimated by eye. Then, once the initial model is fitted with VPFIT, more H₂ components might be added if the residuals show any hints of underfitting. VPFIT rejects the added components if data do not support them. As explained above, the necessity to include more components is also assessed from the behavior of χ^2_ν and AICC and the residuals: if these parameters improve, the model is considered more adequate. One should be cautious to not to underfit: it has been shown that underfitting is more prone to cause biases in the $\Delta\mu/\mu$ or $\Delta\alpha/\alpha$ constraints than overfitting [95, 127].

As mentioned before, each Voigt profile is described by three free parameters. By employing the comprehensive fitting method, we tie the free parameters among different transitions. For a single VC of H₂ the following physical restrictions are imposed:

- the same column density for all transitions from a single J level,
- the same z parameter for all transitions,
- the same turbulent b parameter for all transitions.

Some assumptions can be relaxed if a reasonable fit cannot be achieved, but as a rule, we aim to base our fit on as much molecular physics information on the H₂ molecule as possible. Besides the free parameters, a Voigt profile for each transition involves three fixed parameters that are obtained from the molecular physics: rest wavelength λ_i , oscillator strength I_i , and damping parameter Γ_i .

Once the model is optimized, the last free parameter, $\Delta\mu/\mu$, is introduced. A single $\Delta\mu/\mu$ parameter allows relative shifting of the H₂ transitions in accordance with Eq. (3.1). It is important to introduce this fourth parameter

only after the model is finalized because, otherwise, it can acquire a false value to accommodate imperfections of the fit. The very last step is to test how sensitive the derived $\Delta\mu/\mu$ constraint is to the physical assumptions and fitting choices made. These tests can include μ constraints derived from various data cuts: separate J levels, separate Werner transitions and Lyman transitions, regions with no overlapping metal lines, a fit with no assumption about b in different J levels, etc.

3.3 Data

The spectrum of QSO B0642–5038 (RA 06^h43^m27^s.0024 Dec $-50^{\circ}41'12''804$, J2000, visible magnitude $V = 18.5$) was obtained on VLT/UVES under three different programs (their IDs along with the observational settings are listed in Table 3.1). A concise report on the observations was given by [58]. All raw science and calibration data were retrieved from the publicly available European Southern Observatory (ESO) archive.³ The total exposure time of the selected data makes up 22.4 hr. The combined spectrum covers wavelengths from 330 to 1040 nm with two gaps due to separation between the CCDs at 452.1–461.9 and 842.5–856.9 nm. The ratio of average seeing to slit width is 1''. More than half of the exposures were followed immediately by the ThAr calibration (so-called attached ThAr calibration), thereby minimizing the possibility that the optical system can be disturbed by the grating reset. Most of the science frames were obtained with a slit width of 1'', which with 2×2 on-chip binning translates to an instrumental velocity resolution of $\sigma_v \simeq 3.1 \text{ km s}^{-1}$ in the blue part and $\simeq 3.3 \text{ km s}^{-1}$ in the red part (resolving powers $R \sim 41\,000$ and 39 000, respectively). However, the target is a point source, and unlike the calibration lamp, which illuminates the entire slit, it only covers the central part of the slit; thus, a better resolution is expected. Here, we adopt a resolution of $\sigma_v \simeq 2.9 \text{ km s}^{-1}$, which is $\sim 6\%$ better than the formally derived value.

We used the ESO UVES Common Pipeline Language software suite to optimally extract and calibrate the echelle orders, and an open-source, publicly available, custom program UVES_POPLER⁴ to combine multiple exposures into a single, one-dimensional, normalized spectrum on a vacuum-heliocentric wavelength scale. The Pipeline first bias corrects and flat fields the quasar exposures. It then constrains a physical model of where the quasar light is expected to fall on the CCDs with the aid of quartz and ThAr exposures taken through a pinhole instead of a standard slit. The quasar light is then separated from the background and extracted using an optimal extraction method. The ThAr flux (from the calibration frame taken with the same slit as the quasar)

³ESO Archive is accessible via: http://archive.eso.org/eso/eso_archive_main.html

⁴http://astronomy.swin.edu.au/~mmurphy/UVES_popler

was extracted with the same optimal weights derived from the corresponding quasar exposure. The selection of ThAr lines and the establishment of a wavelength solution followed the method described in [126]. UVES_POPLER takes the pixel-space flux spectra from each order of each exposure and disperses all off them onto a common log-linear wavelength scale with a dispersion bin of 2.5 km s^{-1} . Before redispersion, the wavelength solution for each exposure (established from its corresponding ThAr calibration frame) was corrected from air to vacuum using the [137] formula and placed in the heliocentric reference frame using the time of the midpoint of the exposure's integration as a reference. The method of combining the exposures is based on the relative flux scaling between all available overlapping orders weighted by their inverse variance. When combining these scaled orders in this weighted fashion, UVES_POPLER applies an automated algorithm for cosmic ray rejection while other spectral artifacts are inspected and removed manually. The continuum is fitted manually with low-order polynomials. Small constant or linear local changes of the continuum and corrections to zero level are permitted in later stages of the analysis.

3.4 Analysis

Damped Lyman- α system in the QSO B0642–5038 spectrum

The quasar is located at redshift $z = 3.09$ thereby defining the extent of the Lyman- α forest. The quasar radiation is cut off at the shortest recorded wavelengths since a DLA at redshift $z = 2.659$ produces the Lyman break at $< 335 \text{ nm}$. The H_2 lines associated with the DLA are spread in the range from 335 to 410 nm. The SNR of the continuum at the center of this range ($\sim 370 \text{ nm}$) is 35 per 2.5 km s^{-1} pixel. The column density of the neutral hydrogen contained by the DLA is $\log N = 20.95 \pm 0.08 \text{ cm}^{-2}$ [58].

Creating and selecting the most adequate absorption model

We detect molecular hydrogen transitions up to rotational levels with $J = 4$. In total there are ~ 250 potentially useful Lyman and Werner transitions from $J \leq 4$ and vibrational levels $v \leq 18$ (Lyman) and $v \leq 5$ (Werner). We select those H_2 transitions that are neither overlapped by saturated H I nor too weak, as suitable for the analysis. Altogether, 72 regions have been selected, containing a total of 111 H_2 transitions (see Table 3.2; Fig. 3.9 to 3.14 display the spectrum with selected transitions). Each of the H_2 regions is inspected for possible intervening metal lines. The redshifts of absorbing systems with metals in this sightline are determined by identifying the lines in the spectrum redward from the Lyman- α emission of the quasar. Some C IV systems could

3. ANALYSIS OF H₂ ABSORPTION TOWARD QSO B0642–5038

Table 3.1: ESO archival data of the B0642–5038 and Ceres observations with VLT/UVES. The total combined integration time on the B0642–5038 makes up 22.4 hrs in each arm, 14.4 hrs of which have the attached ThAr calibration. The CCD binning mode was 2×2 for all B0642–5038 frames. Airmasses were in the range between 1.113 and 1.562. For Ceres, HD28099, and HD76151 the binning mode was 1×1.

Program ID	Obs. date	Blue/red [nm]	Slit ['']	Integr. time [s]	Seeing ['']	ThAr cal.
B0642–5038						
073.A-0071(A)	2004-09-17	390/580	1.2	5500	1.89	Nonatt.
	2004-09-18	390/580	1.2	6000	1.90	Nonatt.
	2004-09-19	390/580	0.8	6000	1.00	Nonatt.
074.A-0201(A)	2004-10-09	390/850	0.8	5800	0.60	Nonatt.
	2004-10-10	390/850	0.8	5500	0.37	Nonatt.
080.A-0288(A)	2007-12-11	390/564	1.0	3725	1.00	Att.
	2008-01-03	390/564	1.0	3725	0.91	Att.
	2008-01-04	390/564	1.0	3725	1.77	Att.
	2008-01-04	390/564	1.0	3725	1.66	Att.
	2008-01-04	390/564	1.0	1389	1.69	Att.
	2008-01-06	390/564	1.0	2104	1.24	Att.
	2008-01-06	390/564	1.0	3725	1.24	Att.
	2008-01-06	390/564	1.0	3725	1.08	Att.
	2008-01-07	390/564	1.0	3725	0.84	Att.
	2008-01-13	390/564	1.0	3725	1.00	Att.
	2008-01-16	390/564	1.0	3725	0.85	Att.
	2008-02-06	390/564	1.0	3725	0.82	Att.
	2008-02-07	390/564	1.0	3725	0.90	Att.
	2008-02-09	390/564	1.0	3725	0.80	Att.
	2008-02-10	390/564	1.0	3725	0.81	Att.
Ceres						
080.C-0881(B)	2007-12-05	346	1.0	2850	1.32	Nonatt.
HD28099						
380.C-0773(A)	2008-01-11	390/564	0.7	264	1.27	Nonatt.
	2008-01-11	390/564	0.7	264	1.21	Nonatt.
HD76151						
380.C-0773(A)	2008-01-11	390/564	0.7	67	0.69	Att.

be found blueward too. All of them are listed in Table 3.3. We identify seven H_2 transitions that are overlapped by metal lines and several more that are situated next to some narrow unidentified lines. To constrain the relevant metal transitions three more regions containing their counterparts in the red part of the spectrum are added to the region sample. For instance, the H_2 transitions L2P(2) and L2R(3), redshifted to 3954–3958 Å, are overlapping with a Fe II transition ($\lambda_{\text{rest}} = 1081.87 \text{ \AA}$) of the DLA. To constrain the absorption of Fe II, we use a different Fe II transition that is outside the Lyman- α forest ($\lambda_{\text{rest}} = 1608.45 \text{ \AA}$).

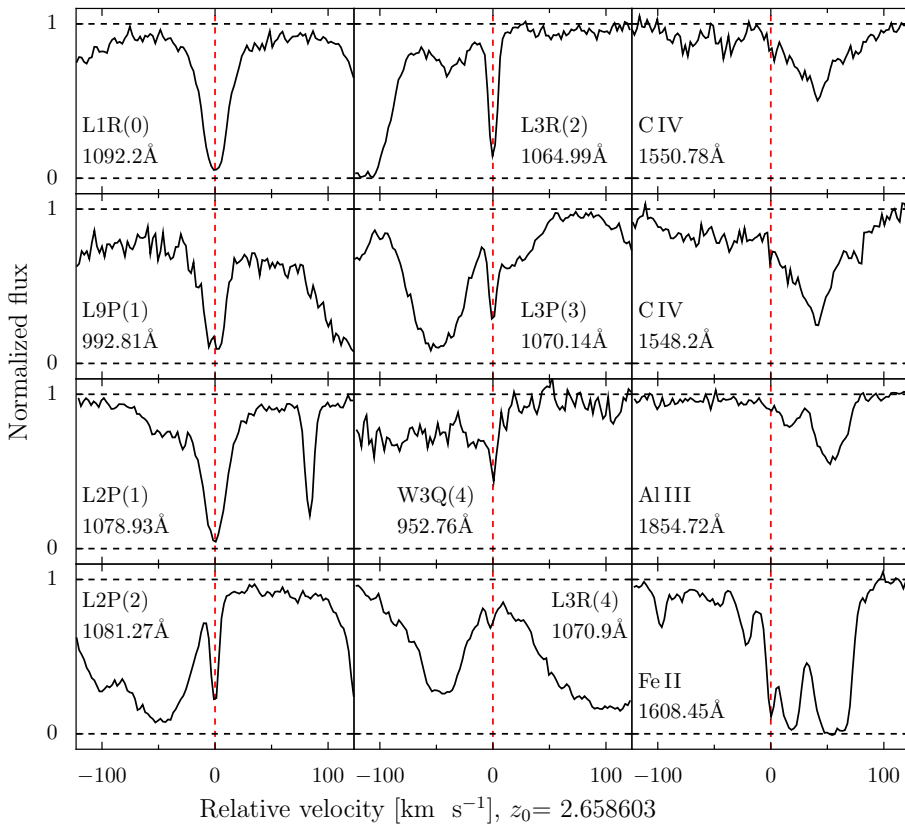


Figure 3.2: Some of the H_2 and metal transitions associated with the DLA at $z \sim 2.659$, displayed on a velocity scale. The red dashed line is centered at the redshift of H_2 absorption. The CIV, Al III, and Fe II profiles show multiple absorption features spread over 200 km s^{-1} .

3. ANALYSIS OF H₂ ABSORPTION TOWARD QSO B0642–5038

Table 3.2: List of the H₂ transitions used in the present study. The underlined transitions are overlapped by narrow lines of known or unknown origin, and the corresponding regions are excluded in one of the tests.

J level	Lyman transitions	Werner transitions	n_{trans}
$J = 0$	L0R0, L1R0, <u>L2R0</u> , L4R0, L7R0, L8R0, L14R0, L17R0	W3R0	9
$J = 1$	L0P1, L1P1, <u>L2P1</u> , <u>L2R1</u> , L4P1, L4R1, L5P1, L7P1, L7R1, L8P1, L9P1, L9R1, L10P1, L10R1, <u>L12R1</u> , <u>L13P1</u> , <u>L13R1</u> , L14R1, L15P1, L15R1, L16P1, <u>L17R1</u> ,	W0Q1, W2Q1, W3R1	25
$J = 2$	L0R2, L1R2, <u>L2P2</u> , <u>L2R2</u> , L3P2, L3R2, L4P2, L4R2, L5P2, L6P2, <u>L7P2</u> , L7R2, L8P2, L8R2, L9P2, L10P2, <u>L10R2</u> , <u>L11P2</u> , L12P2, L13P2, L15P2, L16P2, L16R2, L17P2, L18P2	W0Q2, W0P2, W1R2, W2Q2, W2P2, W4P2, W3R2	32
$J = 3$	<u>L2R3</u> , L2P3, L3P3, L3R3, L4P3, L4R3, <u>L5R3</u> , L6P3, L6R3, L7P3, L9P3, L10R3, L11P3, L12R3, L13R3, L15R3, L16R3, L17R3	W0R3, W0Q3, W0P3, <u>W1Q3</u> , W3R3, W3P3, W4P3	25
$J = 4$	L1P4, L3R4, L4P4, L4R4, L5P4, L6P4, L8P4, L8R4, L9P4, <u>L10R4</u> , L11P4, <u>L14P4</u> , L15R4, L17P4	W0Q4, W0R4, W1Q4, W2R4, W3Q4, W4Q4	20
Total			111

Although the H₂ absorption is seen in a single feature upon first inspection (see Fig. 3.2), the possibility of a more complex underlying structure is explored (see Section 3.2 for motivation of doing so). A second VC is added near to the first VC, and fitting is performed with VPFIT. Several fits with various combinations of the initial values for z , b , and N of the two components have been carried out to ensure the robustness of such a model. For each VC, the free parameters are connected to each other as described in Section 3.2. We find that the model with two VC (2 VC) is statistically more preferable than the model with 1 VC (1 VC): it has a χ^2_ν of 1.189 and an AICC of 10165.6, compared to, respectively, 1.193 and 10190.4 for the 1 VC model. However, the additional VC, present in $J = 0$ and 1 transitions only, is very weak (a column density of some four orders of magnitude lower than the main component is found) and its position has a very large uncertainty (see Table 3.4) that later translates to a minor increase in the uncertainty of $\Delta\mu/\mu$. The CRS of the 1 VC model does not show any significant underfitting (see Fig. 3.3). Attempts to compose a stable 3 VC model were unsuccessful. Thus, on the basis of the statistical parameters, we adopt the 2 VC model as fiducial but we perform further testing for robustness and consistency on both 1 VC and 2 VC models since the second VC is very weak.

Before proceeding with consistency tests focused on a μ -variation analysis, we use the measured column densities of H₂ to estimate some basic characteristics of the absorbing cloud. The column densities of different J transitions of H₂ provide a measure of the gas temperature in the cloud if the observed populations are in thermodynamic equilibrium and follow Boltzmann’s law. The excitation temperature is defined with respect to the $J = 0$ level via: $N_J/N_0 = g_J/g_0 \times e^{-E_{0J}/kT_{0J}}$. In Galactic diffuse clouds, the T_{01} temperature is regarded as a kinetic temperature of the gas [138]. The higher levels are often populated in excess of the Boltzmann law, implying that besides collisions there are other processes involved, such as cascades following UV or formation pumping or, alternatively, shocks or turbulence effects (see, e.g., [139]). From the H₂ absorption in the DLA at $z = 2.659$ toward B0642–5038, we find a kinetic temperature of $T_{01} \simeq 84$ K, which is consistent with that in the Galactic interstellar medium [140], while the levels at $J > 2$ indeed show higher temperatures of 100–140 K (see Fig. 3.4). Both measured temperatures are consistent with what was found in other DLA studies (e.g., [120]). For the temperature calculations we used column densities from the 1 VC model.

The total molecular column density amounts to $\log N(\text{H}_2) = 18.48 \pm 0.01$ cm⁻². Given the neutral content of $\log N(\text{H I}) = 20.95 \pm 0.08$ cm⁻² [58], a molecular fraction of $\log f = -2.18 \pm 0.08$ is derived. Only 15% of DLAs with detected H₂ have a molecular fraction in the range $-4 < \log f < -1$ [81]. For comparison, in the Galactic sightlines of similar neutral hydrogen density, typical values for the molecular hydrogen are $\log N(\text{H}_2) > 19$ [140].

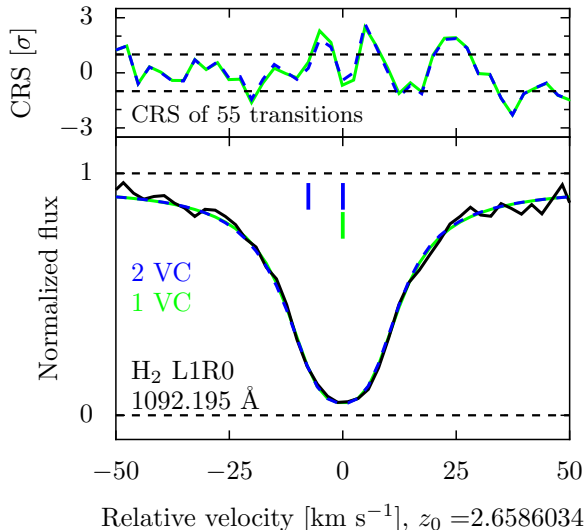


Figure 3.3: The composite residual spectrum (top) and an example of H₂ absorption centered at $z = 2.658603$. Fifty-five H₂ transitions were used to compose the composite residual spectrum. The black horizontal dashed lines in the composite residual plot show $\pm 1\sigma$ boundaries. The green line shows composite residuals (top) and a corresponding fit from the 1 VC model, and the blue line refers to the 2 VC model.

Consistency tests

The results of the consistency tests discussed below are displayed in Fig. 3.7. We start from a generic fit that includes all suitable transitions (111 in total) and data, i.e., all exposures independent of how they were calibrated (attached ThAr or not). Unless stated otherwise, in all the tests the z and b parameters are assumed to be the same for all J levels, and the column density N is the same for all transitions from a single J level for a single VC. The fitting solution is found through an iterative process, where at each iteration VPFIT checks the change in the relative χ^2 and stops when a stopping criterion is reached. We used a stopping criterion of $\Delta\chi^2/\chi^2 < 10^{-7}$ for a fine mode of fitting and $< 10^{-6}$ for a coarse fitting. Whenever possible, we used the fine fitting mode, but in some cases this gave very slow convergence of the fit, and the coarse mode gave faster, more reliable results from a single minimization run of VPFIT. The 1 VC generic model delivers $\Delta\mu/\mu = (16.9 \pm 4.4_{\text{stat}}) \times 10^{-6}$, while the 2 VC generic model results in $\Delta\mu/\mu = (17.1 \pm 4.5_{\text{stat}}) \times 10^{-6}$; further tests and comparisons are made with respect to these results from generic tests.

Table 3.3: Metal absorbers in the line of sight toward the B0642–5038

Redshift	Species
1.545 ^a , 1.647, 1.691, 1.852, 1.987, 2.031, 2.126, 2.204, 2.348, 2.423, 2.500, 2.912	C IV
1.561	C I, C IV
2.029	C IV, Si IV, Si III
2.082	C IV, Si IV, Si III
2.510	C IV, N V, Si IV, O VI
2.521	C IV, Al II
2.659 ^b	C IV, C II, Al III, Si II ^a , Si III, Si IV, P II, Cr II, Ni II, Zn II, Al II, Fe II ^a , Ni, O I, C I, C III, C II*
2.899	C IV ^a , C III ^a , N V, Si IV, Si III, S IV, O VI
2.955	C IV, C III, O VI
2.967	C IV, O VI

^a Metal absorptions overlapping H₂ (or those used to constrain them).

^b The DLA system presently analyzed for μ -variation.

Table 3.4: Column densities, Doppler widths, and redshifts of the fitted H₂ transitions (together with 1 σ statistical uncertainties) as reported by VPFIT.

	1 VC model		2 VC model	
	$z = 2.6586026(4)$	$z_1 = 2.6586030(4)$	$z_2 = 2.65851(12)$	
	$b = 1.57 \pm 0.04$	$b_1 = 1.58 \pm 0.04$	$b_2 = 12.5 \pm 6.3$	
	[km s ⁻¹]	[km s ⁻¹]	[km s ⁻¹]	
J level	$\log N$ [cm ⁻²]	$\log N$ [cm ⁻²]	$\log N$ [cm ⁻²]	
$J = 0$	18.15±0.01	18.13±0.02	13.97±0.62	
$J = 1$	18.20±0.01	18.19±0.01	13.74±0.61	
$J = 2$	16.21±0.07	16.19±0.07	-	
$J = 3$	15.04±0.05	15.03±0.05	-	
$J = 4$	13.72±0.03	13.71±0.03	-	

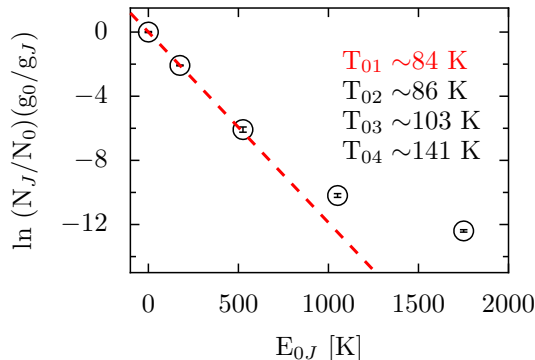


Figure 3.4: Excitation diagram for H₂ in the DLA at $z = 2.659$. The column densities are weighted with a factor $g_J = g_N(2J + 1)$, where g_N is the nuclear spin weight that has the value $g_N = 1$ for even values of J and $g_N = 3$ for odd values of J . The slope of a straight line gives $1/T_{01}$. The uncertainties of $T_{0,J}$, as derived directly from measured column densities, are of the order of 3–5 K.

In all the tests presented here, the transition oscillator strengths were kept fixed to the values established for the H₂ molecule. Note that the line intensities were derived in a model involving interactions between electronic states $B^1\Sigma_u^+$, $C^1\Pi_u$, $B^1\Sigma_u^+$, and $D^1\Pi_u$ and intensity borrowing [141]; no accurate transition oscillator strengths have been experimentally determined. In contrast, in previous analyses by [62] and [57] for some specific transitions the oscillator strengths had to be adapted in the fitting procedure. In a study of three H₂ absorbing systems [56] varied column densities (including a product with an oscillator strength) for each of the lines separately. In the present study we stuck as close as possible to the established molecular physics of H₂ and found no need to adapt oscillator strengths.

Isolating low- and high- J transitions

In this particular absorber, the $J = 0, 1$ and $J = 2-4$ transitions differ in that the former are saturated ($\log N > 18 \text{ cm}^{-2}$; Table 3.4), unlike the latter. For this reason, if the velocity structure is underfitted (VCs missing), the lower- J level transitions would be affected more than the higher- J transitions because any missing components will be weak even in the low- J transitions and completely negligible in the high- J transitions. In other words, the low J transitions can be more misleading when determining $\Delta\mu/\mu$ than the high J transitions. For this reason, two more $\Delta\mu/\mu$ constraints are derived separately from the $J = 0, 1$ transitions (34 in total) and $J = 2-4$ transitions (77 in to-

tal) of the generic fit. Note, that the tests are performed not by excluding unwanted transitions but by leaving their $\Delta\mu/\mu$ parameter fixed to zero. As in the generic tests, the z and b parameters are assumed to be the same for all J levels for a single VC, and the column density N is the same for all transitions from a single J level. Constraints delivered from the $J = 0, 1$ transitions are $\Delta\mu/\mu = (7.9 \pm 6.2_{\text{stat}}) \times 10^{-6}$ and $\Delta\mu/\mu = (18.7 \pm 7.2_{\text{stat}}) \times 10^{-6}$ for the 1VC model and 2VC model, respectively. If only the $J = 2-4$ transitions are used, the 1VC and 2VC model deliver $\Delta\mu/\mu = (17.7 \pm 6.1_{\text{stat}}) \times 10^{-6}$ and $\Delta\mu/\mu = (14.1 \pm 6.0_{\text{stat}}) \times 10^{-6}$, respectively. As it can be expected in the case of underfitting, the 1VC constraint from the $J = 0, 1$ transitions seems to be slightly off from the other constraints, including those from the generic fits.

Separating Lyman and Werner transitions

A test is performed where a $\Delta\mu/\mu$ constraint is delivered from either only Lyman band or only Werner band transitions. For the 1VC model we find $\Delta\mu/\mu = (15.5 \pm 4.5_{\text{stat}}) \times 10^{-6}$ from the Lyman transitions and $\Delta\mu/\mu = (14.3 \pm 17.7_{\text{stat}}) \times 10^{-6}$ from the Werner transitions. For the 2VC model it is, respectively, $\Delta\mu/\mu = (15.9 \pm 4.6_{\text{stat}}) \times 10^{-6}$ and $\Delta\mu/\mu = (10.1 \pm 17.7_{\text{stat}}) \times 10^{-6}$. The derived constraints are in good agreement with each other and with the generic fit results. However, the uncertainty of the constraints from Werner transitions is much larger than the one from Lyman transitions because there are around four times fewer Werner transitions in the fit. What the dominance of Lyman transitions over the fiducial result can imply is discussed in Section 3.5. Note again that the tests are performed not by excluding unwanted transitions but by leaving their $\Delta\mu/\mu$ parameter fixed to zero.

Excluding problematic regions

Seventeen H_2 transitions are blended with narrow lines, some of which are due to known metal absorbers, while others are unidentified. If the interloping lines are fitted inadequately, an effect in $\Delta\mu/\mu$ can be expected. To test this presumption, a fit without the regions containing these transitions is performed. For the 1VC and 2VC models the fitted subsample delivered, respectively, $\Delta\mu/\mu = (18.3 \pm 4.8_{\text{stat}}) \times 10^{-6}$ and $\Delta\mu/\mu = (15.9 \pm 4.9_{\text{stat}}) \times 10^{-6}$. The resulting constraints are in agreement with those from the generic fit which leads to a conclusion that contamination by metallic transitions does not affect positions of the H_2 transitions substantially.

Untying free parameters among different J levels

In the tests described above, redshifts and widths of the H_2 transitions were assumed to be the same, independent of J level. To test the validity of this

assumption, the low- and high- J transitions are decoupled from each other and allowed to assume different z and b values to verify if the two groups deliver consistent constraints. One possibility why this may not be the case is a spatial inhomogeneity in temperature in the absorbing cloud. Also, by performing such a test we can test the possibility of an underfitted velocity structure as in Section 3.4. For the 1 VC and 2 VC models this test delivered, respectively, $\Delta\mu/\mu = (15.6 \pm 4.5_{\text{stat}}) \times 10^{-6}$ and $\Delta\mu/\mu = (15.5 \pm 4.6_{\text{stat}}) \times 10^{-6}$. These constraints agree within uncertainties with those from the generic fits which means that in the case of a relatively simple velocity structure of H₂, releasing some assumptions may not affect the $\Delta\mu/\mu$ considerably.

Fitting parts of the spectrum

In the presence of a long-range monotonic distortion of the wavelength scale, a significant effect on $\Delta\mu/\mu$ can potentially be generated, especially if only Lyman or only Werner transitions were fitted since the transitions in each band have monotonically increasing K_i coefficients toward the blue wavelengths. The degeneracy is possibly broken if both Lyman and Werner transitions are fitted in a common wavelength interval because, e.g., $K_i(\text{Werner}) = -0.01$, while $K_i(\text{Lyman}) = 0.03$ at 1010 Å (see Fig. 3.1). On the other hand, the range where only Lyman transitions are present has a better SNR and therefore can have a substantial weight in the comprehensive fit.

We separate and fit the part of the spectrum where both Lyman and Werner transitions are present, i.e. blueward from 3714 Å, and as a complementary test we also fit the excluded Lyman transitions (redward from 3714 Å). For the 1 VC test, the former test results in $\Delta\mu/\mu = (12.1 \pm 6.6_{\text{stat}}) \times 10^{-6}$, and the latter $\Delta\mu/\mu = (15.4 \pm 9.9_{\text{stat}}) \times 10^{-6}$. For the 2 VC test, the results are $\Delta\mu/\mu = (11.1 \pm 6.7_{\text{stat}}) \times 10^{-6}$ and $\Delta\mu/\mu = (17.9 \pm 10.0_{\text{stat}}) \times 10^{-6}$, respectively. If the μ dependence of Werner transitions is removed, the fit (in the blue part) delivers $\Delta\mu/\mu = (10.5 \pm 6.7_{\text{stat}}) \times 10^{-6}$ and $\Delta\mu/\mu = (9.7 \pm 6.8_{\text{stat}}) \times 10^{-6}$ for the 1 VC and 2 VC models, respectively.

Generally, the constraints quoted above do not diverge significantly from those in the generic fit; however, there is a bias all of them can be affected by. In Section 3.4, it was demonstrated that the constraints derived from generic model are dominated by the Lyman transitions because of their disproportionate contribution to the data set. In the test where we disregard Lyman transitions in the red part (38 in total), the Lyman-to-Werner ratio is reduced to 2:1 compared to 4:1 in the generic fit. Thus, this approach should be less biased than the generic one, but it is still dominated by the Lyman transitions.

In Section 3.5 the possibility of long-range distortions is explored further.

3.5 Systematic uncertainty

Calibration residuals

One of the sources of systematic uncertainty is wavelength calibration residuals of ThAr lines. Typically, the residuals have a rms of 70 m s^{-1} ; that is, at any given place in the spectrum the wavelength scale is accurate within 70 m s^{-1} . Usually, more than 10 ThAr lines are detected and multiple H_2 transitions are fitted in each echelle order; therefore, the effect of any systematic trends is reduced to 30 m s^{-1} at most [126]. Given a span in K_i of 0.05, a velocity shift of 30 m s^{-1} translates into a $\Delta\mu/\mu$ shift of 2.0×10^{-6} , applying the following relation: $\Delta v = c\Delta K_i\Delta\mu/\mu$.

Nonattached ThAr

The UVES spectrograph is designed in such way that the grating is repositioned between different exposures. Although the repositioning of the grating should be accurate to within 0.1 pixel [142], the ThAr calibrations can be obtained immediately after science observation, without initiating grating reset, so that potential uncertainties in the wavelength scale are avoided. The bulk of our exposures have attached ThAr calibrations (60 % of the data). To test for possible miscalibration effects, we fit a ‘subspectrum’, a spectrum comprising of only a subset of exposures but composed by the same process as the full spectrum, which includes only these ‘well-calibrated’ exposures. For the SNR reduced from 35 to 32 at 370 nm, the 1 VC model delivers $\Delta\mu/\mu = (16.7 \pm 4.9_{\text{stat}}) \times 10^{-6}$, and the 2 VC model delivers $\Delta\mu/\mu = (16.4 \pm 4.9_{\text{stat}}) \times 10^{-6}$ (also see Fig. 3.7). It can be concluded that the effect on $\Delta\mu/\mu$ due to data with nonattached ThAr is not evident in our case. However, this conclusion cannot be generalized and applied to every UVES spectrum; for example, in the case of varying α studies where just a few transitions are fitted in the spectrum, the effect, if present, might cause considerable shifts.

Intraorder wavelength-scale distortions

[128] showed that intraorder distortions (i.e. distortions of the wavelength scale within echelle orders that repeat from order to order) up to $\sim 100 \text{ m s}^{-1}$ can be expected in VLT/UVES spectra. Thus, a $\pm 100 \text{ m s}^{-1}$ sawtooth wavelength distortion is introduced to each echelle order of the B0642–5038 spectrum using UVES_POPLER before they are combined into a single spectrum for analysis in VPFIT. Then, taking all 111 transitions into account, we perform a fit on a spectrum with the introduced intraorder wavelength-scale distortions. Results of such tests are model dependent, but generally, intraorder distortions are not

expected to be a significant problem for μ -variation analysis, because the H₂ transitions are spread over multiple orders. From the test that we performed on a distorted spectrum, we find a contribution to the systematic uncertainty of $\Delta\mu/\mu$ at the level of 0.6×10^{-6} (see Fig. 3.7). The effect we find here is of the same order as in previous studies where such an analysis was also performed [62, 57, 63].

Uncertainty from spectral redispersion

To compose a final one-dimensional spectrum, several echelle orders are combined by redispersing them onto a common wavelength scale and taking their weighted mean. The rebinning may cause flux correlations between neighboring pixels. Thus, the choice of a wavelength grid can, in principle, affect the measurement of $\Delta\mu/\mu$. To test this, we choose several slightly different grids in the range from 2.3 to 2.7 km s⁻¹ per pixel. The maximal deviation among the resulting $\Delta\mu/\mu$ values is $\pm 3.0 \times 10^{-6}$. This is added to the total systematic uncertainty budget. Previous studies of different H₂ absorbers report deviations in $\Delta\mu/\mu$ due to redispersion in the range from 0.2×10^{-6} [63] to 0.8×10^{-6} [62] for pixel sizes ~ 1.3 km s⁻¹ and to 1.4×10^{-6} [57] for ~ 2.5 km s⁻¹ pixels, like those in the present analysis.

Long-range wavelength scale distortions

The possibility of long-range distortions between the ThAr calibration spectra and quasar spectra recorded with VLT/UVES has been reported recently by [37]. In a study focusing on a μ -variation analysis from H₂ absorption toward HE0027–1836, [37] report significant long-range calibration errors for UVES data, especially strong in exposures taken in 2012. Wavelength distortion errors, when using ThAr spectra for calibration, could, in principle, be produced by differing beam paths and/or slit illumination distributions between the quasar science exposure and the subsequent ThAr calibration exposure. After reflecting from the primary, secondary, and tertiary mirrors, quasar light is directed through a derotator into the UVES enclosure. Once it enters the enclosure, the beam is split by a dichroic into the two arms of the spectrograph: a blue arm and a red arm. Each beam passes through its respective optics, which are: a blue (red) slit, the cross dispersers, several mirrors, and finally lands on the blue (red) CCD(s). The light from the calibration lamp is sent into the UVES enclosure by reflecting from a calibration mirror that is slid into the optical path of the telescope. After entering the enclosure, it interacts with the same optics described above. However, there could be an angular offset between the science and calibration exposures, which would result in slightly differing beam paths through the spectrometer, leading to a

possible wavelength distortion. Also, each slit is illuminated fully by the ThAr lamp, while the quasars are unresolved point sources. Therefore, the quasar and ThAr light may produce different point-spread functions on the CCDs, and if that difference varies across the CCDs, a long-range distortion between the quasar and ThAr calibration may result.

Rahmani *et al.* [37] used a cross-correlation technique to compare UVES spectra of various asteroids taken across several years with a solar spectrum recorded with a Fourier transform spectrometer (FTS). They found long-range velocity slopes which they translated into systematic offsets for $\Delta\mu/\mu$ lying in the range between 2.5×10^{-6} and 13.3×10^{-6} . Prompted by the conclusions of [37], we will later assess long-range wavelength distortions in the B0642–5038 spectrum using the asteroid method.

We first attempt to address the likely sign and magnitude of long-range distortions in the actual B0642–5038 spectra using simulations. In Section 3.4 we discussed the fact that the Werner and Lyman transitions, when fitted simultaneously, can break a possible degeneracy between long-range distortions and $\Delta\mu/\mu$. To illustrate this further we use simulated spectra with distortions introduced following the formalism presented by [62], Section 4.2.2 in their paper. The wavelength scale is compressed to simulate a long-range distortion and the H₂ transitions are shifted to mimic a nonzero $(\Delta\mu/\mu)_{\text{sys}}$. We used the 1 VC generic model to produce simulated spectra with the same S/N ratio as the real quasar spectrum, three different noise realizations in total. Each of these three simulated spectra was distorted to mimic $(\Delta\mu/\mu)_{\text{sys}}$ of -17 and $+17 \times 10^{-6}$ and fitted using the 1 VC generic model including all 111 H₂ transitions. As expected, the $\Delta\mu/\mu$ values returned from fitting agree with $(\Delta\mu/\mu)_{\text{sys}}$ within uncertainties; they also agree within uncertainties when the undistorted simulations (i.e. $(\Delta\mu/\mu)_{\text{sys}} = 0$) were analyzed. In other words, in the relationship $\Delta\mu/\mu = s_1 \times (\Delta\mu/\mu)_{\text{sys}} + b_1$ the coefficient s_1 is close to unity, and b_1 is of the order of $\Delta\mu/\mu$ statistical uncertainty.

In a second step, the same simulated spectra with long-range distortions were used to derive $\Delta\mu/\mu$ constraints separately from the blue and red parts (with a dividing line at 3714 Å as in Section 3.4). To compare the constraints returned from the blue part with those from the red part we use the relationship $(\Delta\mu/\mu)_{\text{red}} - (\Delta\mu/\mu)_{\text{blue}} = s_2 \times (\Delta\mu/\mu)_{\text{sys}} + b_2$. In this case, an s_2 coefficient close to unity means that the blue part is very resistant to the long-range distortions represented by $(\Delta\mu/\mu)_{\text{sys}}$. From our simulated spectra we derive $s_2 \simeq 0.8$. The real quasar spectrum fitted with a 1 VC model returns $(\Delta\mu/\mu)_{\text{red}} - (\Delta\mu/\mu)_{\text{blue}} = (3.3 \pm 11.9) \times 10^{-6}$ (see Section 3.4). Assuming b_2 is negligible (few 10^{-6}), we can estimate the size of a possible linear wavelength distortion in the real spectrum: $(\Delta\mu/\mu)_{\text{sys}} = (3.3 \pm 11.9) \times 10^{-6} / 0.8 = (4 \pm 15) \times 10^{-6}$. The possible distortion itself is not large but it has a large uncertainty which makes the interpretation difficult.

A different way of quantifying long-range distortions is to observe objects with a well-understood spectrum that can then be compared with a reference spectrum. An iodine cell has been used to quantify the calibration differences between the ThAr wavelength solution of quasar spectra observed with the iodine cell in the line of sight and a reference FTS iodine cell spectrum [143, 128]. We use a new implementation of this ‘supercalibration’ method [38], which is similar to the iodine cell. The only practical difference is instead of using the iodine cell spectrum as a reference, we use the solar spectrum. The general procedure for finding a velocity shift v_{shift} between the ThAr solution and the FTS reference spectrum begins by using a science exposure that has been calibrated in the standard way that our quasar exposures were calibrated: (1) take a science exposure, (2) take a ThAr calibration exposure, and (3) solve for the ThAr wavelength solution. After these steps are completed, the supercalibration technique solves for relative velocity shifts between the science exposure’s ThAr wavelength solution and a reference spectrum.

The details of how we implement this supercalibration technique for this paper are as follows. We use the FTS solar spectrum KPNO2010 detailed in [144], which is publicly available,⁵ as our reference spectrum. We chose an archival exposure of the asteroid Ceres taken in 2007 December, a few days before the beginning of the quasar observations (which span the next 2 months, see Table 3.1). Also, we used a number of the solar twin HD28099 and HD76151 spectra observed a month later than Ceres, conveniently close in time to the bulk of the quasar observations (see Fig. 3.5). A 500 km s⁻¹ segment of the spectrum is taken from the asteroid/solar twin science exposure, and an overlapping region of the solar FTS spectrum is taken as the model. The model is modified by the following five-parameter transformation: (1) a single velocity shift, (2) a multiplicative flux scaling factor, (3) an additive flux offset factor, (4) the sigma width of a symmetric Gaussian instrument profile, and (5) a linear continuum slope correction. We minimize χ^2 between the model and the data. The wavelength ThAr corrections found with this supercalibration technique are reported as v_{shift} with the following sign conventions:

$$\lambda_{\text{shift}} = \lambda_{\text{reference}} - \lambda_{\text{ThAr}}, \quad (3.4)$$

$$v_{\text{shift}} = c \times \frac{\lambda_{\text{shift}}}{\lambda}. \quad (3.5)$$

The supercalibration technique is sensitive to both short- and long-range distortions. Since the contribution to the systematic error budget of short-range (intraorder) distortions are quantified in Section 3.5, the long-range distortions remain to be incorporated. A plot of the average v_{shift} per order, with an error

⁵<http://kurucz.harvard.edu/sun/irradiance2005/irradthu.dat>

bar that is the size of the standard deviations, is shown in Fig. 3.5. We fit a linear model of the long-range distortion and use this model in our analysis.

As can be seen from Fig. 3.6(a), a correction derived from the Ceres observations is twice as big as the one from the solar twins. We apply these two corrections to the spectrum of B0642–5038 (1 VC model) and derive, respectively, $\Delta\mu/\mu$ of $(0.7 \pm 4.4_{\text{stat}}) \times 10^{-6}$ and $(12.5 \pm 4.4_{\text{stat}}) \times 10^{-6}$. These values, especially the former, differ substantially from an uncorrected measurement ($\Delta\mu/\mu = (16.9 \pm 4.4_{\text{stat}}) \times 10^{-6}$). As an additional test, we apply the corrections to a simulated spectrum. Similar to what we did before, we used the 1 VC generic model to produce a simulated spectrum with the same SNR as the real quasar spectrum and imposed $\Delta\mu/\mu = 0$. Fitting this spectrum with two different correction values results in $\Delta\mu/\mu$ of $(-10.5 \pm 3.4_{\text{stat}}) \times 10^{-6}$ (larger correction from Ceres) and $(-4.9 \pm 3.4_{\text{stat}}) \times 10^{-6}$ (smaller correction from the solar twins). In both cases, when the corrections are applied to the real and simulated spectrum, the measured $\Delta\mu/\mu$ value is smaller than that from a corresponding uncorrected spectrum (see Fig. 3.6 (b) and (c)). In other words, if the long-range wavelength distortions are neglected, the measured $\Delta\mu/\mu$ will likely be more positive than its actual value. A number of asteroid calibrations taken with UVES over surrounding years agree on the sign of the effect. These offsets are relatively large, exceeding the estimates of statistical uncertainties and other systematic effects [37]. However, an important question to be addressed when making a correction to $\Delta\mu/\mu$ is that of the accuracy of the correction. As can be seen from Fig. 3.6(a), most of the quasar exposures are taken within ± 8 days of the observations of the solar twins, and thus, we further rely on the solar twins in making an adjustment of the fiducial $\Delta\mu/\mu$ measurement; that is, we use $\Delta\mu/\mu = -4.4 \times 10^{-6}$ as a correction. Note also that the same central wavelengths (setting of the dichroic) have been adopted in the observations of the solar twins and quasar, although that is not the case for the Ceres asteroid (see Table 3.1). Nevertheless, we include the latter measurement in the estimation of the $\Delta\mu/\mu$ correction accuracy, which we base on a spread in the derived wavelength correction values over a month’s time (Fig. 3.6(a)). A standard deviation of the averaged correction values equals $\pm 0.7 \text{ m s}^{-1} \text{ nm}^{-1}$, and thus, we fit spectra corrected by $\pm 0.7 \text{ m s}^{-1} \text{ nm}^{-1}$ with respect to the correction from the solar twins ($1.5 \text{ m s}^{-1} \text{ nm}^{-1}$). These corrections result in $\Delta\mu/\mu$ shifts of $\pm 2.0 \times 10^{-6}$ with respect to the results derived from both the real quasar spectrum and the simulated spectrum. Thus, we further add $\pm 2.0 \times 10^{-6}$ to the systematic error budget of $\Delta\mu/\mu$.

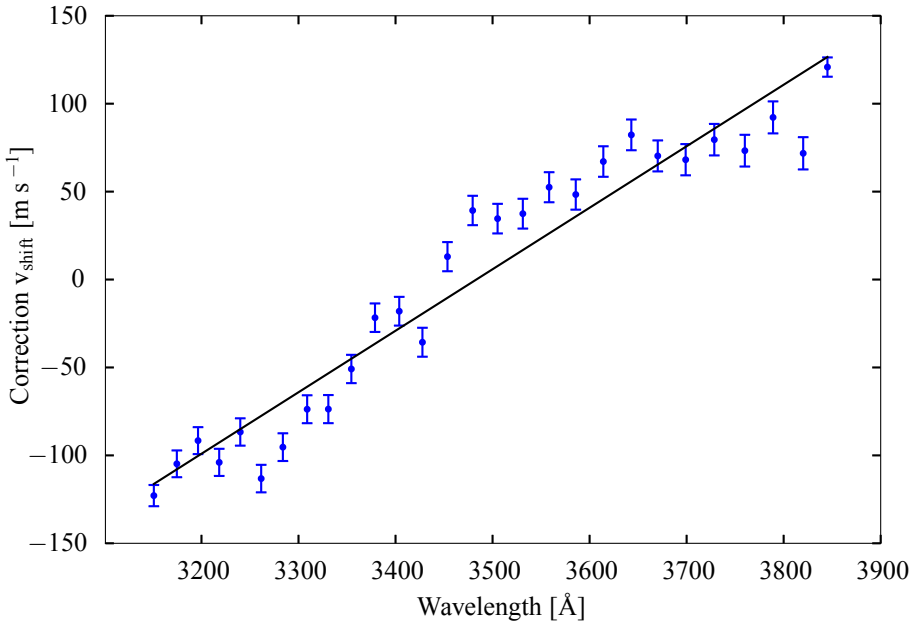


Figure 3.5: Plot of the long-range wavelength distortion found by the supercalibration technique in the Ceres 2007 exposure (orders 5–33). The v_{shift} , as defined in Eq. 3.5, is the correction that needs to be applied to the ThAr wavelength solution to align with the fiducial FTS solar spectrum. We plot the average v_{shift} for each echelle order, and the size of the error bar is the standard deviation of the v_{shift} within that order. The plot has been shifted by a constant velocity to account for radial velocity and slit-offset effects. In other words, the absolute scale is not meaningful, but the relative scale is informative. The equation of the best fit line is $v_{\text{shift}}(\lambda) = A \times \lambda + B$, with $A = 350 \text{ m s}^{-1}$ per 1000 \AA , and $B = -1218.0 \text{ m s}^{-1}$.

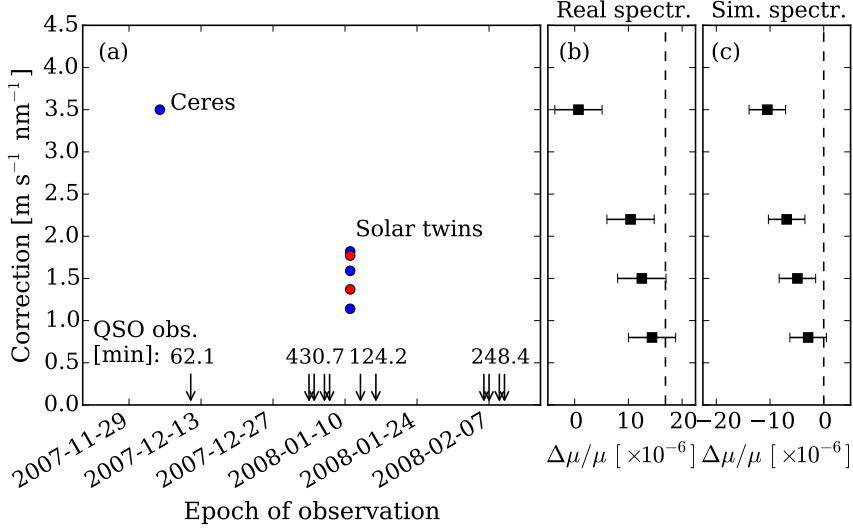


Figure 3.6: (a) Corrections of the wavelength scale, as derived from observations of Ceres and solar twins, are displayed vs. the observing epoch. Blue (red) points refer to corrections of the wavelengths at <450 nm (>450 nm). Quasar observations from program 080.A-0288(A) are marked on the time axis; most of them were conducted around the time when the solar twin spectra were taken. (b) The data points refer to the $\Delta\mu/\mu$ constraints as derived from the B0642–5038 spectrum when wavelength corrections are applied to it (1 VC model). The vertical dashed line shows a $\Delta\mu/\mu$ constraint from an uncorrected spectrum. Applying wavelength corrections results in $\Delta\mu/\mu$ values that deviate from zero less than the one from the uncorrected spectrum. Note that we apply wavelength corrections to the total averaged spectrum and not to the individual exposures. (c) A simulated quasar spectrum is skewed using the same wavelength corrections as in (b). Corrections of this sign result in a $\Delta\mu/\mu$ measurement smaller than the input $\Delta\mu/\mu = 0$ (indicated by the dashed vertical line). A correction of $3.5 \text{ m s}^{-1} \text{ nm}^{-1}$ (implied by Ceres observations) leads to a $\Delta\mu/\mu$ shift from 0 to -10.5×10^{-6} . A correction based on the solar twin ($1.5 \text{ m s}^{-1} \text{ nm}^{-1}$) results in a $\Delta\mu/\mu$ shift from 0 to -4.9×10^{-6} . The uncertainties of the $\Delta\mu/\mu$ constraints are defined by the S/N of the simulated spectrum.

Summary of systematic uncertainty

From the performed tests we estimate four definite contributions to the total systematic error of $\Delta\mu/\mu$: the calibration residuals can contribute up to 2.0×10^{-6} , the intraorder distortions can introduce an error of 0.6×10^{-6} , an effect of 0.7×10^{-6} can be expected due to nonattached ThAr calibrations, and the spectral redispersion may introduce an error of 3.0×10^{-6} . Adding these four contributions in quadrature, we obtain the total systematic error of $\Delta\mu/\mu = 3.7 \times 10^{-6}$. The resulting constraint is then $\Delta\mu/\mu = (17.1 \pm 4.5_{\text{stat}} \pm 3.7_{\text{sys}}) \times 10^{-6}$. Analysis of solar twin and asteroid spectra shows that an additional systematic effect pertaining to wavelength miscalibration over long ranges is found in the quasar spectrum. Due to this miscalibration the $\Delta\mu/\mu$ measurement may have been shifted toward more positive values. Although both the asteroid and solar twin calibrations suggest corrections of the same sign, their magnitudes differ by a factor of two. In making a correction, we rely on the solar twin spectra which are taken closer in time to most of the quasar observations and with the same spectrograph settings. They deliver a $\Delta\mu/\mu$ correction of $(-4.4 \pm 2.0_{\text{sys}}) \times 10^{-6}$ and hence a corrected $\Delta\mu/\mu$ of $(12.7 \pm 4.5_{\text{stat}} \pm 4.2_{\text{sys}}) \times 10^{-6}$.

3.6 Discussion

In the present study ESO archival spectra toward a quasar system B0642–5038 with a DLA at redshift 2.659 are analyzed to extract information on a possible variation of the proton-electron mass ratio μ . The DLA contains a molecular fraction of $\log f = -2.18 \pm 0.08$ in which 111 H₂ lines were identified as usable for a μ -variation analysis. The spectrum is of good quality and has a SNR of ~ 35 in the relevant wavelength region of H₂ absorbers, which is just a bit lower than some other systems that were analyzed previously, e.g., J2123–0050 [62, 63], Q0528–250 [56, 57], Q0405–443 [56], and Q0347–383 [56, 130], and better than Q2348–011 [66] and HE0027–1836 [37].

The resulting value of $\Delta\mu/\mu = (17.1 \pm 4.5_{\text{stat}} \pm 3.7_{\text{sys}}) \times 10^{-6}$ represents a result that is in itself a remarkable 3σ effect on a varying constant. However, we find evidence for a long-range distortion of the wavelength scale in the analyzed spectrum. On the basis of our analysis of asteroid and solar twin spectra and on a similar study by [37] we conclude that because of long-range distortions $\Delta\mu/\mu$ in this spectrum has shifted away from its actual value toward more positive values. Although the sign of this systematic error seems to be consistent among data taken in different epochs, the amplitude appears to be varying. We use solar twin spectra that are taken close in time to the quasar observations to make a correction that reduces the significance of the initial measurement and delivers $\Delta\mu/\mu = (12.7 \pm 4.5_{\text{stat}} \pm 4.2_{\text{sys}}) \times 10^{-6}$ or $(12.7 \pm 6.2) \times 10^{-6}$ if the

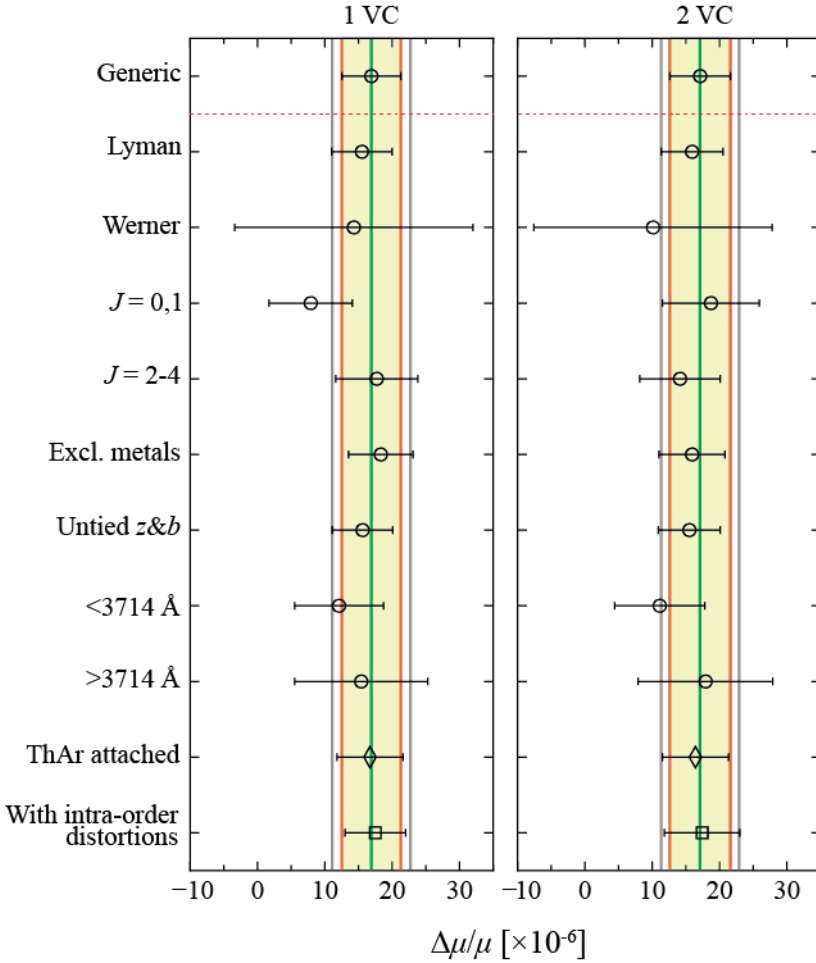


Figure 3.7: Constraints from various tests described in Section 3.4 are displayed for comparison with the one from a generic model that includes all 111 transitions and all available spectral data. The vertical green line in each panel indicates the $\Delta\mu/\mu$ value from the generic test. The shaded area and red (gray) vertical lines indicate the 1σ statistical (statistical and systematic) uncertainties associated with the constraints from the generic tests. The two bottom constraints are used to estimate systematic error on $\Delta\mu/\mu$ due to potential wavelength-scale inaccuracies described in Section 3.5.

uncertainties are added in quadrature.

Regarding the analysis presented here, of great importance is the consistency found in the statistical and systematic tests performed on the data set. These tests, results of which are graphically displayed in Fig. 3.7, constitute VC analysis, the separate effect of subsets of Lyman and Werner bands, separate sets of populated rotational states associated with cold and warm molecular fractions, separation of wavelength regions, and effects of short-range (i.e., intraorder) distortions of the wavelength scale. No significant difference was found between the sets of quasar exposures with attached ThAr calibration spectra and the sets for which the ThAr calibration was performed at the end of the night after resets of the grating in the spectrometer.

The presented $\Delta\mu/\mu$ constraint can be viewed in the perspective of the entire set of results that is currently being produced for H₂ absorptions at high redshift. In Fig. 3.8 this data set is plotted. From all the analyses being performed we have collected those results that were obtained through the comprehensive fitting method. In previous reports an extensive discussion is provided on the advantages of the comprehensive fitting over the line-by-line method [62, 56]. Only for the case where a single VC is definitive, such as in Q0347–383 [130], is a result from a line-by-line analysis included in the overview. Averaging over the presented data set results in $\Delta\mu/\mu = (4.0 \pm 1.8) \times 10^{-6}$ for look-back times in the range of 10–12 billion years.

Naturally, a question arises as to what extent the $\Delta\mu/\mu$ constraints measured in the past are affected by the long-range wavelength miscalibration. In the data set displayed in Fig. 3.8, only the constraints from the B0642–5038 and HE0027–1836 quasar sight lines are derived with the long-range wavelength distortion effect taken into account. According to the present study, wavelength distortions can vary in amplitude within one night as well as over a month's time, while [37] found year-to-year changes. Thus, regarding the H₂ absorbers that have been analyzed so far, a case-by-case reanalysis might be necessary, where this newly found systematic effect is investigated. Although from the presently available information it seems likely that the individual and average $\Delta\mu/\mu$ measurements are biased toward more positive values, the two examples discussed further reinforce the motivation for individual reanalysis using absolute calibration methods such as the supercalibration method. As for VLT/UVES, a detailed and very accurate study was made for the Q0528–250 H₂ absorbing system. On the basis of UVES data recorded in 2003 January reported by [131], [56] performed a reanalysis with the comprehensive fitting method and retrieved a constraint of $\Delta\mu/\mu = (-1.4 \pm 3.9) \times 10^{-6}$. On the basis of an independent data set for Q0528–250, recorded in the period 2008 November to 2009 February, [57] deduced a constraint of $\Delta\mu/\mu = (0.3 \pm 3.7) \times 10^{-6}$, in perfect agreement, while the data sets of the same object analyzed by the same methods were obtained over a time interval of 6 yr. How the long-

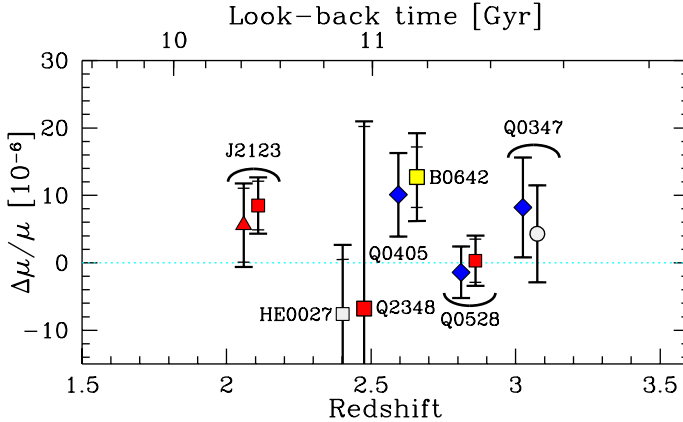


Figure 3.8: $\Delta\mu/\mu$ constraints from H_2 in seven different quasar sightlines: Q0528–250 [56, 57], J2123–0050 [134, 63], Q0347–383 [56, 130], Q2348–011 [66], Q0405–443 [56], HE0027–1836 [37], and B0642–5038 (this work). Note that some absorbers were analyzed more than once; in these cases one of the points is offset on the z scale by +0.05 to avoid overlap. Also the Q2348 point is offset by +0.05 to avoid overlap with HE0027, which is located at a similar redshift. All the constraints shown here are derived by employing the comprehensive fitting method, except for a constraint from Q0347–383, shown as a gray circle [130].

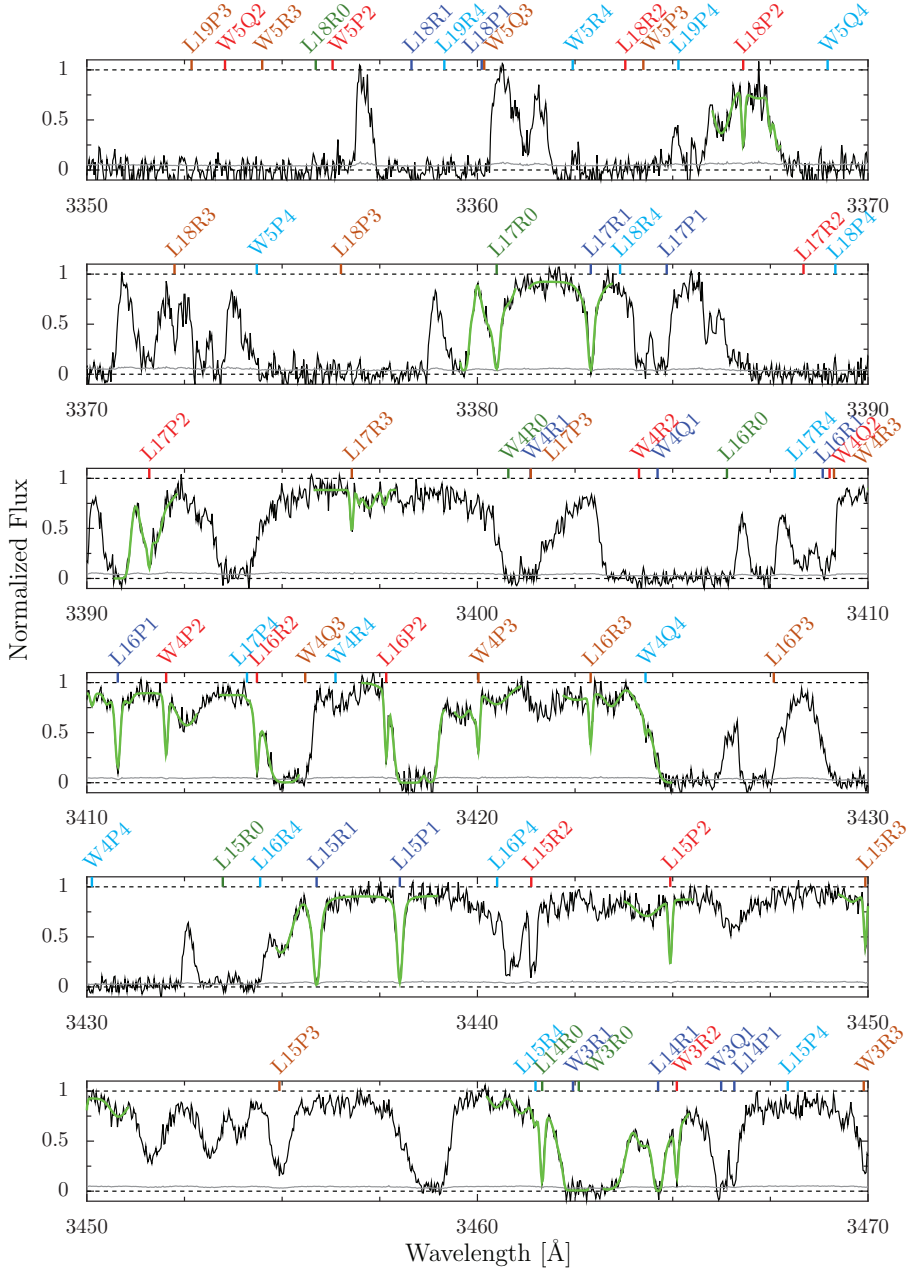
range wavelength distortions change with time is not understood, it remains to be seen whether it is just a coincidence that these two constraints were affected similarly. Further, there is a result on the analysis of H_2 absorption toward J2123–0050, from two different telescopes. While [62] obtained $\Delta\mu/\mu = (5.6 \pm 5.6_{\text{stat}} \pm 2.9_{\text{sys}}) \times 10^{-6}$ from an observation of J2123–0050 with Keck/HIRES, [63] obtained $\Delta\mu/\mu = (8.5 \pm 3.6_{\text{stat}} \pm 2.2_{\text{sys}}) \times 10^{-6}$ from VLT/UVES, also in good agreement. Here it is noted that the same comprehensive fitting method was used in both analyses, and that, so far J2123–0050 is the best H_2 absorbing system analyzed, in terms of brightness of the background quasar and the column density of the H_2 absorbing galaxy. This particular absorber was investigated in a recent study by [145], in which direct comparison of the HIRES/Keck and VLT/UVES spectra was made to detect possible relative velocity shifts between the two. Although some indications of a constant offset between the spectra were found, no significant wavelength-dependent shift could be detected. The sensitivity of the direct comparison method is similar to that of the supercalibration approach used in the current study (a few $\text{m s}^{-1} \text{ nm}^{-1}$). Thus, the results by [145] might be held as coun-

terevidence against long-range distortions of the UVES wavelength calibration, unless HIRES/Keck suffers from a similar problem. More investigations of this phenomenon are urgently needed, in particular for studies such as the present one that require understanding of the calibration of the spectrometer at its extreme limits. This would lead to establishing a firm constraint on a variation of μ at redshifts $z \sim 2-3$.

Studies at lower redshifts, based on the ammonia and methanol methods, yield a constraint of μ varying at the level of less than 3×10^{-7} [96, 132, 20, 21]. These strongly constraining findings, produced from absorbing clouds toward PKS1830–211 and B0218+357, may be interpreted as contradictory to less constraining results beyond $z > 2$. In view of physical models linking coupling strengths to the ratio of matter versus dark energy in the universe, where variation of constants is frozen by dark energy [17, 146], it remains important to search for drifting constants in various evolutionary stages of the universe, i.e., at different redshifts.

Appendix

The B0642–5038 spectrum and the fitted regions are displayed in Fig. 3.9 to 3.14. The tick marks for the H₂ transitions are positioned at $z = 2.658603$. Different J transitions are labeled in different colors. The photons at the bluest wavelengths ($< 3355 \text{ \AA}$) are cut out by the Lyman limit of the DLA.

Figure 3.9: Part 1 of 6 of the B0642–5038 spectrum with fitted H₂ transitions.

3. ANALYSIS OF H₂ ABSORPTION TOWARD QSO B0642–5038

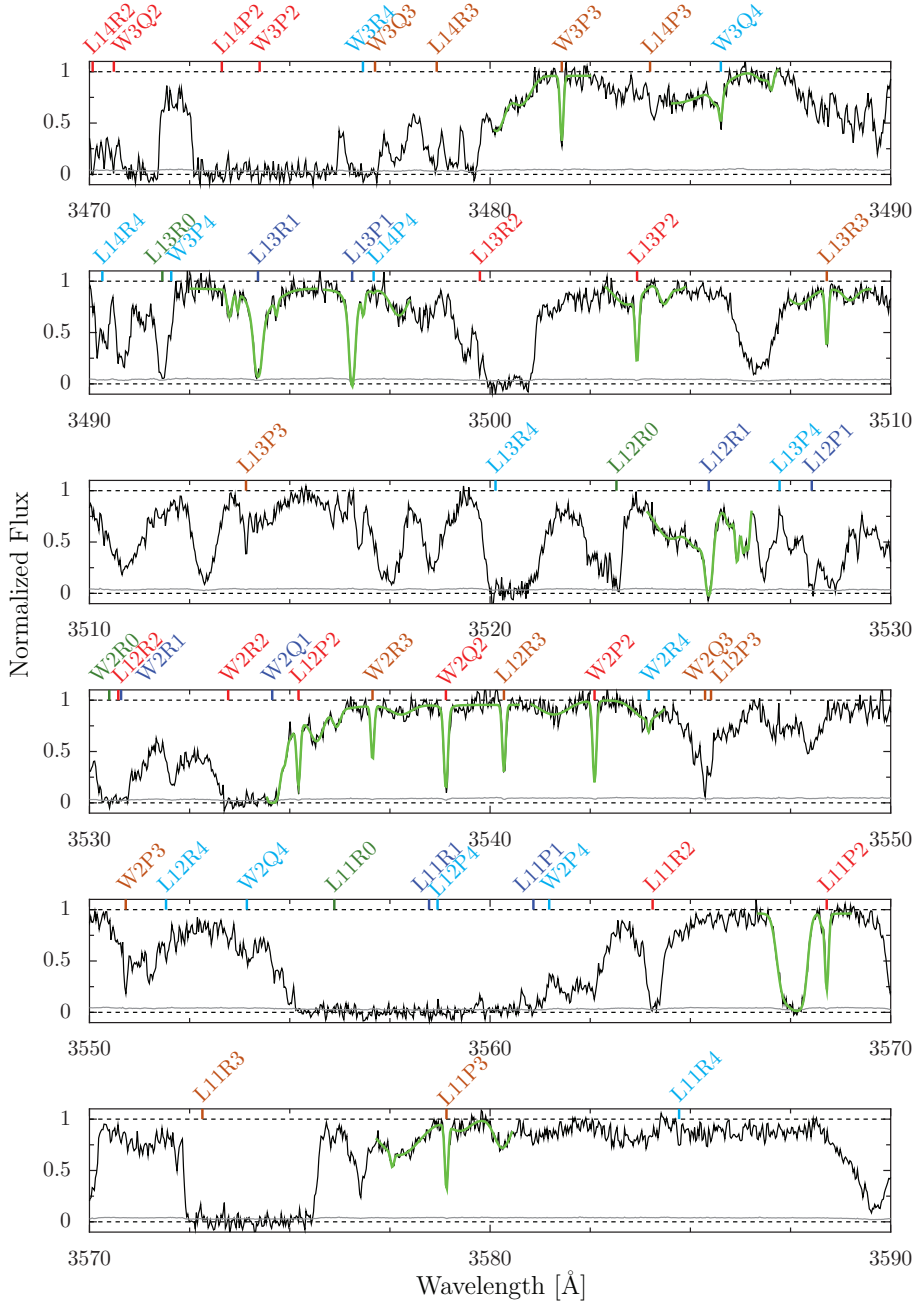
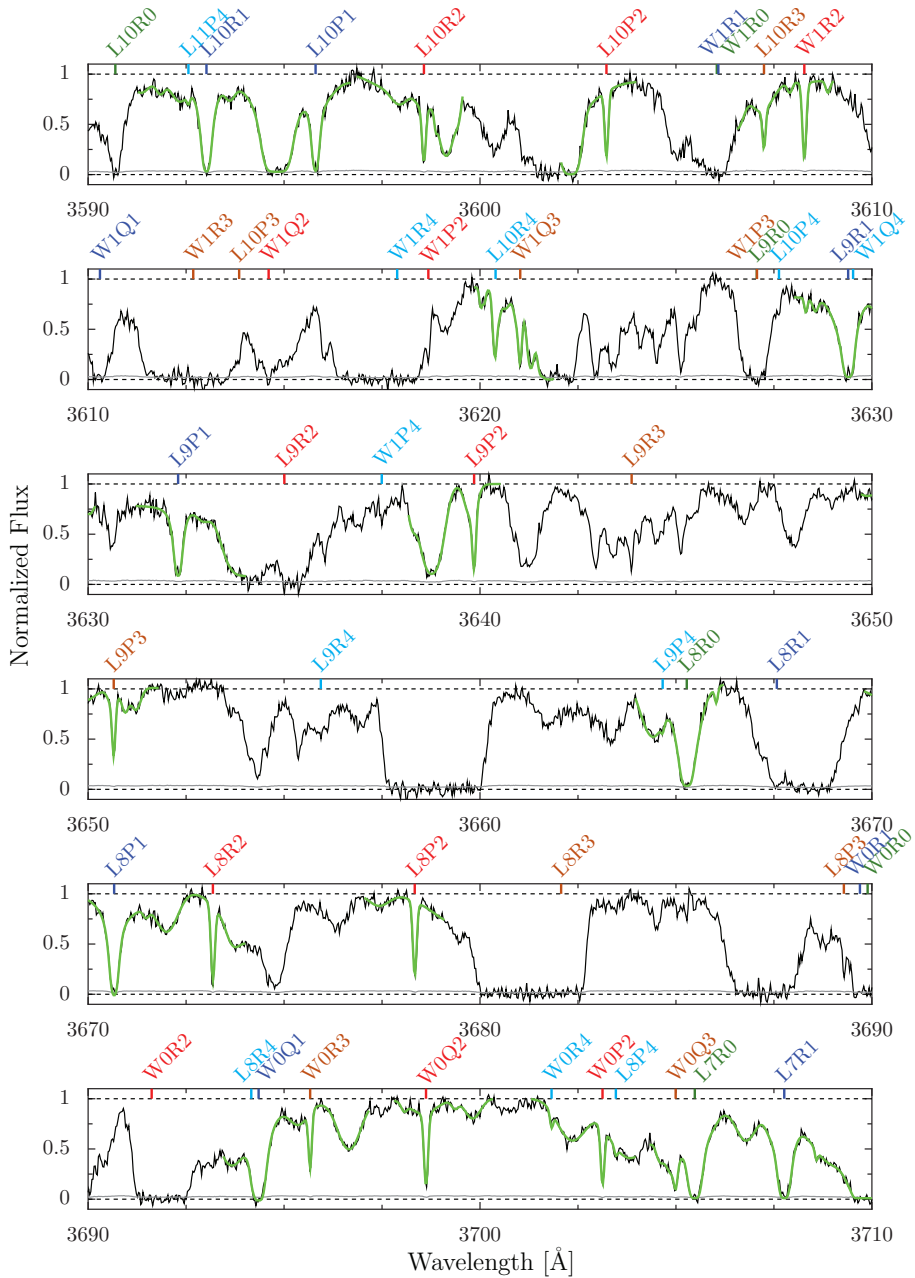


Figure 3.10: Part 2 of 6 of the B0642–5038 spectrum with fitted H₂ transitions.

Figure 3.11: Part 3 of 6 of the B0642–5038 spectrum with fitted H_2 transitions.

3. ANALYSIS OF H₂ ABSORPTION TOWARD QSO B0642–5038

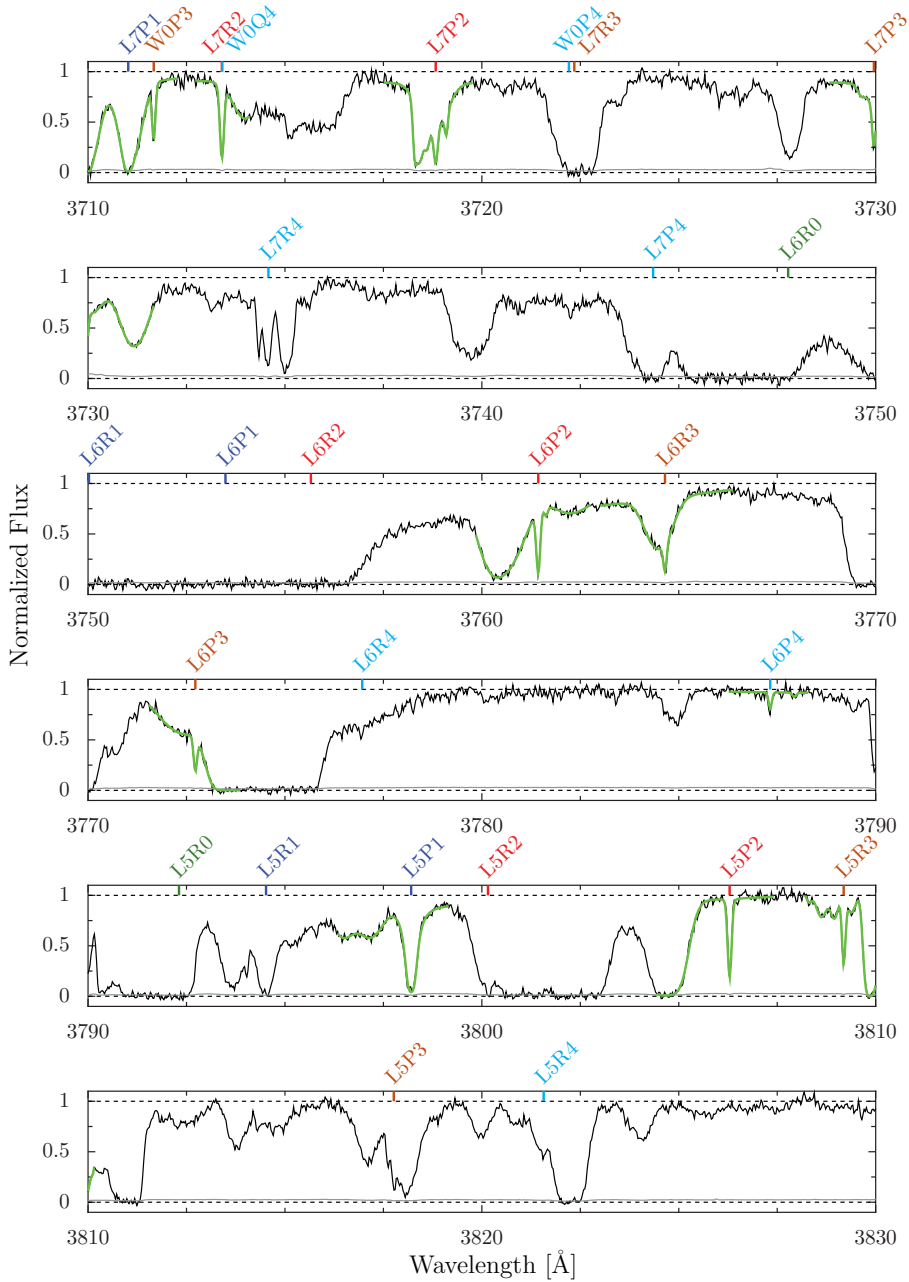
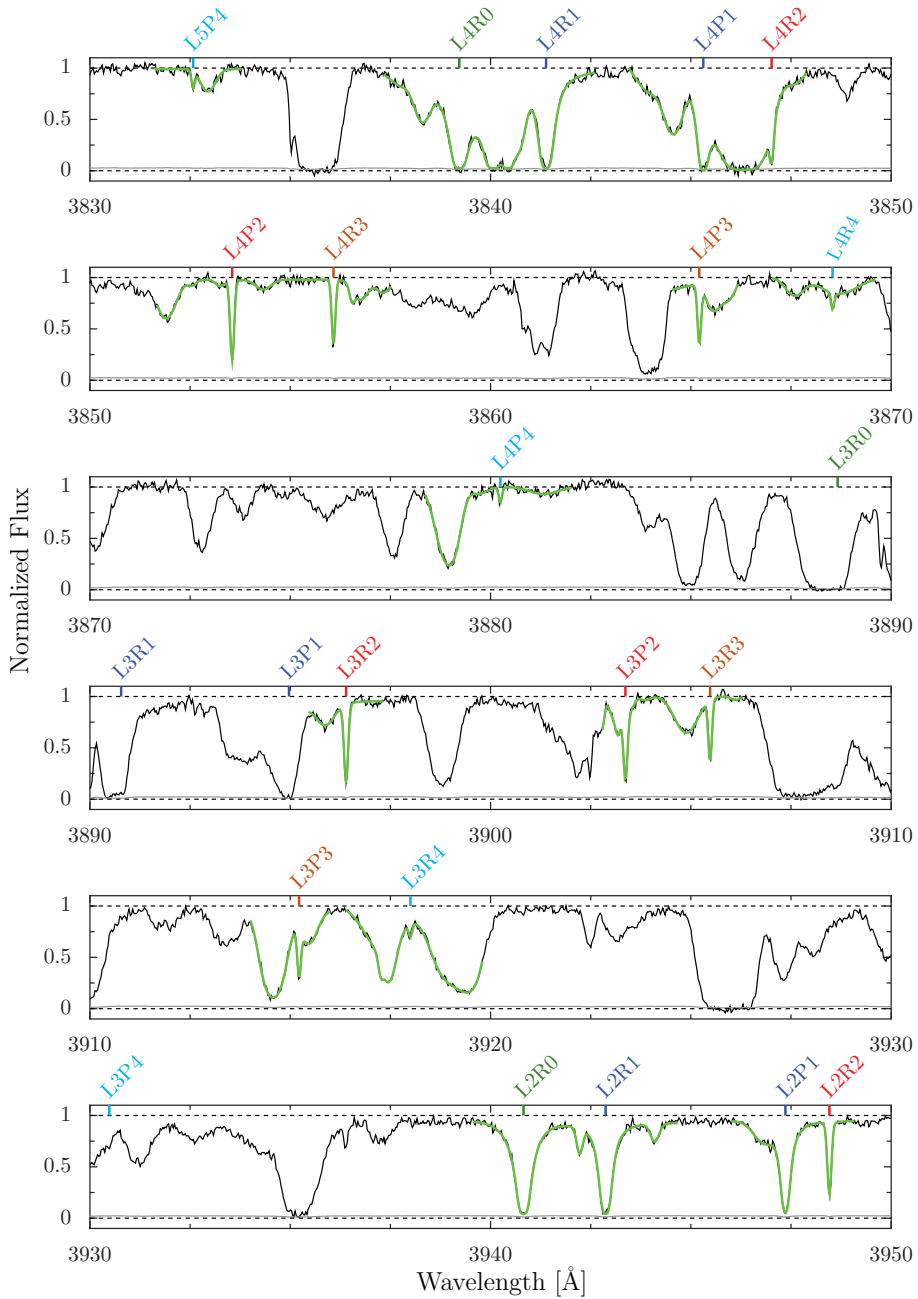


Figure 3.12: Part 4 of 6 of the B0642–5038 spectrum with fitted H₂ transitions.

Figure 3.13: Part 5 of 6 of the B0642–5038 spectrum with fitted H₂ transitions.

3. ANALYSIS OF H₂ ABSORPTION TOWARD QSO B0642–5038

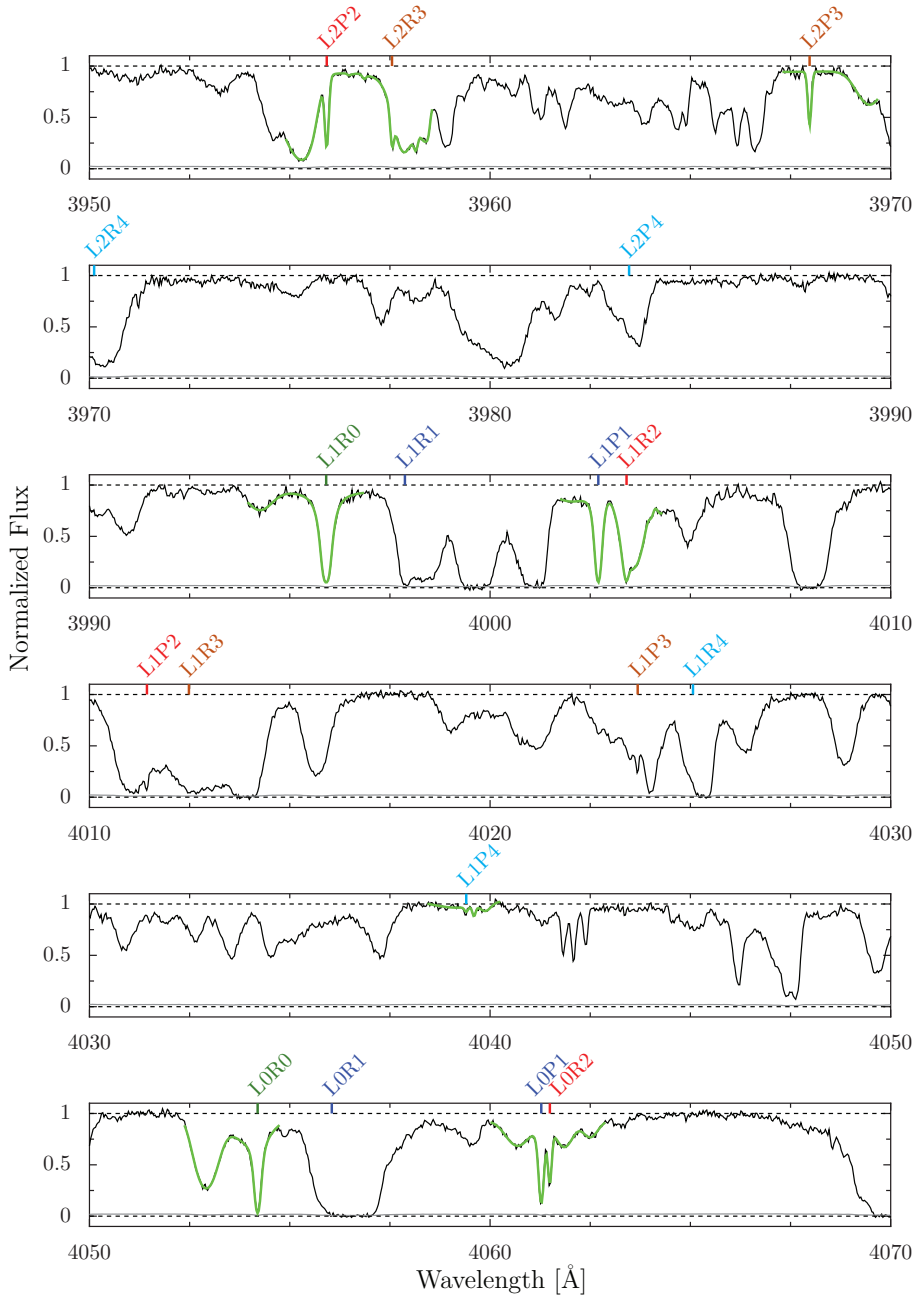


Figure 3.14: Part 6 of 6 of the B0642–5038 spectrum with fitted H₂ transitions.

Constraint on a varying proton–electron mass ratio 1.5 billion years after the Big Bang

*Bagdonaite, J., Ubachs, W., Murphy, M. T. & Whitmore, J. B.
Accepted for publication in Phys. Rev. Lett. (2015).*

Abstract

A molecular hydrogen absorber at a lookback time of 12.4 billion years, corresponding to 10% of the age of the universe today, is analyzed to put a constraint on a varying proton–electron mass ratio, μ . A high resolution spectrum of the J1443+2724 quasar, which was observed with the Very Large Telescope, is used to create an accurate model of 89 Lyman and Werner band transitions whose relative frequencies are sensitive to μ , yielding a limit on the relative deviation from the current laboratory value of $\Delta\mu/\mu = (-9.5 \pm 5.4_{\text{stat}} \pm 5.3_{\text{sys}}) \times 10^{-6}$.

The accelerated expansion of the universe is ascribed to an elusive form of gravitational repulsive action referred to as dark energy [147, 148, 149]. Whether it is a cosmological constant, inherent to the fabric of space-time, or whether it may be ascribed to some dynamical action in the form of a scalar field ϕ [150], is an open issue. In the latter case it has been shown that the interaction of the postulated quintessence fields ϕ to matter cannot be ignored, giving rise to a variation of the fundamental coupling constants and a breakdown of the equivalence principle [151, 129]. In this context it is particularly interesting to probe possible variations of the fundamental constants in the cosmological epoch of the phase transition, going from a matter-dominated universe to a dark energy-dominated universe, covering redshift ranges $z = 0.5 - 5$ [17]. While models of Big Bang nuclear synthesis probe fundamental constants at extremely high redshifts ($z = 10^8$) [92], the Oklo phenomenon ($z = 0.14$) [152] and laboratory atomic clock experiments ($z = 0$) [29] probe low redshifts. Absorbing galaxies in the line-of-sight of quasars are particularly suitable for investigating the range of medium-high redshifts, for a varying fine-structure constant, α , based on metal absorption [34] and for a varying proton-electron mass ratio, $\mu = m_p/m_e$, based on molecular absorption [153]. Furthermore, unification scenarios predict that variations of α and μ are connected, while in most schemes μ is a more sensitive target for varying constants [9].

A variation of μ may be probed through the spectroscopy of molecules such as hydrogen (H_2) [44], ammonia (NH_3) [96] and methanol (CH_3OH) [20]. The latter polyatomic molecules are more sensitive to a variation in μ under the assumption that molecular reduced masses, involving protons and neutrons, scale in a similar manner as μ , which can be probed in a pure form in H_2 [153]. Moreover, the radio absorption systems, where the polyatomic absorbers can be found, are more rare and are currently only found at the lower redshifts $z = 0.68$ [95, 132] and $z = 0.89$ [20]. Molecular lines observed at $z = 6.34$ [154] are of insufficient spectral quality to constrain μ -variation. Conveniently, the ultraviolet spectrum of the H_2 Lyman and Werner bands can be investigated with large ground-based optical telescopes for absorbers at redshifts $z > 2$. The current sample of H_2 -based measurements covers a redshift interval from 2 to 3 [63, 37], with the highest redshift object Q0347-383 at $z = 3.025$ [56, 130].

Here we constrain variations in μ at substantially higher redshift by analyzing an H_2 absorber at $z = 4.22$ along the sightline towards the background ($z = 4.42$) quasar PSS J1443+2724 [64]. This step to higher redshift is challenging for several reasons. Firstly, more distant quasars are typically fainter, making initial discovery of the H_2 absorption more difficult and requiring longer integration times for a high-quality spectrum with which to constrain $\Delta\mu/\mu$. Secondly, absorption lines from neutral hydrogen (HI) in the intergalactic medium are more numerous at higher redshifts, complicating analysis of the H_2 transitions. The Lyman-series transitions from the many

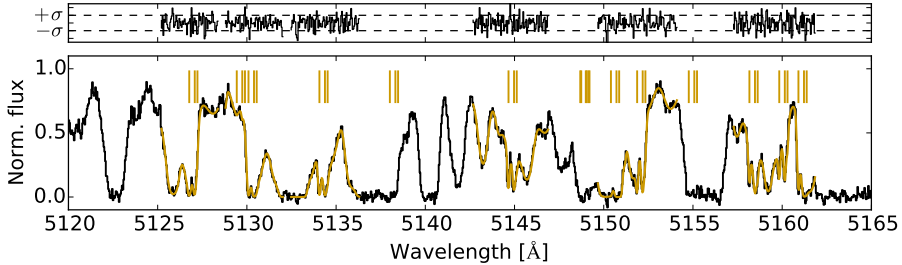


Figure 4.1: Part of the final, fitted spectrum of J1443+2724. The sticks indicate the 3 velocity components of each H_2 transition from the rotational levels $J = (0 - 4)$. The residuals are shown above the spectrum for the regions fitted. The broad features that surround and overlap the fitted H_2 transitions are multiple, unrelated H I Lyman-series absorption lines arising in other absorbers along the line of sight.

unrelated H I clouds in the intergalactic medium form a characteristic ‘forest’ of broader spectral features against which the H_2 have to be identified and analyzed (see Fig. 4.1). However, the ‘comprehensive fitting’ method of simultaneously treating this H I forest and the H_2 absorption, developed previously and documented extensively [56, 62, 63, 59], is employed here to reliably meet this challenge.

A portion of the J1443+2724 spectrum is shown in Fig. 4.1. To create the spectrum, we make use of an archival dataset obtained in 2004 [64] and a new dataset obtained in 2013 (Program ID 090.A-0304) which comprise, respectively, 7.3 and 16.7 hours (5 and 12 exposures) observation time with the Very Large Telescope/the Ultraviolet and Visual Echelle Spectrograph (VLT/UVES). For weak light sources as the present quasar (visual magnitude $V \sim 19.4$) long integration time is required to reach signal-to-noise ratio (SNR) of >30 , especially if high spectral resolution is required. Wavelength calibration in the UVES instrument is achieved by observing a reference ThAr lamp. After each night of observations (in 2004) or, preferably, immediately after each quasar exposure (in 2013) a spectrum of the ThAr lamp was recorded using identical settings to those of the science exposure. The ThAr spectrum was used by the UVES data-reduction pipeline to create pixel-vs.-wavelength maps and apply them to the quasar exposures. The wavelength scales of the spectra were converted to vacuum-heliocentric values. Following the same procedures as in [62, 63, 59], flux-extracted individual exposures were then resampled, scaled and merged to a final 1D spectrum that extends from 474 to 792 nm, with the H_2 transitions detected at 484–581 nm. The SNR at shorter wave-

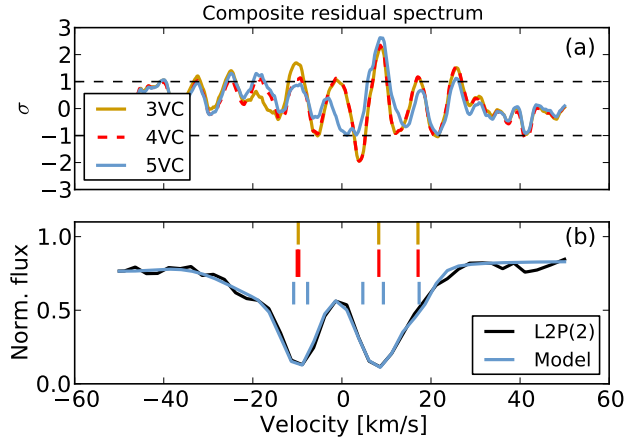


Figure 4.2: (a) Composite residual spectra of 31 transitions shown for the 3, 4, and 5 VC models. (b) An H_2 absorption profile in the J1443+2724 spectrum. The sticks indicate the positions of velocity components for the 3, 4, and 5 VC models.

Table 4.1: Results of fitting models of increasing complexity to the spectrum. The two velocity features (see Fig. 4.2) require fitting at least 2 velocity components (VC) but as it can be seen from the goodness-of-fit measure χ_ν^2 (where ν is the number of degrees of freedom; here $\nu \sim 4600$) models with 3, 4, and 5 VC replicate the data better. For each model, a resulting $\Delta\mu/\mu$ value is shown in the last column.

Number of VCs	χ_ν^2	$\Delta\mu/\mu [\times 10^{-6}]$
2	1.396	-8.7 ± 5.2
3	1.161	-6.7 ± 5.4
4	1.139	-8.3 ± 5.4
5	1.133	-2.9 ± 5.2

lengths is entirely dominated by the data from 2004 as the observations in 2013 were affected by stray light from the full moon.

As shown in Fig. 4.2, each H_2 transition in the J1443+2724 spectrum has two distinct velocity features. In the comprehensive fitting method employed here, these two features in all H_2 transitions are fitted simultaneously (along with the many broader, unrelated HI forest features). With this approach, one makes use of the known molecular physics of H_2 , thereby reducing the number of free parameters in the fit. In particular, transitions from the same

ground rotational level J are fitted using a single parameter for column density, N_J , while, for the same velocity component (VC), transitions from all J levels are tied in terms of redshift, z , and line-width, b . The intrinsic intensities of the H_2 absorbing transitions are fixed to the oscillator strengths known from the molecular physics database [62]. In this way, the best fit is achieved by simultaneously combining information from multiple spectral regions. In the case of J1443+2724, we selected 60 spectral regions containing a total of 89 H_2 transitions up to $J = 4$, among which 17 are from the Werner band¹. This approach, along with the simultaneous fitting of the HI forest lines, is the same as detailed previously (e.g. [63, 59]). The χ^2 minimization is performed using a Voigt profile fitting program VPFIT9.5.² To fit each transition i , a Voigt profile is created from a threefold convolution of a Lorentzian profile defined via a damping parameter Γ_i , a Gaussian profile describing the thermal and turbulent velocities in the gas, and an instrumental profile. For the i th transition of H_2 detected at redshift z_{abs} , the recorded wavelength is expressed as:

$$\lambda_i = \lambda_i^0(1 + z_{abs})(1 + K_i \frac{\Delta\mu}{\mu}), \quad (4.1)$$

where λ_i^0 is the corresponding laboratory wavelength, and K_i is a coefficient that quantifies the sign and magnitude of its sensitivity to a varying μ [44], and where that variation is parametrized by $\Delta\mu/\mu = (\mu_z - \mu_{lab})/\mu_{lab}$.

The two velocity features per transition can contribute towards better precision of $\Delta\mu/\mu$. However, previous studies have shown that an inadequate fit of H_2 features can produce a spurious $\Delta\mu/\mu$ value [127]. In particular, under-fitted velocity profiles are more prone to such errors. To avoid that, additional VCs are included in the profile to check for a more complex velocity structure than can be appreciated by eye. The additional components can be rejected by VPFIT as statistically unjustified or they can remain and improve the model. Table 4.1 contains the results of fitting increasingly complex models to the H_2 spectrum of J1443+2724. Fig. 4.2 displays composite residual spectra of different models. The composite residual spectra are created by combining a number of residuals of individual transitions, which are aligned in velocity/redshift space [62]. While according to the reduced χ^2 value, a model with 4 or 5 VCs initially might appear preferable to one with only 3 VCs, fitting the former more complex models was not stable: VPFIT rejected the additional VCs in lower- J transitions while retaining them in higher- J transitions, thereby departing from a physically plausible, self-consistent model. Fig. 4.2 shows that adding a second VC to the left feature of the absorption profile

¹See Appendix for the complete list of fitted transitions, the final fitted spectrum, and details on continuum fitting.

²Developed by R. F. Carswell et al.; available at <http://www.ast.cam.ac.uk/~rfc/vpfit.html>

Table 4.2: Results of fitting a 3 VC model to the data.

z_{abs}	b [km/s]	$\log(N/\text{cm}^{-2}) \pm \sigma_{\log N}$ from $J = 0$ to $J = 4$
4.2237292(6)	1.74 ± 0.06	$17.04 \pm 0.06, 17.40 \pm 0.05, 15.86 \pm 0.09,$ $14.81 \pm 0.04, 12.99 \pm 0.84$
4.2240440(11)	0.42 ± 0.18	$17.49 \pm 0.03, 17.87 \pm 0.02, 17.34 \pm 0.02,$ $17.09 \pm 0.03, 13.80 \pm 0.33$
4.2241975(20)	0.20 ± 0.08	$15.01 \pm 0.33, 16.17 \pm 0.10, 15.77 \pm 0.09,$ $15.97 \pm 0.06, 13.67 \pm 0.61$

reduces the composite residuals, but that the residuals for the right feature are barely affected when adding a third VC.

In all the models, the H_2 absorption feature on the right requires fitting of at least one very narrow component. This weak component exhibits an unusually high relative column density for $J = 2, 3$ levels, and a width of 0.2 km/s, corresponding to a kinetic temperature of 5 K, hence lower than $T_{\text{CMB}} = 14$ K at $z = 4.22$. While this low b value results from a best-fit model and hence is favored statistically, we performed further testing by imposing b_{min} parameters corresponding to temperatures including those in the expected kinetic regime of 50–100 K ($b \sim 0.6 - 0.9$ km/s). These tests, performed for 3 VC and 4 VC models demonstrate that resulting values for $\Delta\mu/\mu$ do not critically depend on the narrowness of this velocity feature.³ A spectrum of a higher SNR and higher resolution might help in explaining the composite residual excess and the N, b values obtained here.

Based on the internal consistency of various fitting results, a model with 3 VCs is selected as the fiducial model (see Table 4.2 for fitting results) and is further tested for possible systematics. The 4 and 5 VC fits are used to verify the results of the fiducial model.

The fiducial 3 VC model delivers $\Delta\mu/\mu = (-6.7 \pm 5.4_{\text{stat}}) \times 10^{-6}$. Fig. 4.3 shows how this result compares to constraints obtained from fitting only certain selected transitions, velocity components, or parts of the spectrum. Most of the derived constraints are compatible with the fiducial result, demonstrating that the result is robust. Nevertheless, a possible discrepancy is that constraints from the low- and high- J transitions seem to move in opposite directions if fitted separately. This tendency is observed in the 4 and 5 VC models as well. If the redshift and width parameters are tied separately for the low- J and high- J transitions the resulting z and b parameter values agree well between the two groups. Fitting only the small number of Werner transitions (17), together

³See Appendix for the specific test results.

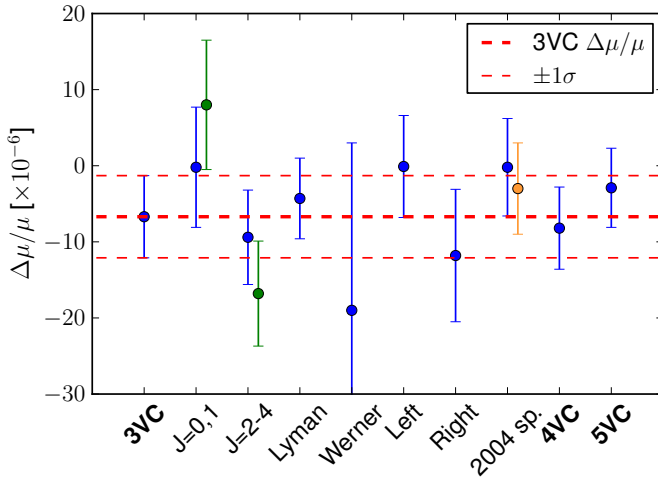


Figure 4.3: $\Delta\mu/\mu$ constraints obtained from the fiducial 3VC model, from various tests performed on it, and from the 4VC and 5VC models. The green points refer to fitting low- and high- J transitions with the z and b parameters tied within each group but not between the two groups. The left and the right tests refer to deriving $\Delta\mu/\mu$ constraints from the two velocity features of H_2 separately (see Fig. 4.2). The orange point was obtained after the spectrum obtained in 2004 has been corrected for long-range wavelength distortions.

with their smaller spread in K_i coefficients, results in a large uncertainty in $\Delta\mu/\mu$. Fitting a spectrum that includes only the exposures from 2004 delivers $\Delta\mu/\mu = (-0.2 \pm 6.4_{\text{stat}}) \times 10^{-6}$. This constraint, as well as the constraints derived from the 4 and 5 VC models on a full spectrum, are in agreement with the result from the fiducial model. Fitting a spectrum that includes only 2013 exposures results in $\Delta\mu/\mu = (4.0 \pm 12.4_{\text{stat}}) \times 10^{-6}$. The uncertainty is much larger because the SNR of the data collected in 2013 is affected by additional noise from the full moon.

The accuracy to which $\Delta\mu/\mu$ can be measured strongly relies on accurate wavelength calibration of the quasar spectrum. At any wavelength in the J1443+2724 spectrum, the error of the wavelength calibration solution is ~ 70 m/s which translates to $\Delta\mu/\mu$ of 1×10^{-6} given a spread in K_i coefficients of 0.05.⁴

⁴Calculated via $\Delta\mu/\mu = 1/\Delta K_i \times \Delta v/c \times 1/\sqrt{n}$, where n is the number of ThAr transitions per one echelle order; typically $n > 15$.

An additional source of systematic uncertainty might be caused by wavelength-scale distortions inherent to the instrument. Short-range distortions with a characteristic shape repeating in each diffraction order of the echelle spectrograph were found in UVES [128]. We estimate its potential to systematically shift $\Delta\mu/\mu$ value by applying a saw-tooth like distortion of ± 100 m/s to each order and fitting the recombined spectrum, as in [62, 59]. This results in a $\Delta\mu/\mu$ shift as small as 1×10^{-7} .

Recently, indications were reported that the UVES instrument is also susceptible to long-range wavelength distortions that are able to mimic non-zero $\Delta\mu/\mu$ values at the level of several parts per million [37]. Their origin is not clear but deviations between the light paths of the quasar and ThAr lamp is considered the likely (proximate) cause. The effect of such a miscalibration can be quantified by observing objects that have well-understood spectra, such as asteroids which reflect the solar spectrum and stars with solar-like spectra, known as solar twins [155, 37, 38, 59]. In the archive of UVES,⁵ we found several Sun-like stars that were observed in 2004, at a similar time as the J1443+2724 quasar.⁶ By comparing their spectra to a highly accurate Fourier-Transform spectrum of the Sun⁷ we found a correction amounting to 44.9 ± 46.8 m/s/1000 Å. An extensive study of this particular systematic effect shows that corrections of this size are typical for the considered time period [38]. Applying the aforementioned correction on the wavelength scale of the spectrum obtained in 2004 results in a $\Delta\mu/\mu$ shift of -2.8×10^{-6} if compared to the uncorrected constraint. The uncertainty on this correction translates into a systematic $\Delta\mu/\mu$ uncertainty of 1.6×10^{-6} . We consider this shift a representative correction for the long-range wavelength distortions of the total spectrum since 84% of the fiducial $\Delta\mu/\mu$ accuracy is gained from the 2004 exposures.

Creating a 1D spectrum from multiple exposures and overlapping echelle orders involves redispersion onto a single wavelength grid. The rebinning causes correlation in flux and flux uncertainty values between adjacent pixels. Varying the dispersion bin size from the default value of 2.5 km/s by ± 0.1 km/s results in an average $\Delta\mu/\mu$ shift of $\pm 4 \times 10^{-6}$.

The spectra were obtained using 1''0 and 0''8 slitwidths in 2004 and 2013, respectively. This corresponds to respective spectral resolutions of $R \sim 38\,700$ and $\sim 48\,500$ or Gaussian instrumental profiles with the width of $\sigma_{\text{inst}} = 3.3$ and 2.6 km/s. However, the profile to be convolved with the fitted line profile will be up to $\sim 10\%$ narrower because the quasar light is concentrated towards the centre of the slit. The fiducial $\Delta\mu/\mu$ constraint was derived from the

⁵http://archive.eso.org/eso/eso_archive_main.html

⁶See Appendix for the observational details.

⁷<http://kurucz.harvard.edu/sun/irradiance2005/irradthu.dat>

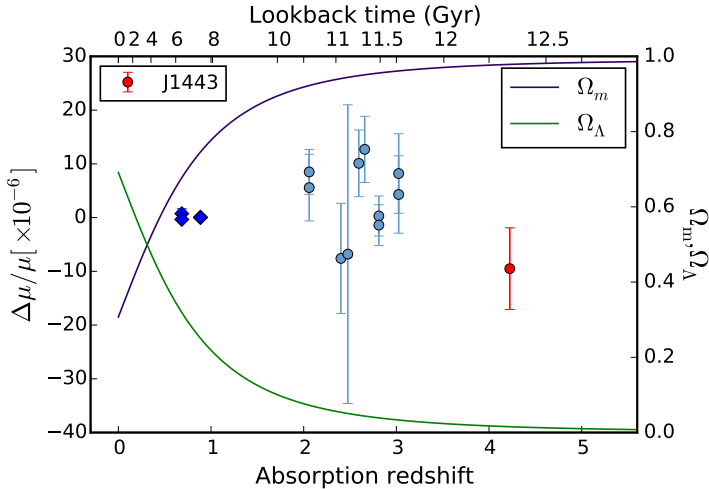


Figure 4.4: The non-relativistic mass density parameter Ω_m and the dark energy density parameter Ω_Λ as functions of redshift, with a corresponding lookback time axis on top. Results from various $\Delta\mu/\mu$ studies: the diamond markers refer to the measurements of rotational transitions of methanol and ammonia [95, 96, 132, 20], while $\Delta\mu/\mu$ values derived from H_2 observations are denoted by circles [56, 62, 66, 63, 57, 130, 37, 59].

combined 2004 and 2013 spectra using an instrumental profile of $\sigma_{\text{inst}} = 2.6$ km/s. Varying the σ_{inst} in the range from 2.6 to 2.9 km/s resulted in deviations from the fiducial $\Delta\mu/\mu$ constraint as large as 3×10^{-6} .

In summary, the constraint on $\Delta\mu/\mu$ derived from this quasar spectrum shows sensitivity to these systematic effects. All the contributions combined (added in quadrature) constitute the total systematic error budget of $\sigma_{\text{sys}} = 5.3 \times 10^{-6}$. After correction for the long-range wavelength distortions, our fiducial constraint therefore becomes $\Delta\mu/\mu = (-9.5 \pm 5.4_{\text{stat}} \pm 5.3_{\text{sys}}) \times 10^{-6}$.

This result constrains a possible variation of the proton–electron mass ratio by means of the H_2 spectroscopic method for the highest redshift so far. Fig. 4.4 displays a comparison with previous data, mainly showing results derived from H_2 absorbers toward quasars in the redshift interval $z = 2 - 3$, as well as the more constraining results from radio astronomy of polyatomic molecules for $z < 0.9$. With the analysis of the absorber toward J1443+2724 the window $z > 4$ is opened. A further comparison can be made with a result from radio astronomy of a lensed galaxy probing a (7-6) rotational transition in CO and a fine-structure transition in atomic carbon ($^3\text{P}_2 - ^3\text{P}_1$) at $z = 5.2$ corresponding

to 12.7 Gyr lookback time;⁸ that study probes the combination of dimensionless constants $F = \alpha^2/\mu$ and yields $\Delta F/F < 2 \times 10^{-5}$ [156].

The presented H_2 constraint signifies a null result. It will assist in setting boundaries to various theories describing physics beyond the Standard Model [129, 17], as well as on the Λ CDM standard model of cosmology [157]. The densities of matter (including dark matter) Ω_m and dark energy Ω_Λ , and their ratio (see Fig. 4.4) are important parameters in the models [151], and the present work covers a wide set of values: in the interval $z = 0-4.22$ dark energy covers $\Omega_\Lambda = 0.68$ to 0.015. While a number of cosmological scenarios suggest varying constants [17, 9] no quantification of the rate of change is predicted, except for some model-dependent scenarios involving screening and not holding for cosmological time scales [158]. Thus, while a clear threshold for new physics is lacking, the observational and experimental targets are positioned to set ever tighter constraints on varying constants. The present study pushes a tight constraint on a varying μ to lookback times of 10% of the age of the universe today.

Acknowledgments

The authors thank the Netherlands Foundation for Fundamental Research of Matter (FOM) for financial support. M.T.M. and J.B.W. thank the Australian Research Council for Discovery Project grant DP110100866 which supported this work. The work is based on observations with the ESO Very Large Telescope at Paranal (Chile).

⁸To compute lookback times we adopt the following values of cosmological parameters: Hubble constant $H_0 = 67.3$ km/s/Mpc, $\Omega_{m,0} = 0.307$, $\Omega_{\Lambda,0} = 0.691$.

Appendix

Fitted transitions

In Table 4.3, the 89 fitted H₂ transitions are listed, grouped by the ground J level. Of these transitions, 17 are from the Werner band. The fitted regions are displayed in Fig. 4.5 to 4.8.

Table 4.3: Eighty-nine fitted H₂ transitions in 60 regions of the J1443+2724 spectrum.

J level	Number of tr.	Transition names
0	7	W3R(0), L14R(0), L10R(0), L8R(0), L7R(0), L1R(0), L0R(0)
1	20	L16P(1), L15P(1), L15R(1), W3R(1), L12R(1), L12P(1), W2Q(1), L10R(1), L10P(1), L9R(1), L9P(1), L8P(1), L4R(1), L4P(1), L3R(1), L3P(1), L2R(1), L2P(1), L1R(1), L1P(1)
2	27	L16R(2), L15R(2), L13R(2), L12P(2), W2R(2), W2Q(2), W2P(2), L11R(2), L11P(2), L10P(2), W1R(2), W1Q(2), L9R(2), L9P(2), L8R(2), W0Q(2), L7R(2), L6P(2), L5P(2), L4R(2), L4P(2), L3P(2), L2R(2), L2P(2), L1R(2), L1P(2), L0P(2)
3	26	L15R(3), W3P(3), L13R(3), L13P(3), L12R(3), W2R(3), L12P(3), W2Q(3), W2P(3), L11P(3), L10R(3), L10P(3), W1R(3), L9R(3), W0R(3), W0Q(3), L6R(3), L5P(3), L4R(3), L4P(3), L3R(3), L3P(3), L2R(3), L1R(3), L0R(3)
4	9	L17P(4), L16P(4), L15R(4), L13P(4), L12R(4), L11P(4), W1Q(4), L9P(4), W0Q(4)

4. A $\Delta\mu/\mu$ CONSTRAINT 1.5 BILLION YEARS AFTER THE BIG BANG

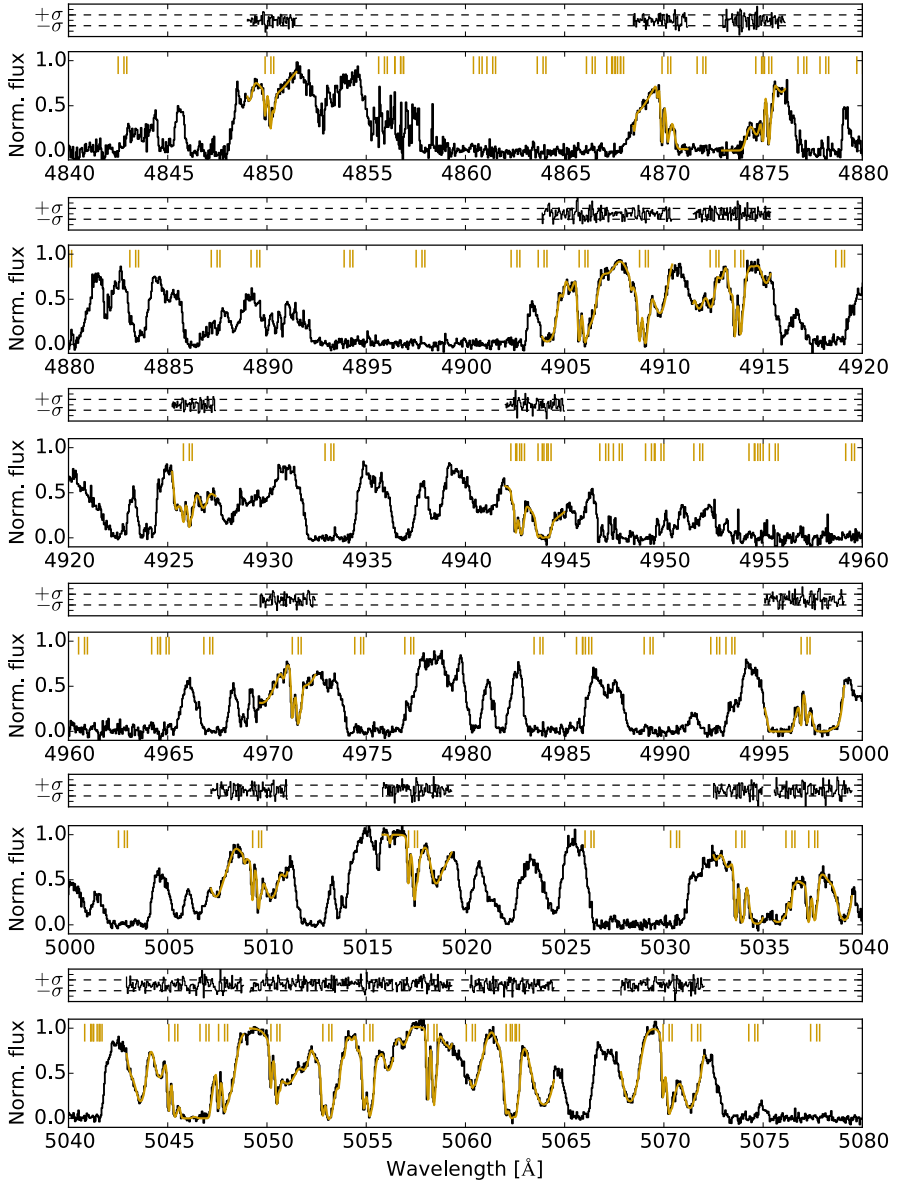


Figure 4.5: Part 1 of 4 of the J1443+2724 spectrum with fitted H₂ transitions.

4. A $\Delta\mu/\mu$ CONSTRAINT 1.5 BILLION YEARS AFTER THE BIG BANG

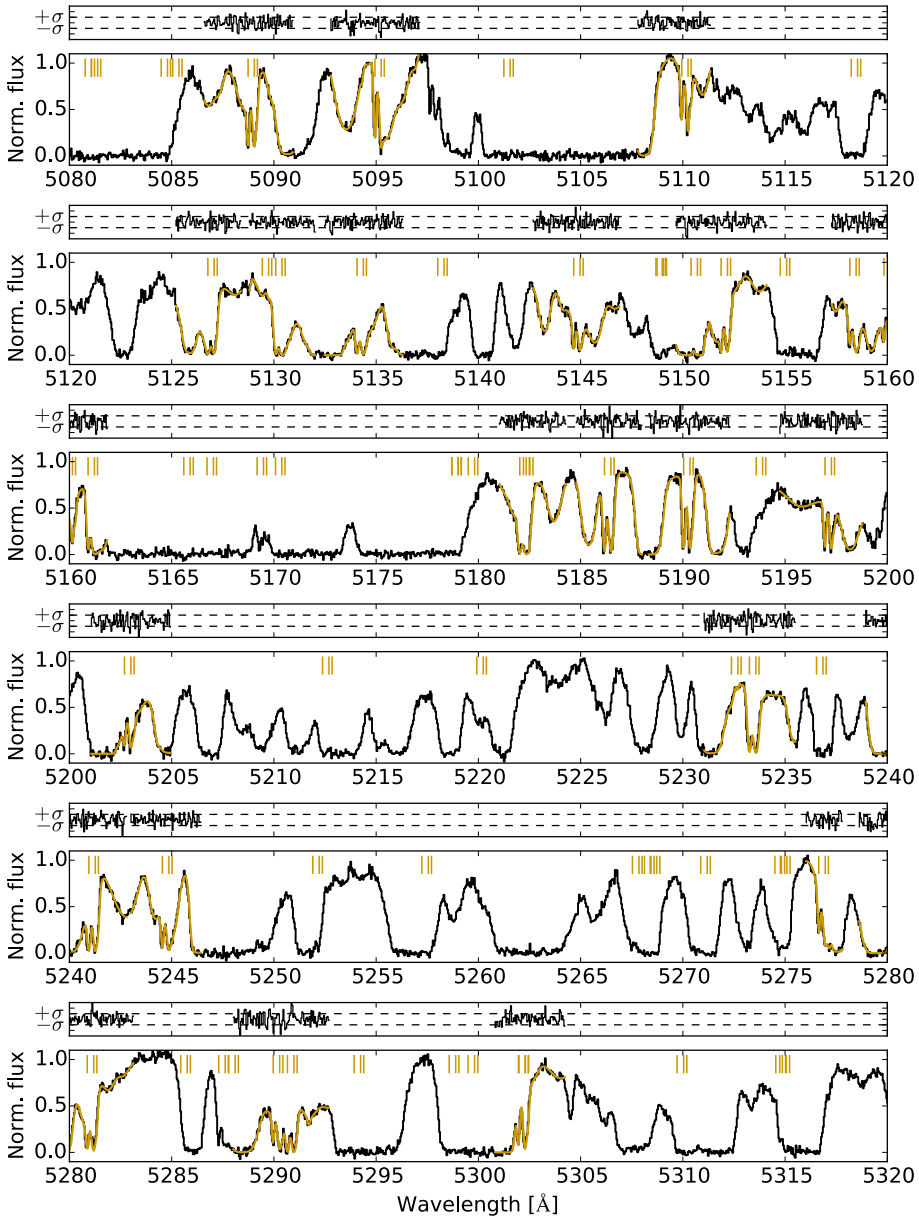


Figure 4.6: Part 2 of 4 of the J1443+2724 spectrum with fitted H₂ transitions.

4. A $\Delta\mu/\mu$ CONSTRAINT 1.5 BILLION YEARS AFTER THE BIG BANG

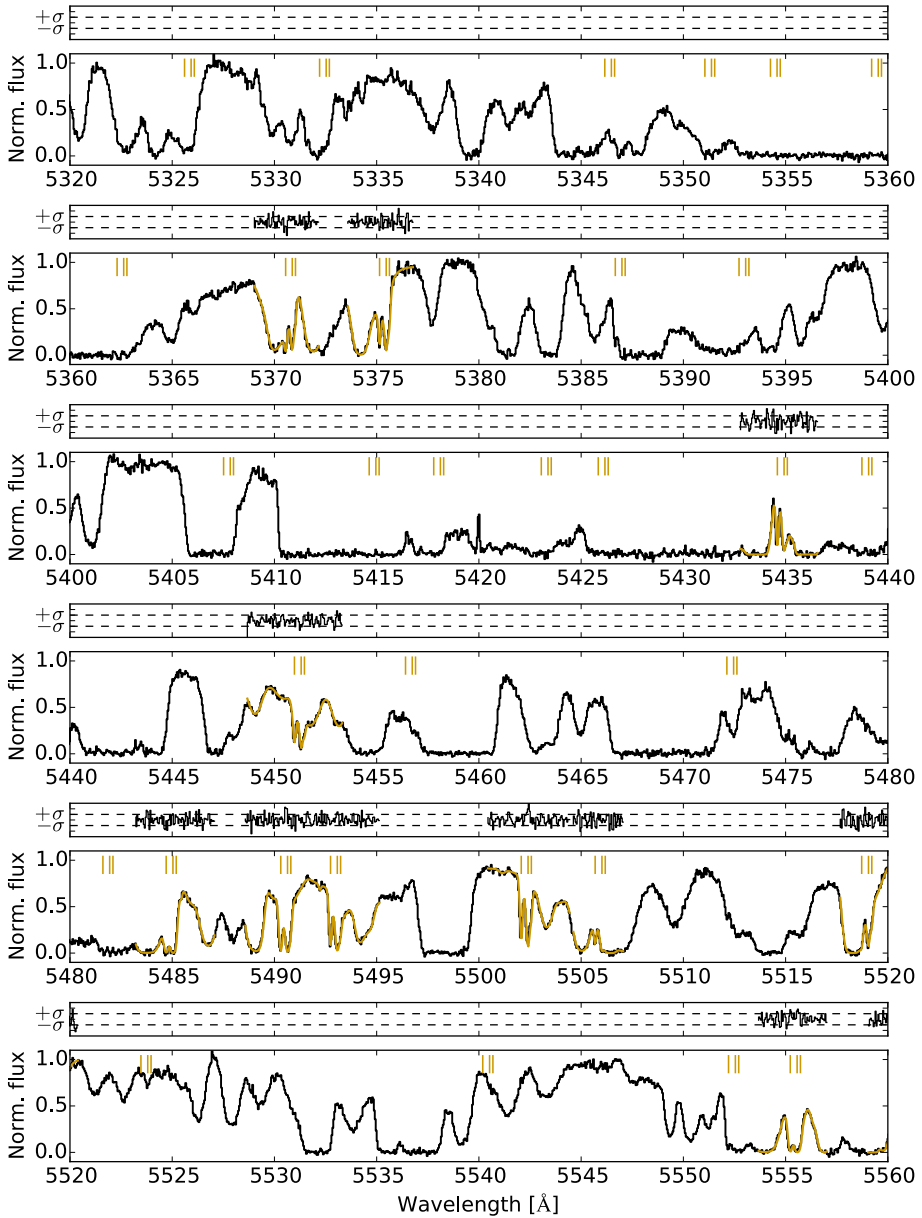


Figure 4.7: Part 3 of 4 of the J1443+2724 spectrum with fitted H₂ transitions.

4. A $\Delta\mu/\mu$ CONSTRAINT 1.5 BILLION YEARS AFTER THE BIG BANG

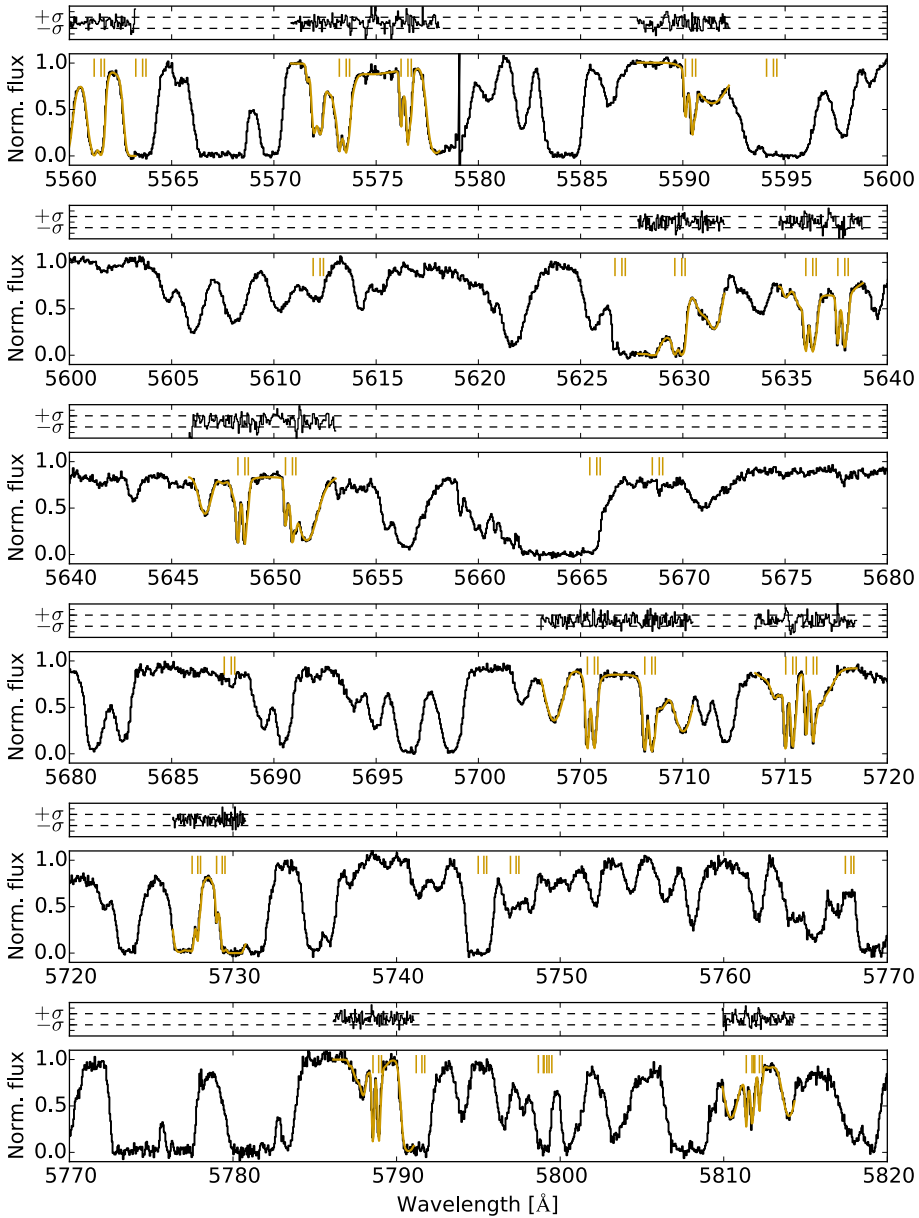


Figure 4.8: Part 4 of 4 of the J1443+2724 spectrum with fitted H₂ transitions.

Continuum error

One possible source of uncertainty in $\Delta\mu/\mu$ can in principle be caused by incorrect treatment of the continuum; we address it here. One can assume that, for 60 fitted sections (containing the 89 H_2 lines), the continuum error is random, with the error in the slope of the continuum over any individual H_2 section (of width ~ 100 km/s) being Gaussian-distributed with a sigma of approximately 0.05 [norm. flux units] / 100 km/s = 5×10^{-4} per km/s. Individual H_2 transitions are ~ 40 km/s wide in this absorber, so this corresponds to an incorrect continuum slope of $\sim 2 \times 10^{-3}$ across the transition. To a reasonable approximation, this should impart a spurious shift to the fitted centroid of 0.002 times the width, i.e. 40 km/s again, or a shift of ~ 80 m/s for an individual line. Some of the 89 lines are blended together and therefore share the same spurious shift. Thus, effectively a sample of ~ 70 transitions reduces the per-line error of 80 m/s down to a total error budget of $80/\sqrt{70} \approx 10$ m/s, which is well below our systematic or random error budgets.

The global quasar continuum assumed initially is just a nominal starting guess which is refined by introducing local continua to each fitting region. These local continua are either constants or straight lines so that degeneracies with broad Ly- α lines would be avoided. Therefore, errors in the global continuum level in each fitting section are marginalized over by fitting a local continuum with a slope and also fitting the broader H I Ly- α lines.

Varying the minimum linewidth parameter

The minimum linewidth parameter b_{\min} in VPFIT is user-defined. Throughout the paper, we use a $b_{\min} = 0.2$ km/s. In the case of J1443+2724, one of the H_2 velocity components reaches this limit. This is likely unphysical because $b_{\text{H}_2} = 0.2$ km/s corresponds to $T \sim 5$ K, while the temperature of the Cosmic Microwave Background radiation at $z = 4.224$ corresponds to $T = 14$ K or $b_{\text{H}_2} = 0.3$ km/s. Furthermore, the kinetic temperature in cold molecular clouds is typically around ~ 100 K or $b_{\text{H}_2} = 0.9$ km/s. In Fig. 4.9, we show how imposing these values as b_{\min} affects $\Delta\mu/\mu$. Overall, the resulting $\Delta\mu/\mu$ values are in agreement with the fiducial $\Delta\mu/\mu$ limit from the 3VC model with $b_{\min} = 0.2$ km/s. However, the goodness of fit parameter χ_ν^2 increases with increasing b_{\min} values. For example, a χ_ν^2 of 1.161 results from the 3VC model with $b_{\min} = 0.2$ km/s, and $\chi_\nu^2 = 1.189$ from the same model with $b_{\min} = 0.9$ km/s. This indicates that the former model is statistically preferred over the latter.

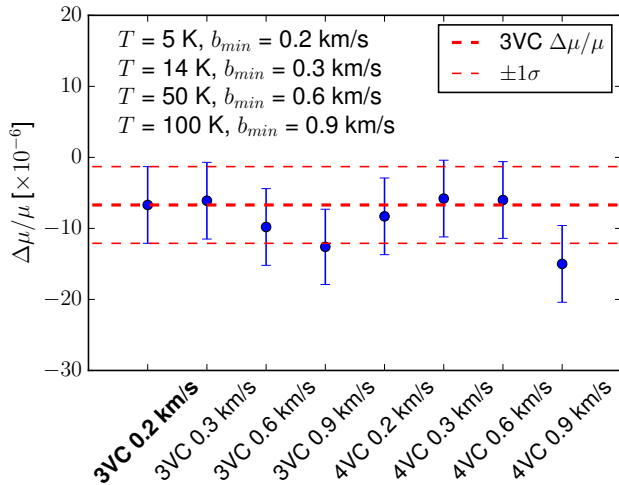


Figure 4.9: Results of fitting the J1443+2724 spectrum with different minimum width parameter b_{\min} . For the H_2 molecule, the Cosmic Microwave Background radiation at $z = 4.224$ corresponds to $T = 14$ K. The kinetic temperature in cold molecular clouds typically amounts to 50 – 100 K.

Supercalibration

Long-range wavelength distortions in UVES can be quantified by means of a so-called supercalibration method which is based on observations of objects with well understood spectra [19, 32]. In particular, these objects can be asteroids or solar twins which both exhibit solar-like spectra. Their observations include the usual ThAr calibration routine, used also for the quasar, and the resulting spectra are compared to a highly accurate solar spectrum obtained by an independent instrument, namely Fourier Transform Spectrometer (FTS). The comparison provides means to verify correctness of the ThAr calibration and to make adjustments if it is found to be flawed.

In Table 4.4, observational details are provided regarding the J1443+2724 observing runs both in 2004 and 2013. The service mode J1443+2724 observations were conducted during 2–3 and 17–19 of March, 2004. Note that most of the total SNR of the J1443+2724 spectrum originates from this dataset (see Table 4.6). Even though dedicated asteroid or solar twin observations were not carried out along with the quasar observations, incidentally, on the ESO archive we could find several Sun-like stars observed during that time period under a different program; their observational details are collected in Table 4.5.

It has to be noted that even though the same arm of the spectrograph was used, the settings of the quasar observations and those of the Sun-like stars were not identical. By applying the supercalibration method described above, we found corrections amounting to 44.9 ± 46.8 m/s/1000 Å (see Fig. 4.10). Here we assume that the distortions remain semistable over time periods as long as several weeks, and that the slopes obtained from the solar twins hold also for the main target. The resulting $\Delta\mu/\mu$ correction amounts to $(-2.8 \pm 1.6_{\text{sys}}) \times 10^{-6}$.

Asteroids Juno and Flora, and the solar twin HD126525 were observed along with J1443+2724 in March 2013. The instrumental settings of the quasar observations were maintained during the observations of calibration sources: a 544 or 520 nm central wavelength, 2x2 CCD binning, 0.8 slit. For this sample of solar-like spectra, a significant deviation from perfect calibration was found with an average slope value of the correction amounting to 297.6 ± 122.7 m/s/1000 Å. In a study of H₂ toward B0642–5038, a miscalibration of similar size yielded a $\Delta\mu/\mu$ correction of -10×10^{-6} [59]. Fitting the uncorrected 2013 subspectrum results in $\Delta\mu/\mu = (4.0 \pm 12.4) \times 10^{-6}$ for the 3VC model. If a correction is applied a $\Delta\mu/\mu$ of $(-9.3 \pm 12.4) \times 10^{-6}$ is obtained. Because of a low SNR, it is difficult to reliably estimate the uncertainty of this shift. Hence, we do not correct the present 2013 subspectrum of J1443+2724.

Table 4.4: ESO archival data of the J1443+2724 observations with VLT/UVES (program IDs: 072.A-0346(B) and 090.A-0304(A)). The archival exposure name contains the date and time of the observations.

Archival exposure name	Central wavelength [nm]	CCD binning	Slitwidth ['']	Integ. time [s]
UVES.2004-03-02T07:52:43.078.fits	580	2x2	1.0	5225.00
UVES.2004-03-03T08:12:39.143.fits	580	2x2	1.0	5016.00
UVES.2004-03-17T08:14:13.810.fits	580	2x2	1.0	5091.00
UVES.2004-03-18T06:53:02.273.fits	580	2x2	1.0	5225.00
UVES.2004-03-19T06:35:36.823.fits	580	2x2	1.0	5800.00
UVES.2013-03-28T05:15:58.805.fits	544	2x2	0.8	4800.00
UVES.2013-03-28T06:39:39.743.fits	544	2x2	0.8	4800.00
UVES.2013-03-28T08:02:50.876.fits	544	2x2	0.8	4800.00
UVES.2013-03-29T05:22:20.681.fits	544	2x2	0.8	4800.00
UVES.2013-03-29T06:45:12.579.fits	544	2x2	0.8	4800.00
UVES.2013-03-29T08:10:27.130.fits	544	2x2	0.8	4800.00
UVES.2013-03-30T05:03:29.905.fits	520	2x2	0.8	4800.00
UVES.2013-03-30T06:28:32.340.fits	520	2x2	0.8	4800.00
UVES.2013-03-30T07:51:11.513.fits	520	2x2	0.8	6000.00
UVES.2013-03-31T05:03:05.640.fits	544	2x2	0.8	4800.00
UVES.2013-03-31T06:25:58.450.fits	544	2x2	0.8	4800.00
UVES.2013-03-31T07:49:11.563.fits	544	2x2	0.8	6300.00

Table 4.5: ESO archival data of several Sun-like stars observed in 2004 (program IDs: 072.D-0739(A) and 072.B-0179(A)), at a similar time when also part of the J1443+2724 data were taken. The archival exposure name contains the date and time of the observations.

Target	Archival exposure name	Central wavelength [nm]	CCD binning	Slitwidth ["]
HDI40538	UVES.2004-03-04T08:11:03.429.fits	860	2x2	1.0
HDI40538	UVES.2004-03-04T08:11:06.685.fits	390	2x2	1.0
Hip64345	UVES.2004-03-12T07:14:53.472.fits	564	1x1	0.3
Hip67534	UVES.2004-03-12T08:09:56.593.fits	564	1x1	0.3
Hip64459	UVES.2004-03-25T07:43:09.439.fits	564	1x1	0.3
Hip64459	UVES.2004-03-25T07:46:30.774.fits	564	1x1	0.3
Hip99224	UVES.2004-03-25T09:12:28.662.fits	564	1x1	0.3
Hip99224	UVES.2004-03-25T09:22:46.173.fits	564	1x1	0.3
Hip102793	UVES.2004-03-28T09:01:15.687.fits	564	1x1	0.3
Hip102793	UVES.2004-03-28T09:17:43.306.fits	564	1x1	0.3

4. A $\Delta\mu/\mu$ CONSTRAINT 1.5 BILLION YEARS AFTER THE BIG BANG

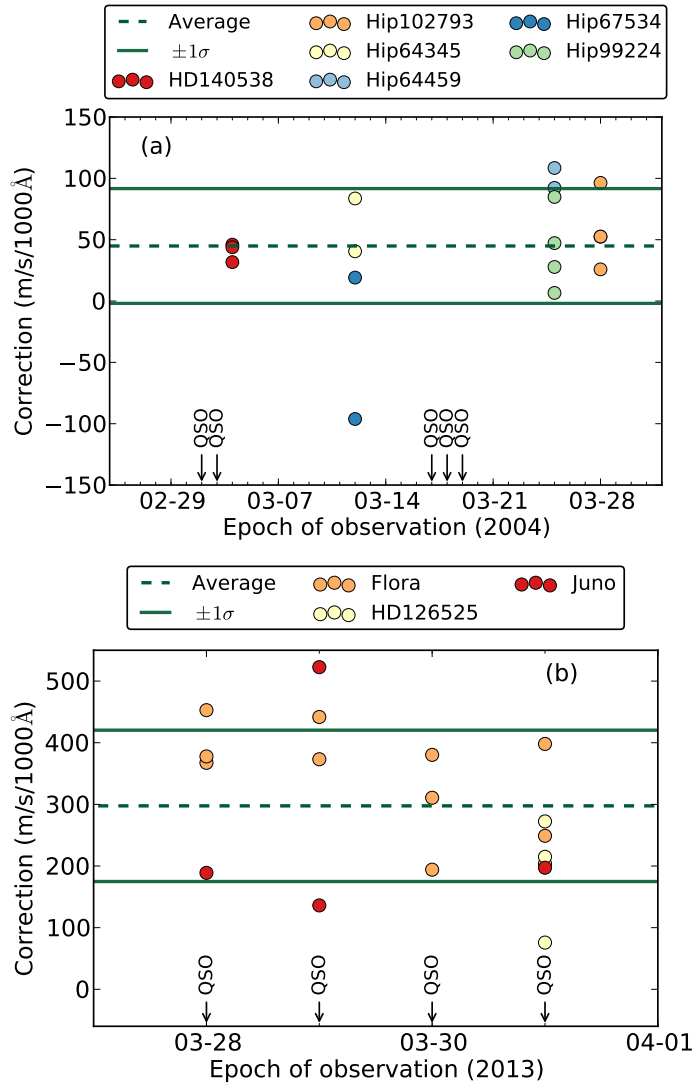


Figure 4.10: (a) Supercalibration results from 2004. The average correction value amounts to 44.9 ± 46.8 m/s/1000Å. (b) Supercalibration results from 2013. The average correction value amounts to 297.6 ± 122.7 m/s/1000Å.

Table 4.6: Representative signal-to-noise (SNR) values measured in the continuum of the J1443+2724 spectrum. The redshifted H₂ transitions are found in the range between 484 and 581 nm. The total spectrum is a combination of two datasets obtained independently in 2004 and 2013. The SNR at shorter wavelengths is entirely dominated by the data from 2004 as the observations in 2013 were affected by the presence of the full moon.

λ [nm]	SNR _{tot}	SNR ₂₀₀₄
501.5	25	23
528.5	30	26
560.0	48	39

Limits on a gravitational field dependence of the proton–electron mass ratio from H₂ in white dwarf stars

Bagdonaite, J., Salumbides, E. J., Preval, S. P., Barstow, M. A., Barrow, J. D., Murphy, M. T. & Ubachs, W. Phys. Rev. Lett. 113, 123002 (2014).

Abstract

Spectra of molecular hydrogen (H₂) are employed to search for a possible proton-to-electron mass ratio (μ) dependence on gravity. The Lyman transitions of H₂, observed with the Hubble Space Telescope towards white dwarf stars that underwent a gravitational collapse, are compared to accurate laboratory spectra taking into account the high temperature conditions ($T \sim 13\,000$ K) of their photospheres. We derive sensitivity coefficients K_i which define how the individual H₂ transitions shift due to μ dependence. The spectrum of white dwarf star GD133 yields a $\Delta\mu/\mu$ constraint of $(-2.7 \pm 4.7_{\text{stat}} \pm 0.2_{\text{syst}}) \times 10^{-5}$ for a local environment of a gravitational potential $\phi \sim 10^4 \phi_{\text{Earth}}$, while that of G29–38 yields $\Delta\mu/\mu = (-5.8 \pm 3.8_{\text{stat}} \pm 0.3_{\text{syst}}) \times 10^{-5}$ for a potential of $2 \times 10^4 \phi_{\text{Earth}}$.

Theories of high-energy physics with a nonunique vacuum state, that invoke extra dimensions, or contain new light scalar fields can permit or require space-time variations of the fundamental low-energy ‘constants’ of nature [16, 10]. Small time variations of nongravitational constants have negligible effects on the expansion dynamics of the universe but have potentially observable effects on astronomical spectra. Self-consistent scalar-tensor theories for the variation of these constants (analogous to Brans-Dicke theory [159] for a varying gravitation ‘constant’, G) are needed to evaluate their full cosmological consequences. Theoretical studies have focused on a varying fine-structure constant α , which is simplest to develop because of its gauge symmetry [17, 160], and a varying proton-electron mass ratio $\mu \equiv m_p/m_e$ [161, 162]. Scaling arguments have been used to relate changes in α , to changes in μ using the internal structure of the standard model, including supersymmetry [163]. Typically (in the absence of unusual cancellations involving the rates of change of α , and the supersymmetry-breaking and grand unification energy scales), they predict that changes in μ at low energies should be about an order of magnitude greater than those in α . However, high-redshift cosmological bounds on μ variation are expected to be weaker than those from laboratory tests of the equivalence principle [161]. Indications of possible variations of α in time [33] and space [35] and time variations in μ [55] have been reported. Systematic investigations of the spectra of cold H_2 towards quasar sources have now produced a constraint on μ variation over cosmological time scales yielding $\Delta\mu/\mu < 1 \times 10^{-5}$ at redshifts $z = 2-3.5$ corresponding to look-back times of 10–12 Gyr [62, 59].

Besides dependencies on cosmological scales, the couplings between light scalar fields and other fields can generate dependencies of coupling strengths on the local matter density [17, 22], or on local gravitational fields [164, 23]. Such couplings violate the Einstein equivalence principle that is fundamental to general relativity [159, 165]. The gravitational potential at distance R from an object of mass M is commonly expressed in dimensionless units of $\phi = GM/(Rc^2)$. A number of studies have been performed using ultrastable lasers and atomic clocks exploiting the eccentricity of Earth’s orbit [166, 167, 168] causing sinusoidal changes of $\Delta\phi = 3 \times 10^{-10}$. Recently, a spectroscopic study of Fe V and Ni V ions in the local environment of the photosphere of a white dwarf was employed to assess the dependence of α in a strong gravitational field ($\phi = 4.9 \times 10^{-5}$) [92]. In the present study we use the spectrum of molecular hydrogen in the photosphere of two white dwarfs, GD133 (WD 1116+026) and G29–38 (WD 2326+049), obtained with the Cosmic Origins Spectrograph on the Hubble Space Telescope [91], to probe a possible dependence of μ on a gravitational potential that is $\sim 10^4$ times stronger than its value at Earth’s surface (which is actually dominated by the contribution from the Sun’s potential).

In Fig. 5.1 an overview of the H_2 absorption lines in the G29–38 photosphere is shown for the wavelength range 1337–1347 Å. The total spectrum

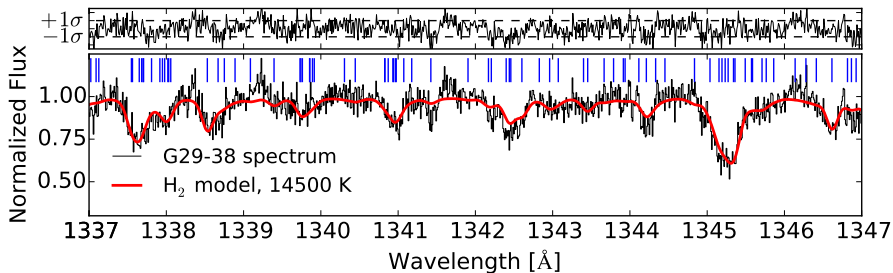


Figure 5.1: Part of the white dwarf G29–38 spectrum in the range between 1337 and 1347 Å. Positions of the $B^1\Sigma_u^+ - X^1\Sigma_g^+$ Lyman band H_2 transitions falling within this window are indicated with (blue) sticks. Overplotted (in red) on the spectrum is an absorption model based on the indicated transitions while the corresponding normalized residuals are shown at the top. To create the model, a set of fixed parameters known from molecular physics (transition rest-wavelength, λ_i , oscillator strength, f_{ik} , damping parameter, Γ_i) is combined with a partition function, $P_{v,J}(T)$, which defines level population at a temperature T . Even though this model includes many transitions, fitting it to the data requires only 4 free parameters: total column density N , redshift z , linewidth b , and temperature T . The total fitted spectrum extends from 1310.7 Å to 1411.7 Å (see Fig. 5.4–5.7).

covers wavelengths from 1144 to 1444 Å. The data of both G29–38 and GD133 were retrieved from the Hubble Space Telescope archive.¹ The individual exposures (3 of G29–38 and 5 of GD133) were rebinned to a common wavelength scale and combined using the same techniques as in [62, 59]. For both stars, lines pertaining to the $B^1\Sigma_u^+ - X^1\Sigma_g^+$ Lyman band are solidly detected in the range 1298–1444 Å at a signal-to-noise ratio of ~ 15 . The $C^1\Pi_u - X^1\Sigma_g^+$ Werner band transitions fall in the range 1144–1290 Å at a lower signal-to-noise ratio of ~ 5 and are only weakly detected and thus are not considered in the present analysis. Because of the high temperature in the photosphere, the observed H_2 lines are from multiple vibrationally – and rotationally – excited levels of the ground electronic state. The most intense H_2 Lyman transitions involve the $B - X$ (v', v'') bands for $v' = 0 - 2$ and $v'' = 1 - 5$ vibrational levels with the highest population in the $J'' = 8$ level (at $T = 13\,000$ K).

The laboratory wavelengths are derived from combination differences using level energies in the $B^1\Sigma_u^+, v', J'$ states from Refs. [118, 169]. The $X^1\Sigma_g^+$

¹HST archive, Cycle 18, program 12290, PI M. Jura.

Table 5.1: The most intense H₂ transitions observed in GD133 and G29–38 spectra. Wavelengths in Å, with uncertainties in between parentheses given in units of the last digit. The calculated sensitivity coefficients K_i and the oscillator strengths f_{ik} are listed in the last two columns.

B, v'	X, v''	Transition	Wavelength	K_i	f_{ik}
0	3	R(9)	1 313.376 43 (2)	-0.106	0.0494
0	3	P(9)	1 324.595 01 (2)	-0.115	0.0538
0	3	P(11)	1 345.177 88 (2)	-0.129	0.0508
0	4	R(7)	1 356.487 60 (2)	-0.114	0.0821
0	4	R(9)	1 371.422 41 (2)	-0.125	0.0816
0	4	R(11)	1 389.593 79 (2)	-0.138	0.0816
0	4	R(13)	1 410.648 (1)	-0.152	0.0821
0	4	P(9)	1 383.659 16 (2)	-0.134	0.0739
0	4	P(11)	1 403.982 60 (2)	-0.148	0.0765
0	4	P(13)	1 427.013 40 (2)	-0.163	0.0793

ground state level energies used in the derivation are from *ab initio* calculations including relativistic and quantum electrodynamical effects [170], with estimated uncertainties better than 0.001 cm^{-1} , which were tested in metrology laser experiments [133, 171]. The most accurate transition wavelengths are those derived from Ref. [118] (for $J' < 14$) with relative accuracies at the 10^{-8} level, while those derived from Ref. [169], for higher J' quantum numbers, exhibit relative accuracies of 10^{-6} . When the level energies from Ref. [169] are used, an energy correction for each band is applied (typically $0.04\text{--}0.06 \text{ cm}^{-1}$) based on the comparison of Refs. [118, 169] at low J quantum numbers. The most intense transitions are listed in Table 5.1, and the complete list involves around 1500 lines [172].

Sensitivity coefficients K_i due to a variation in μ were calculated for each transition i using a semiempirical method based on the experimentally determined level energies. The coefficient K_i is separated into electronic (K_{el}), vibrational (K_{vib}) and rotational (K_{rot}) contributions, which are calculated via

$$K_i = \frac{d \ln \lambda_i}{d \ln \mu} = -\frac{\mu}{E_B - E_X} \left(\frac{dE_B}{d\mu} - \frac{dE_X}{d\mu} \right), \quad (5.1)$$

with $dE_{B,X}/d\mu$ related to $dE_{B,X}/dv$ and $dE_{B,X}/dJ$ to separate the K_{vib} and K_{rot} contributions. In the framework of the Born-Oppenheimer approximation the K_{el} are set to zero. The method is related to the Dunham approach [44], but turns out to be more robust due to the elimination of correlations in the fitting of the parameters of the Dunham matrix. This effect is more problematic for Dunham representations of levels with higher values of quantum numbers v, J ,

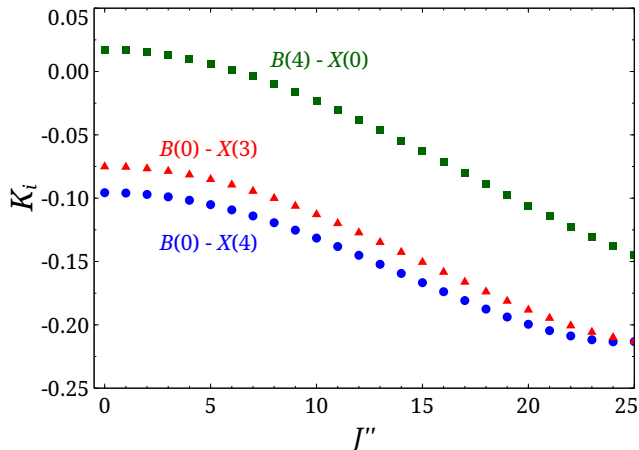


Figure 5.2: K_i coefficients for R branch of the $B(0)-X(4)$ and $B(0)-X(3)$ Lyman bands which include the most intense H_2 transitions in GD133 and GD39–38 spectra. The K_i values for the Lyman $B(4)-X(0)$ band, where low $J'' < 5$ transitions are used in probing μ variation in quasar absorption systems [44], are plotted for comparison.

where the dominant contribution of the higher-order terms in the expansion are susceptible to numerical errors. In contrast, the present method does not have this disadvantage and the accuracy of the K_i values are just limited by the experimental data. The uncertainty of the K_i -coefficients is estimated to be as good as 10^{-4} for the observed Lyman transitions, especially because for $B, v' < 8$ there are no perturbations with the $C^1\Pi_u$ electronic state in the probed wavelength range [44]. The results of the present method were verified to agree with the Dunham approach [44] for low v, J . K_i -coefficients for the strongest Lyman bands observed in both white dwarfs, $B(0)-X(4)$ and $B(0)-X(3)$, are plotted in Fig. 5.2. For comparison, the $B(4)-X(0)$ Lyman band observed in quasar absorption studies are also plotted, showing the higher sensitivity of the $B(0)-X(4)$ band despite the same $|\Delta v| = 4$.

To analyze the white dwarf spectra we do not follow the common procedure [62, 59] of assigning and fitting individual transitions of H_2 . Since they are relatively weak and self-blended we fit them simultaneously over most of the range between 1298 and 1444 Å. We only exclude regions where blends with atomic species occur: the geocoronal O I transitions at 1298–1310 Å, the photospheric and interstellar atomic transitions listed in [173], and part of the spectrum at >1411.7 Å where some previously unidentified atomic transitions have been found. The nonlinear least squares Voigt profile fitting program

VPFIT10.0² is used to model the absorption spectrum of H₂. A Voigt profile represents an absorption line shape involving Doppler broadening, due to thermal motion of the absorbing gas, and Lorentzian broadening arising from the finite lifetimes of the excited states, represented by the damping parameter Γ_i ,³ convolved with an instrumental line spread function.⁴

The intensities of the H₂ absorption lines are described by the product of the oscillator strength f_{ik} and the normalized population of the ground rovibrational level, calculated from a partition function at a temperature T :

$$P_{v,J}(T) = \frac{g_n(2J+1)e^{-\frac{E_{v,J}}{kT}}}{\sum_{v=0}^{v_{\max}} \sum_{J=0}^{J_{\max}(v)} g_n(2J+1)e^{-\frac{E_{v,J}}{kT}}}, \quad (5.2)$$

where g_n is the nuclear statistical weight. Consequently, all lines probing odd- J levels (ortho-H₂) benefit in relative strength from the 3:1 spin statistics ratio between ortho- and paralevels. Invoking this definition of line strengths leads to a model which essentially requires only 4 free parameters: total column density of the gas N , redshift of the absorbing cloud z , linewidth b , and temperature T . Once the fit is optimized, we introduce an additional free parameter $\Delta\mu/\mu$ which allows for small relative line shifts that are governed by the calculated sensitivity coefficients K_i :

$$\frac{\lambda_i^{\text{WD}}}{\lambda_i^0} = (1 + z_{\text{WD}})\left(1 + \frac{\Delta\mu}{\mu} K_i\right), \quad (5.3)$$

where λ_i^{WD} represents the transition wavelength observed in the white dwarf spectra and λ_i^0 is a corresponding wavelength measured in the laboratory. Models of different temperatures were fitted to the data (Fig. 5.3), resulting in a best-fit temperature of $T = (11\,800 \pm 450)$ K for GD133 and $T = (14\,500 \pm 300)$ K for G29–38. Displayed in Fig. 5.1 are fitting results of the G29–38 spectrum, where the model is based on a total of ~ 870 H₂ transitions with the relative strengths defined for $T = 14\,500$ K. The derived H₂ temperature is in good agreement with independent temperature determinations from Balmer-H lines for GD133 but differs for GD29–38 [175]. For either star, measurements of $\Delta\mu/\mu$ are only slightly affected by the choice of temperature, as shown in Fig. 5.3. The best-fit model of GD29–38 yields $\Delta\mu/\mu = (-6.1 \pm 3.9) \times 10^{-5}$, and the one of GD133 results in $\Delta\mu/\mu = (-1.8 \pm 5.0) \times 10^{-5}$. The adequacy

²Developed by R. F. Carswell et al.; <http://www.ast.cam.ac.uk/~rfc/vpfit.html>.

³For the present list of H₂ transitions Γ_i parameters correspond to the total radiative transition probabilities from [174].

⁴We use the COS/HST ‘lifetime position=2’ instrumental profiles provided at: http://www.stsci.edu/hst/cos/performance/spectral_resolution/.

of the fit is reflected by the reduced χ_ν^2 of ~ 0.8 - 0.9 , where the number of degrees of freedom ν is equal to 9633 for both spectra. A column density $\log[N/\text{cm}^{-2}] = (15.849 \pm 0.007)$, a linewidth $b = (14.55 \pm 0.58) \text{ km s}^{-1}$, and a redshift $z = 0.0001820(10)$ were measured for GD133. For G29–38 the results are $\log[N/\text{cm}^{-2}] = (15.491 \pm 0.005)$, $b = (18.65 \pm 0.42) \text{ km s}^{-1}$, and $z = 0.0001360(8)$.⁵ The quoted widths b are deconvolved from the instrument profile, $\text{FWHM} \simeq 17 \text{ km s}^{-1}$.

The measured redshifts of $z_{\text{WD}} \sim 10^{-4}$ are primarily determined by the gravitational redshift associated with the local potential in the white dwarf photospheres, with contribution from the proper motion of the objects and from the uncertainty of the absolute wavelength calibration of the COS instrument, amounting to 1/3 of the measured redshift value. For a $\Delta\mu/\mu$ analysis, the relative wavelength calibration accuracy is of the utmost importance. If not taken into account, velocity distortions – velocity shifts which change with wavelength – may have a significant effect on $\Delta\mu/\mu$ measurements [59]. We searched for such distortions by applying the ‘direct comparison method’ [145] to individual exposures against the combined spectra. The direct comparison method is a model-independent technique of comparing pairs of spectra in order to detect and correct for velocity shifts. No evidence for relative distortions between exposures was found, with $1\text{-}\sigma$ limits of $\Delta v' < 25 \text{ m s}^{-1} \text{ nm}^{-1}$ per exposure. Applying artificial distortions of $\Delta v'/\sqrt{3}$ and $\Delta v'/\sqrt{5}$ to the combined 3 exposures of G29–38 and the 5 of GD133 produces systematic shifts in $\Delta\mu/\mu$ of $\sigma_{\text{syst}} = \pm 0.3$ and $\pm 0.2 \times 10^{-5}$, respectively. The same analysis also allows us to correct the combined spectra for small relative shifts ($< 0.2 \text{ km s}^{-1}$) between individual exposures. The corrected spectra, plus the above estimate of systematic errors, provide our fiducial measurements: $\Delta\mu/\mu = (-5.8 \pm 3.8_{\text{stat}} \pm 0.3_{\text{syst}}) \times 10^{-5}$ for G29–38 and $(-2.7 \pm 4.7_{\text{stat}} \pm 0.2_{\text{syst}}) \times 10^{-5}$ for GD133.

The line broadenings of 15 and 19 km s^{-1} are primarily determined by gas kinetics at the prevailing temperatures of $T = 12\,000\text{--}14\,000 \text{ K}$ yielding $b_{\text{therm}} \sim 10 \text{ km s}^{-1}$, with $b_{\text{therm}} = \sqrt{2kT/m}$, where k is the Boltzmann con-

⁵Updated values of the fitted T , z , b , N , and $\Delta\mu/\mu$ parameters are presented in the follow-up paper of the current analysis [172]. The follow-up paper is focused on calculation of the sensitivity coefficients K_i , and the fitting of the spectra involved both the updated values of the sensitivity coefficients and a refined treatment of the normalization of the temperature-dependent populations. For GD133, the updated best-fit model resulted in a temperature of $T = (11\,100 \pm 470) \text{ K}$, a redshift of $z = 0.0001819(11)$, a linewidth of $b = (14.50 \pm 0.58) \text{ km s}^{-1}$, a column density of $\log[N/\text{cm}^{-2}] = (15.817 \pm 0.007)$, and a relative constraint of a μ variation of $\Delta\mu/\mu = (-2.3 \pm 5.0) \times 10^{-5}$. For G29–38 the results are $T = (13\,500 \pm 340) \text{ K}$, $z = 0.0001358(8)$, $b = (18.29 \pm 0.42) \text{ km s}^{-1}$, $\log[N/\text{cm}^{-2}] = (15.959 \pm 0.005)$, and $\Delta\mu/\mu = (-5.8 \pm 3.7) \times 10^{-5}$. These values are obtained without taking into account the (small) wavelength scale distortions that are discussed in the next paragraph.

stant, and m the molecular mass. It can be estimated that an H_2 absorption cloud of 10 km depth in the photosphere of GD133 would be subject to a ‘gravitational width’ of $(\Delta\lambda/\lambda)_{\text{grav}} = 3.2 \times 10^{-8}$ or only $b_{\text{grav}} = 0.01 \text{ km s}^{-1}$ with a similarly small estimate for G29–38. From a photospheric model the maximum H_2 molecular density ($n(\text{H}_2)/n(\text{H})=10^{-5}$) was found to coincide with a total material density of $\rho = 1.5 \times 10^{-7} \text{ g cm}^{-3}$ [173] amounting to ~ 3 mbar for a H atmosphere. This would translate into a broadening of $b_{\text{col}} < 0.001 \text{ km s}^{-1}$.

Stark and Zeeman broadening effects on the H_2 lines are assumed to be small because the excited state $B^1\Sigma_u^+$ for the Lyman bands is of valence character and only weakly susceptible to external fields; no laboratory measurements of Stark and Zeeman effects have been reported for the molecular Lyman bands. G29–38 is a well-studied irregular pulsator, with time-evolving dominant periods of a few hundred seconds resulting in velocity shifts of atomic hydrogen transitions as large as 16.5 km s^{-1} [176]. In the case of GD133 pulsations occur at a dominant period of 120 s and are much weaker than in G29–38 [177]. In either case, the pulsation period is smaller than the exposure times that exceed 2000 s and, thus, the H_2 spectra in individual exposures and the combined spectra will be smeared out by this effect.

The broadening effects outlined here mainly affect the resolution of the spectra and the accuracy of the constraint on $\Delta\mu/\mu$. They should not affect the symmetry of the H_2 absorption lines, and even if they did, the effect would be the same for all transitions and thus it is unlikely to mimic μ variation.

The above constraints on $\Delta\mu/\mu$ from the white dwarf spectra can be interpreted in terms of a dependence on a dimensionless gravitational potential [164, 23], $\Delta\phi$, where a Taylor series expansion up to the second order can be used to specifically probe strong field gravitational phenomena:

$$\frac{\Delta\mu}{\mu} = k_{\mu}^{(1)}\Delta\phi + k_{\mu}^{(2)}(\Delta\phi)^2. \quad (5.4)$$

The linear term can be constrained most directly from a laboratory spectroscopic investigation of SF_6 molecules aimed to detect a temporal variation of the proton-to-electron mass ratio [28]. We estimate from the results presented in Ref. [28] that the seasonal difference amounts to $|\Delta\mu/\mu| < 10^{-13}$. Invoking a gravitational potential at the Earth’s surface of $\phi_{\text{Earth}} = 0.98 \times 10^{-8}$ (due to the field produced by the Sun) and an Earth orbit eccentricity of $\epsilon = 0.0167$ leading to a 2.6% effect on the difference in the potential between aphelion and perihelion in the current epoch, the laser spectroscopic experiment yields $k_{\mu}^{(1)} < 4 \times 10^{-4}$.⁶ Other Earth-based spectroscopic investigations (and combinations thereof) yield even tighter constraints of $k_{\mu}^{(1)} <$

⁶It is noted that most of the spectroscopic measurements of [28] were fortuitously taken at the aphelion period (July 2005 and 2006), while some were recorded at perihelion (in 2004 and 2006), thus probing the maximum potential difference produced during Earth’s orbit.

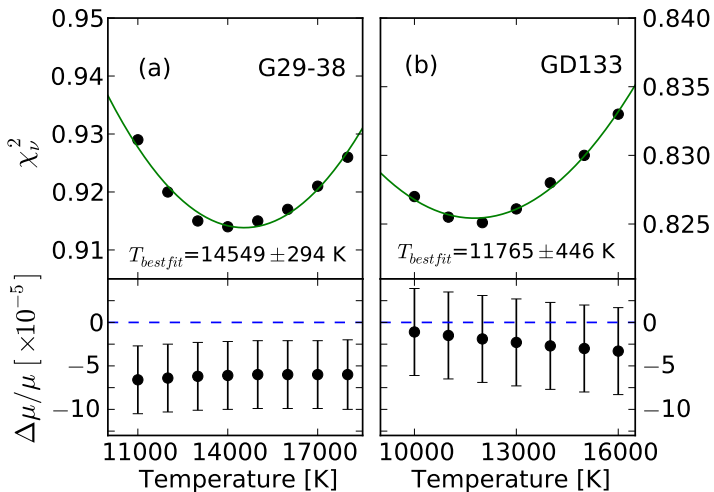


Figure 5.3: (a) Top: Reduced χ^2 from fitted H_2 models with varied temperatures, resulting in a value for temperature of H_2 in the G29–38 photosphere as indicated. Bottom: Measurements of $\Delta\mu/\mu$ invoking partition functions at different temperatures. (b) Same for GD133.

$(4.9 \pm 3.9) \times 10^{-5}$ [166, 167], and $k_{\mu}^{(1)} < (-1.3 \pm 1.7) \times 10^{-5}$ [168], although with model dependence. These results constrain the linear term $k_{\mu}^{(1)}$ more than the present white dwarf study.

The analysis of H_2 spectral lines in the white dwarfs yields $|\Delta\mu/\mu| \lesssim 5 \times 10^{-5}$. The physical properties of GD133 correspond to a gravitational potential $\phi = 1.2 \times 10^{-4}$ in the photosphere at the white-dwarf surface, while that of G29–38 is $\phi = 1.9 \times 10^{-4}$. This delivers a constraint of $k_{\mu}^{(2)} < 1 \times 10^3$, which is several orders of magnitude more stringent than from the Earth-based experiments. This demonstrates that the high gravitational field conditions of white dwarfs (10000 times that on Earth’s surface) is a sensitive probe to constrain $k_{\mu}^{(2)}$. Using the methods presented here, future studies of H_2 in the photospheres of white dwarfs should provide further information on the possible variation of the proton-to-electron mass ratio under conditions of strong gravitational fields.

Acknowledgments

This work was supported by the FOM-Program ‘Broken Mirrors & Drifting Constants’, Science and Technology Facilities Council, the Templeton Foundation and the Australian Research Council (DP110100866). Tyler Evans (Swinburne University of Technology) is thanked for calculating velocity shifts between individual exposures.

Appendix

The spectrum of white dwarf G29–38 is displayed in Fig. 5.4 and 5.5. Positions of the $B^1\Sigma_u^+ - X^1\Sigma_g^+$ Lyman band H_2 transitions falling within this window are indicated with (blue) sticks. Overplotted (in red) on the spectrum is an absorption model based on the indicated transitions while the corresponding normalized residuals are shown at the top. Some metal transitions were found at $z = 0.0001360$ (indicated in green), as well as an interstellar CII transition at $z = 0.0000367$ (in magenta).

For the corresponding GD133 spectrum see Fig. 5.6 and 5.7. In this spectrum, some metal transitions were found at $z = 0.0001820$ (indicated in green), as well as an interstellar CII transition at $z = 0.000050$ (in magenta).

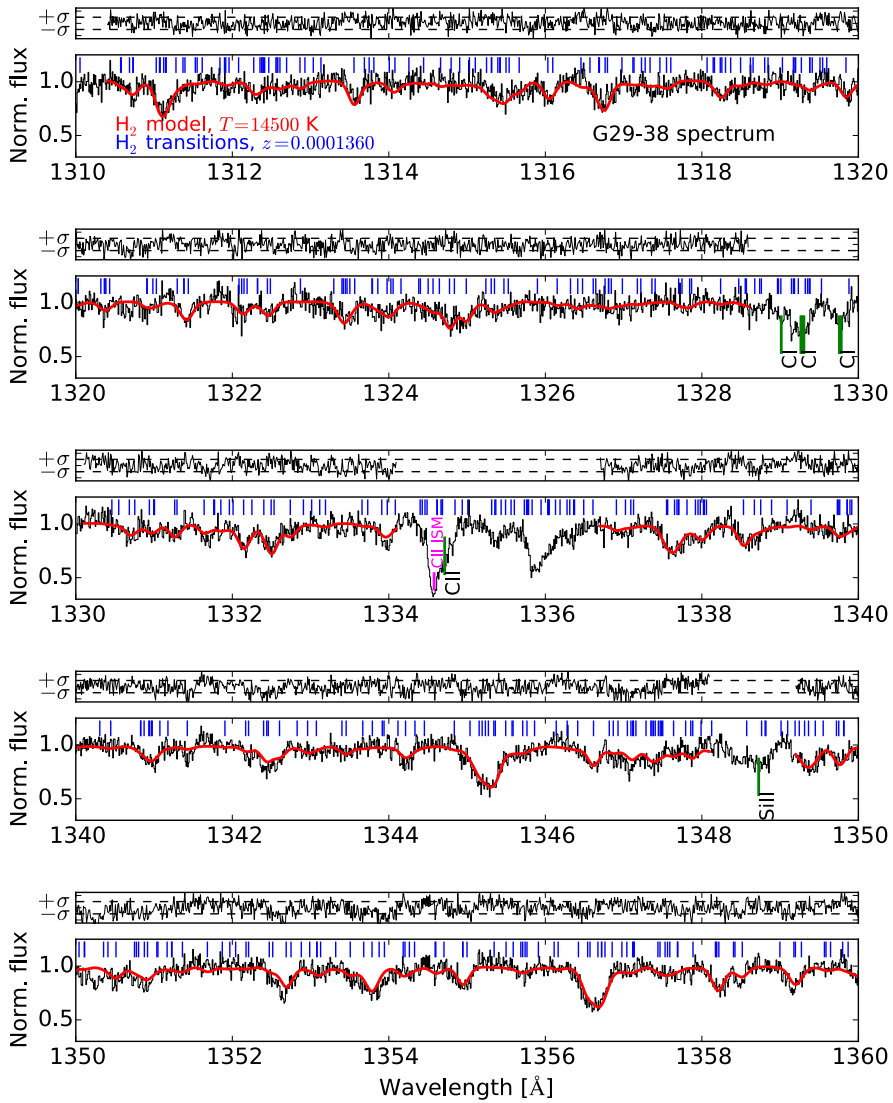


Figure 5.4: Part 1 of 2 of the fitted spectrum of G29-38.

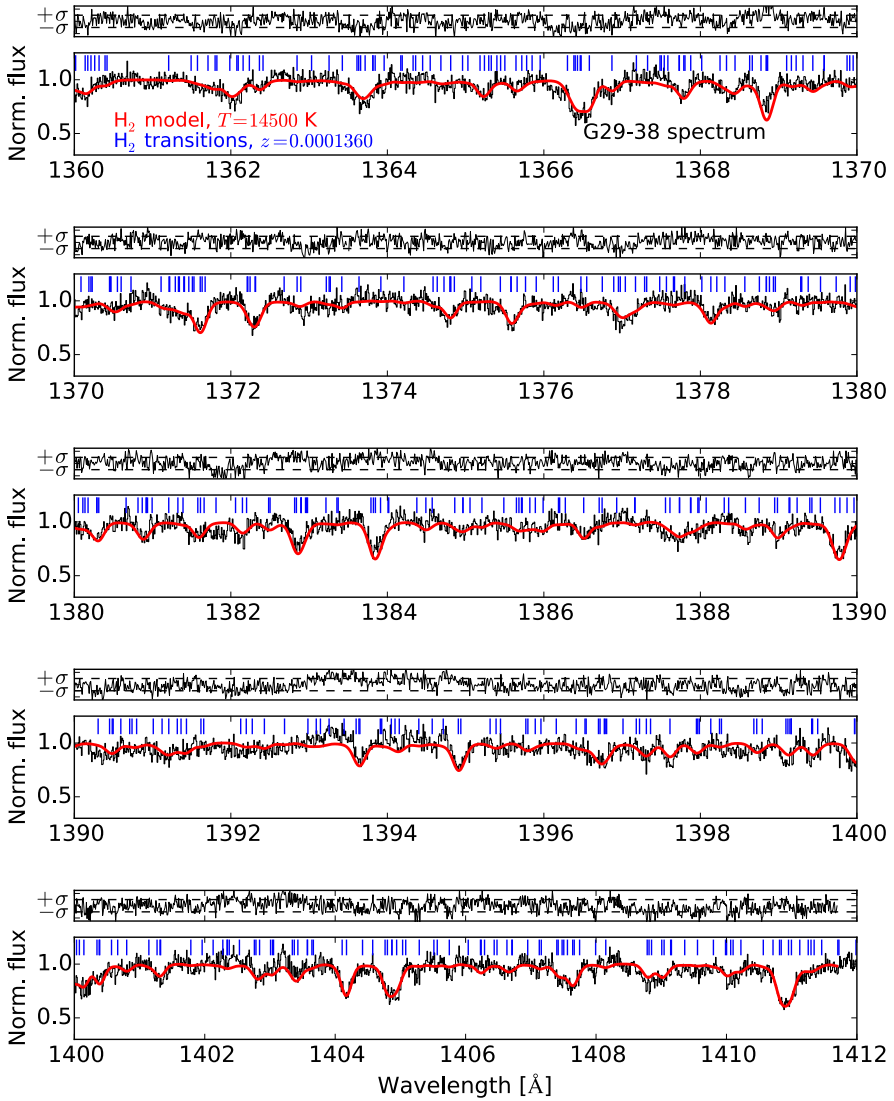


Figure 5.5: Part 2 of 2 of the fitted spectrum of G29–38.

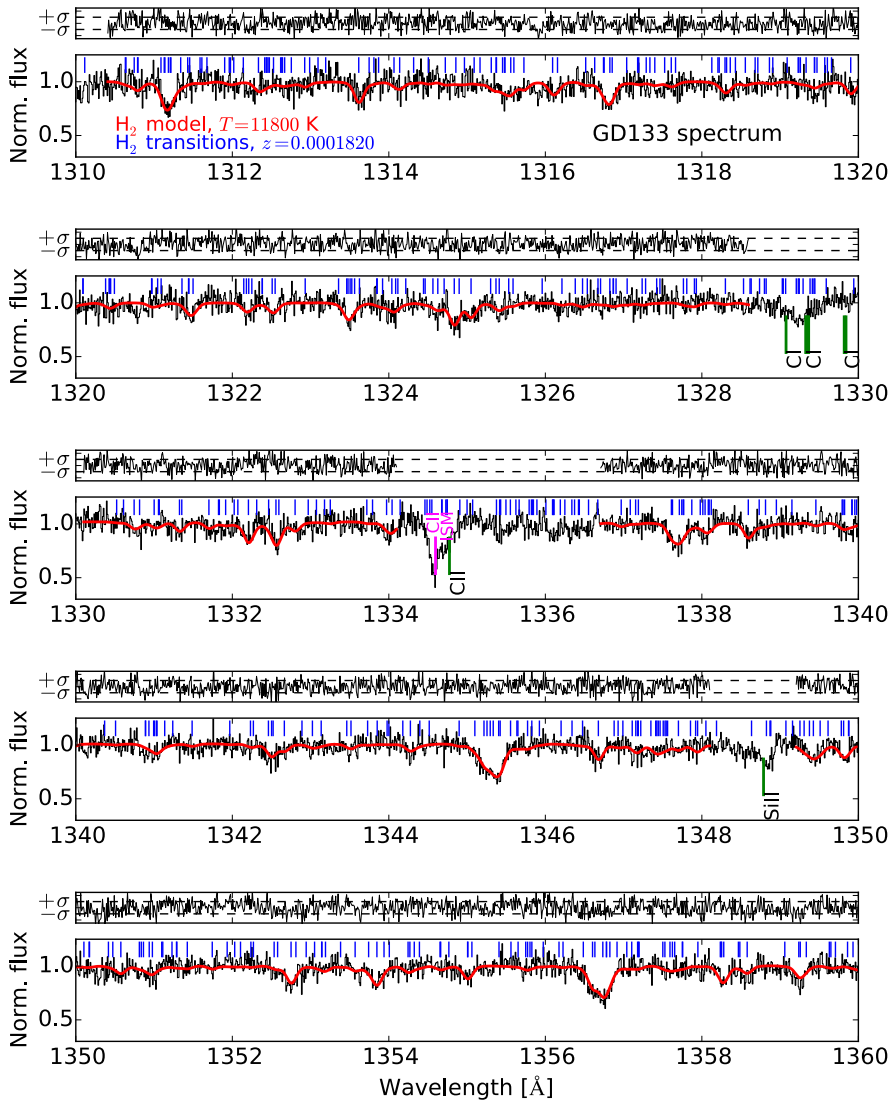


Figure 5.6: Part 1 of 2 of the fitted spectrum of GD133.

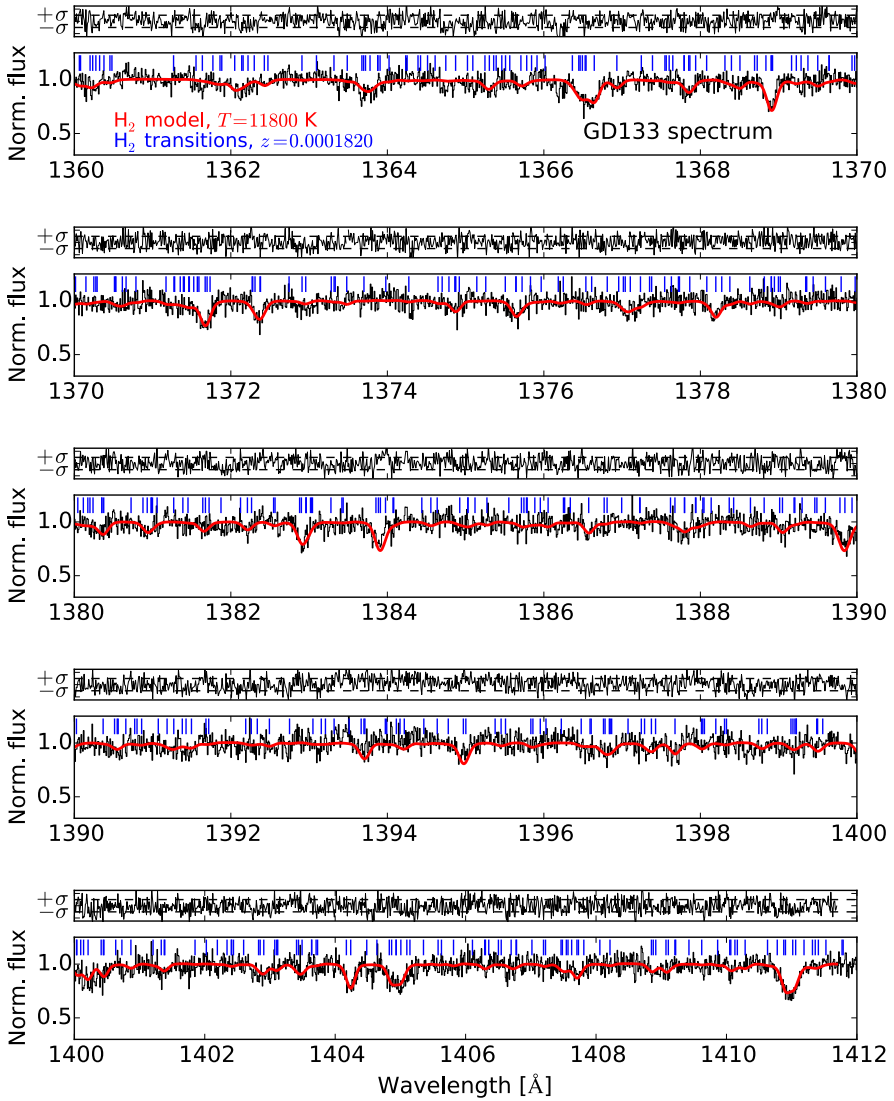


Figure 5.7: Part 2 of 2 of the fitted spectrum of GD133.

A stringent limit on a drifting proton-to-electron mass ratio from alcohol in the early universe

*Bagdonaite, J., Jansen, P., Henkel, C., Bethlem, H. L., Menten, K. M.
& Ubachs, W.
Science 339, 46–48, (2013).*

Abstract

The standard model of physics is built on the fundamental constants of nature, but it does not provide an explanation for their values, nor requires their constancy over space and time. Here we set a limit on a possible cosmological variation of the proton-to-electron mass ratio μ by comparing transitions in methanol observed in the early universe with those measured in the laboratory. From radio-astronomical observations of PKS1830–211, we deduced a constraint of $\Delta\mu/\mu = (0.0 \pm 1.0) \times 10^{-7}$ at redshift $z = 0.89$, corresponding to a look-back time of 7 billion years.

The standard model of particle physics, the theory describing symmetries and forces of nature at the deepest level, does not provide an intrinsic explanation for the values of the fundamental coupling constants, nor does it prohibit that the fundamental constants depend on time and space. In contrast, Einsteins equivalence principle, a basic assumption of general relativity, assumes that the laws of nature, and hence the fundamental constants are independent of a local reference system. Some cosmological scenarios aimed at explaining the fine-tuning between fundamental constants sketch an evolving mechanism, where minimally varying constants are crucial for reaching the present state of complexity in the universe [178]. Theoretical approaches involving additional scalar fields have imposed bounds on varying constants through tests of the weak equivalence principle [19]. In the past decade the search for small variations of dimensionless fundamental constants over cosmological time scales has become an active experimental endeavor, in particular because the accurate measurement of spectral lines of atoms at high redshift have provided indication for a possible variation of the fine structure constant α , either temporally [33, 34] or spatially [35, 36].

A second dimensionless fundamental constant μ , representing the proton-to-electron mass ratio μ , probes the cosmological evolution of the nuclear versus the electroweak sector in the standard model. A search for a possible drift of μ has been made operational by comparing observations of spectral lines of the hydrogen molecule (H_2) in distant galaxies with accurate laboratory measurements [55]. These investigations, based on observations with the world's largest optical telescopes have yielded a limit at the level of $\Delta\mu/\mu < 10^{-5}$ for look-back times of 12 billion years [62, 63].

Inversion transitions of ammonia (NH_3) were found to be 100 times more sensitive to μ -variation than H_2 transitions [93, 95]. Astronomical observations of NH_3 , in the microwave or radio range of the electromagnetic spectrum, led to stringent $1\text{-}\sigma$ constraints at the level of $(1.0 \pm 4.7) \times 10^{-7}$ [96] and $(-3.5 \pm 1.2) \times 10^{-7}$ [132]. This has shifted the paradigm for probing μ -variation from optical to radio astronomy. Here we use the extreme sensitivity of methanol (CH_3OH) [99, 100] to probe the variation of the proton-to-electron mass ratio μ over cosmic time.

Methanol (Fig. 6.1a) is the simplest alcohol and consists of a hydroxyl group attached to a methyl group. The C-O bond is flexible, allowing the hydroxyl group to rotate with respect to the methyl group. This so-called internal rotation is strongly hindered by the repulsion between the hydrogen atoms of the different groups resulting in a three-fold barrier (Fig. 6.1b). If the barrier were infinitely high, the levels in the torsional well would be degenerate. Quantum mechanical tunneling through the barriers lifts this degeneracy, resulting in three levels that are labeled according to symmetry: A , $E1$ and $E2$ [179]. Because the symmetry of the nuclear wave function is preserved in

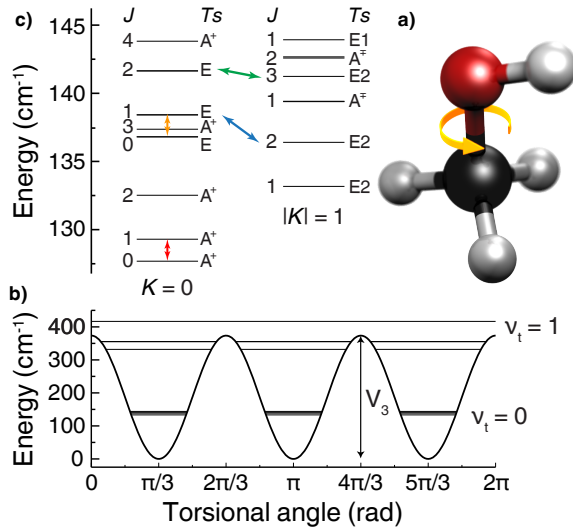


Figure 6.1: (a) Pictorial representation of the methanol molecule. (b) Potential energy as a function of the dihedral angle between the OH group and one of the CH bonds in the methyl group. V_3 denotes the barrier height. The horizontal lines represent the energy for the levels in the torsion-vibrational ground state, $\nu_t = 0$, and first excited state, $\nu_t = 1$. (c) Energy level structure of the torsion-rotation ground state of methanol. Each level is labeled according to its torsional symmetry Ts , total angular momentum J and its projection K on the molecule-fixed axis. The energy-level structure of methanol resembles that of a prolate symmetric top, with the difference that each K manifold is offset depending on its torsional symmetry. Levels of A - symmetry with $|K| > 0$ are split by the slight asymmetry of the molecule. Levels of $E1$ and $E2$ symmetry in the $K = 0$ manifold cannot be distinguished, and are labeled as E . The four transitions observed in this study are indicated by the four arrows. The transitions indicated by the red and orange arrows are pure rotational transitions and have a sensitivity coefficient of -1 . The transitions indicated by the green and blue arrows are mixed torsion-rotation transitions and have sensitivity coefficients of -32.8 and -7.4 , respectively.

optical transitions as well as in (nonreactive) collisions, the A and E levels of methanol can be regarded as belonging to two separate chemical species.

The sensitivity coefficient, K_μ , of a transition with frequency ν is defined by: $\Delta\nu/\nu = K_\mu \times \Delta\mu/\mu$. The frequency of pure rotational transitions, such as the transitions indicated by the red and orange arrow in Fig. 6.1c, are inversely pro-

portional to the reduced mass of methanol and hence to the proton-to-electron mass ratio. Consequently, these have sensitivity coefficients equal to -1 . The frequency of pure torsional transitions - which are not allowed in methanol - depends exponentially on the reduced moments of inertia of the methyl and hydroxyl groups and has a sensitivity coefficient of -2.5 . The sensitivity of mixed transitions, i.e. transitions in which both the internal and overall rotation state is changed, is strongly enhanced. The sensitivity coefficients for different transitions in methanol range from -42 to $+53$. These enhancements occur generally in every internal rotor molecule, but because of a number of favorable properties, the effect is exceptionally large in methanol [103].

Methanol is abundantly present in the universe and more than a 1000 lines have been recorded in our galaxy [181]. So far, searches for methanol absorption in far-distant galaxies have yielded detection only in the gravitational lens system PKS1830–211 [180]. A limit on $\Delta\mu/\mu$ [101] has been previously derived on the basis of two methanol lines. We present a comprehensive study of radio astronomical observations of four methanol lines in PKS1830–211, including the two previously observed, with improved signal-to-noise ratio.

The background source of this system, PKS1830–211, is a high redshift ($z = 2.507$) blazar, which is radio loud and time variable and is viewed as two spot-like features and an Einstein ring, which result from gravitational lensing by the intervening face-on spiral galaxy [182, 183]. The redshift of the main molecular absorptions from the galaxy is $z = 0.88582$ [180, 184] corresponding to a look-back time of 7.0 billion years, or half the age of the universe.¹ More than 30 different molecular species were detected in the lensing galaxy of PKS1830–211 (see [180] and references therein). Molecular absorption is mostly detected toward one of the two blazar images (the south-western), whereas the other image (the north-eastern) shows weaker and fewer molecular lines at a slightly different redshift but stronger neutral hydrogen absorption (see e.g., [180, 185]).

The CH_3OH lines were recorded with the 100-m single-dish Effelsberg radio telescope, using the 5-, 1.3-, and 1-cm receivers. Preliminary detections were performed during the course of 2011, and subsequently systematic observations were performed in a narrow time slot. The data were registered onto a local standard of rest velocity scale, which was centered at $z = 0.88582$. The two blazar images and the Einstein ring are unresolved and PKS1830–211 is effectively treated as a point source, which is an assumption underlying the present study.

The recorded spectra are shown in Fig. 6.2. For a single transition, the spectra taken on various days were averaged together, weighting the individual scans by their integration time. The lines were calibrated by the total contin-

¹Adopting a standard Λ -cosmology with $H_0 = 73 \text{ km s}^{-1} \text{ Mpc}^{-1}$, $\Omega_m = 0.28$, $\Omega_\Lambda = 0.72$.

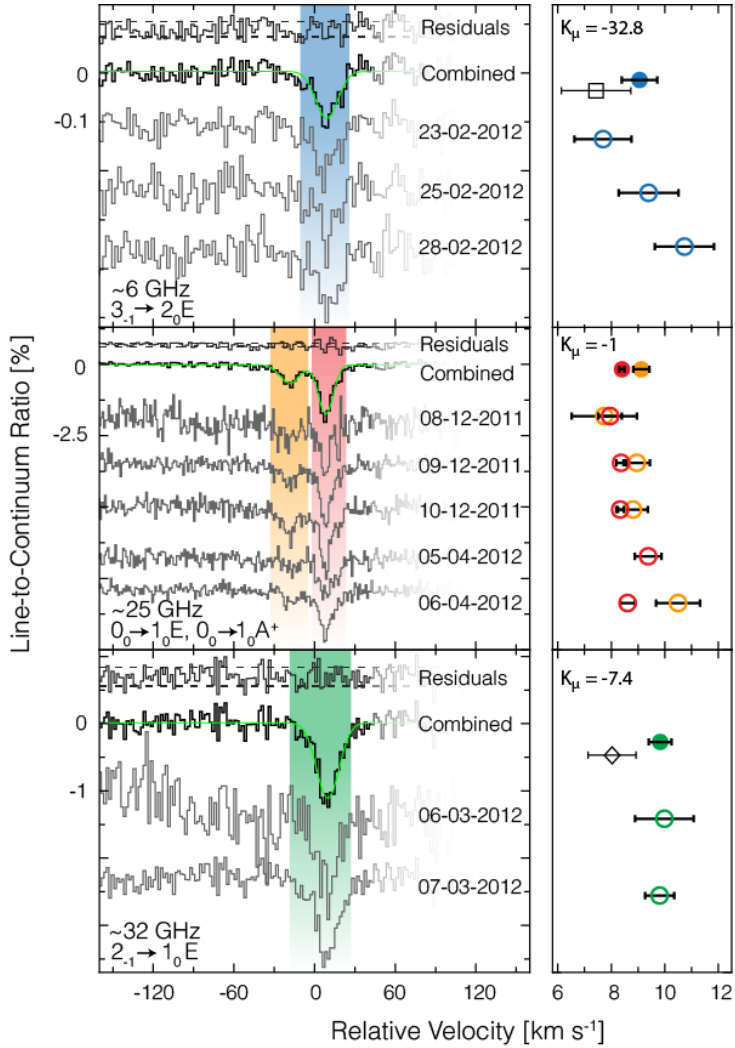


Figure 6.2: Methanol absorption lines on a Local Standard of Rest velocity scale relative to $z = 0.88582$, observed towards PKS1830–211. The transitions and their approximate observed frequencies are indicated in each panel. The coloring of corresponding transitions matches that of Fig. 6.1. *Continued on next page.*

Figure 6.2: *Continued from previous page.* The top spectrum in each panel is a time-weighted average of the individual spectra, which are displayed below the combined one. For each spectrum, the position of a fitted Gaussian (depicted as light green curves) is shown in the graph at the right. Residuals are shown at the top of each combined spectrum with dashed lines indicating $\pm 1\sigma$ offsets. In the case of ~ 25 GHz observations, two proximate methanol transitions were recorded. They are separated by 27.494 km/s; the fitted positions of the weaker line are corrected to bring the measurements on a common scale. The lines are calibrated by the total continuum. The black square (upper panel) and the black diamond (lower panel) represent the single line observations from Ellingsen et al. [101] and Muller et al. [180], respectively. The line positions, originally reported on a heliocentric velocity scale, were transformed to the Local Standard of Rest scale via $V_{\text{LSR}} - V_{\text{HEL}} = 12.432$ km/s.

uum so that their strength is expressed as line-to-continuum flux density ratio. The profiles, devoid of underlying structure, were fitted as a single Gaussian (Table 6.1). The accuracy of the position measurements is at the level of 1 to 4% of the line width. The velocities between different transitions are interrelated via $V/c = -K_{\mu} \times \Delta\mu/\mu$, where c is the speed of light, and $\Delta\mu/\mu$ represents the deviation from the current laboratory value of μ , defined so that a positive sign indicates a larger μ in the high-redshift absorbing galaxy (i.e. $\Delta\mu = \mu_z - \mu_{\text{lab}}$). Therefore, to determine the fractional change in μ , the peak positions of the four transitions are plotted (in V/c) versus K_{μ} , and a (dashed) line is fitted to the data (Fig. 6.3). Because the A and E levels of methanol can be regarded as belonging to two separate species, the data were analyzed in two different ways: first, only the three transitions from E levels were fitted, then the A transition was added to the sample. The analysis of the E transitions results in $\Delta\mu/\mu = (-0.1 \pm 7.6) \times 10^{-8}$, which is consistent with a non-varying μ at the level of 1.5×10^{-7} (95% confidence level). The reduced chi-squared, χ_{ν}^2 , which is a measure of the quality of the fit, is ~ 2.0 . The fit on all four transitions has a much larger χ_{ν}^2 of 6.4, which might be attributed to segregation issues (see below), and it delivers $\Delta\mu/\mu = (11.0 \pm 6.8) \times 10^{-8}$.

The upper limit derived here is statistically more constraining than those derived in previous tests in the radio-domain [127, 96, 132, 180, 101]. Moreover, compared to the methods used in previous studies, the methanol method is more robust against systematic effects. In particular, it is much less sensitive to the assumption that all absorbing species reside in the same physical location and hence are at the same redshift. Spatial segregation of different absorbers may mimic or hide a variation of μ . This is the limiting systematic error for tests based on the comparison between different molecular species,

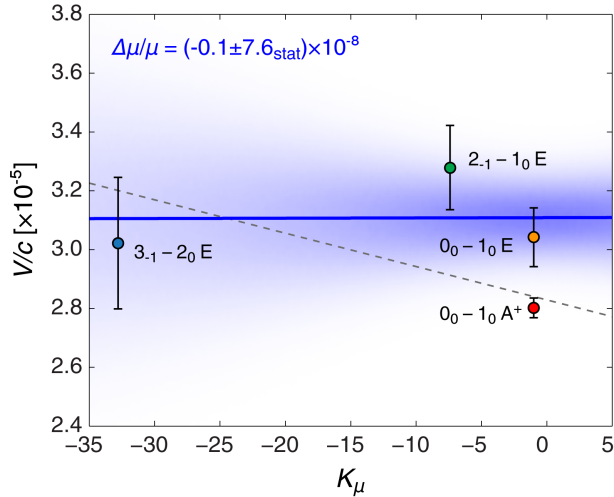


Figure 6.3: The positions of the four observed methanol lines (represented by V/c with respect to $z = 0.88582$) are plotted versus their sensitivity coefficients, K_μ . The bold blue straight line represents the fiducial result of a fit to the E type lines, while the dashed line represents a fit to all four lines. A positive slope of the fitted line implies that μ had a smaller value in the early universe than is measured in the laboratory. The blue-shaded surface is a density plot of simulated data points from the blue fitted line and reflects the confidence bands of the fit. Color-coding of the data points is the same as in Fig. 6.1 and 6.2.

such as the comparison of ammonia with various rotational lines in HCO^+ , HCN , CS and so forth [127, 96, 132]. The molecular survey in PKS1830–211 suggests that segregation effects are prominent among different species [180]. For instance, a single methanol line was found to be displaced from the average absorption velocity by more than 3 km/s [180]. Our test is based exclusively on a single molecular species. However, as discussed above, the E and A type methanol should be considered as different species and thus may undergo spatial segregation effects. In the combined spectrum the $0_0 - 1_0 A^+$ and $0_0 - 1_0 E$ transitions, falling in close proximity in a single scan of the receiver, are separated by 0.72 ± 0.32 km/s. Moreover, the linewidths of the E lines are markedly larger than that of the A line (Table 6.1). Because this is suggestive of a spatial segregation of the E and A symmetry methanol molecules, we adopt a fiducial limit on $\Delta\mu/\mu$ from the fit of only E transitions.

Another source of systematic error is the known variability of the lensed object PKS1830–211. The absorption strength of radio lines was found to vary strongly, by a factor of > 6 in a time span of 3 years, and this was ascribed to the intensity changes in the background continuum source [186]. This phenomenon might cause a varying alignment through parts of the absorbing spiral and therewith absorption through varying Doppler components over time. Hence this variability may affect the derivation of a μ -constraint from radio-observations. For this reason we adopted a measurement strategy to explicitly address the source variability issue. Spectra of the anchor lines (the middle panel in Fig. 6.2) were recorded in December 2011 and April 2012, whereas the two strongly shifting lines have been observed in-between in February and March 2012.² The strong ($0_0 - 1_0A^+$) line in the combined spectrum from December 2011 is positioned at 8.32 ± 0.10 km/s, and at 8.80 ± 0.24 km/s in the spectrum from April 2012. The difference between them is 0.48 ± 0.26 km/s, possibly indicative of a small systematic shift due to variability. We have assessed this possible systematic effect as caused by time variability in two models and have chosen the one producing the largest uncertainty ($\Delta\mu/\mu$ of 7.0×10^{-8}) to give a conservative estimate. Thus, we obtain a limit on varying μ to be $\Delta\mu/\mu = (-0.1 \pm 7.6_{\text{stat}} \pm 7.0_{\text{sys}}) \times 10^{-8}$ or, if the statistical and systematic uncertainties are added in quadrature, a limit of $\Delta\mu/\mu = (0.0 \pm 1.0) \times 10^{-7}$.

Acknowledgments

This work is supported by the FOM-program ‘Broken Mirrors & Drifting Constants’. H. L. B. acknowledges support from NWO via a VIDI grant and by the ERC via a Starting Grant. We thank the staff of the Effelsberg radio telescope for their hospitality and support.

²Each line required a change of receiver, for which reason the time intervals could not be shorter.

Table 6.1: A summary of the relevant parameters and results. Laboratory data: lower and upper energy level quantum numbers; laboratory frequencies, ν , of the four relevant methanol absorption lines; and their uncertainties, fractional uncertainties, and uncertainties in terms of Doppler shift, ΔV_D , in km/s. Calculations: the sensitivity coefficients, K_μ . Observations: the measured local standard of rest velocities of the lines (relative to $z = 0.88582$) and the line widths with their $1-\sigma$ uncertainties. Assuming a molecular hydrogen density of $2 \times 10^3 \text{ cm}^{-3}$ and a kinetic temperature of 80 K [96, 187], $2-\sigma$ or FWHM/ $\sqrt{2ln2}$ linewidths as fitted to observations and a $T_{CMB} = 2.728(1+z) = 5.145 \text{ K}$ for the temperature of the cosmic microwave background (CMB) radiation at $z = 0.88582$, the optical depths τ yield a total column density of $2.0 \times 10^{14} \text{ cm}^2$ from a large velocity gradient radiative transfer model [188].

Line	ν (GHz)	$\Delta\nu/\nu$	ΔV_D (km/s)	Ref.	K_μ	Position (km/s)	Width (km/s)	τ
$J_{K''\nu}^u - J_{K''\nu}^l, T_s$								
$3_{-1} - 2_0 E$	12.178597(4)	3×10^{-7}	0.1	[189]	-32.8	9.06 ± 0.67	16.4 ± 1.4	0.00024
$0_0 - 1_0 A^+$	48.3724558(7)	2×10^{-8}	0.006	[190]	-1	8.40 ± 0.10	10.8 ± 0.2	0.045
$0_0 - 1_0 E$	48.376892(10)	2×10^{-7}	0.06	[191]	-1	9.12 ± 0.30	14.6 ± 0.6	0.016
$2_{-1} - 1_0 E$	60.531489(10)	2×10^{-7}	0.06	[191]	-7.4	9.83 ± 0.43	17.0 ± 0.9	0.028

Robust constraint on a drifting proton-to-electron mass ratio at $z = 0.89$ from methanol observation at three radio telescopes

Bagdonaite, J., Dapra, M., Jansen, P., Bethlem, H. L., Ubachs, W., Muller, S., Henkel, C. & Menten, K. M.
Phys. Rev. Lett. **111**, 231101 (2013).

Abstract

A limit on a possible cosmological variation of the proton-to-electron mass ratio μ is derived from methanol (CH_3OH) absorption lines in the benchmark PKS1830–211 lensing galaxy at redshift $z = 0.89$ observed with the Effelsberg 100-m radio telescope, the Institut de Radio Astronomie Millimétrique 30-m telescope, and the Atacama Large Millimeter/submillimeter Array. Ten different absorption lines of CH_3OH covering a wide range of sensitivity coefficients K_μ are used to derive a purely statistical $1\text{-}\sigma$ constraint of $\Delta\mu/\mu = (1.5 \pm 1.5) \times 10^{-7}$ for a lookback time of 7.5 billion years. Systematic effects of chemical segregation, excitation temperature, frequency dependence and time variability of the background source are quantified. A multi-dimensional linear regression analysis leads to a robust constraint of $\Delta\mu/\mu = (-1.0 \pm 0.8_{\text{stat}} \pm 1.0_{\text{sys}}) \times 10^{-7}$.

The fact that the strengths of the fundamental forces of nature are not fixed by the Standard Model of physics leaves space for the hypothesis of coupling constants varying over time and space. Such a constant is the dimensionless proton-to-electron mass ratio $\mu = m_p/m_e$, representing the ratio of the strong force to the electroweak scale [7]. Effects of a time-varying μ may be probed through the measurement of molecular line spectra in various cosmological epochs. The spectrum of molecular hydrogen, H_2 , the most abundant molecule in the universe, can be investigated with large optical telescopes [56, 62, 63, 130]. The sensitivity coefficient K_μ , defined via

$$\frac{\Delta\nu}{\nu} = K_\mu \frac{\Delta\mu}{\mu} \quad (7.1)$$

for the H_2 spectral lines is only of the order of 0.05 [44]. For this reason the μ constraint resulting from H_2 data is not better than $\Delta\mu/\mu < 10^{-5}$.

Transitions of some other molecules in the radio part of the electromagnetic spectrum exhibit larger sensitivities to a varying μ . Inversion transitions of ammonia (NH_3), with $K_\mu = -4.46$, have been applied to produce $1\text{-}\sigma$ constraints at the level of $\Delta\mu/\mu = (1.0 \pm 4.7) \times 10^{-7}$ in the object PKS1830–211 at $z = 0.89$ [96] and $(-3.5 \pm 1.2) \times 10^{-7}$ in the object B0218+357 at $z = 0.68$ [132]. In the μ -variation analysis the strongly shifting NH_3 lines must be compared with non-shifting anchor lines belonging to different species, such as HCO^+ and HC_3N . This may give rise to systematic effects on the result for $\Delta\mu/\mu$ due to chemical segregation, *i.e.* to a non-homogeneous spatial distribution of the various molecular species along the line-of-sight.

It was recently pointed out that the interplay between the internal and overall rotation in the methanol molecule (CH_3OH) results in specific transitions having an enhanced sensitivity for a possible drift in μ [99, 100]. Some of these transitions involve low lying rotational energy levels populated at the low temperatures characterizing the bulk of the interstellar molecular gas. The spread in K_μ coefficients for methanol lines provides the unique opportunity of deriving a tight constraint on μ from a single molecular species, therewith avoiding chemical segregation issues. Methanol has recently been observed in a gravitationally lensing galaxy (at $z = 0.89$, corresponding to a lookback time of 7.5 billion years) toward the south-western (SW) image of the background blazar PKS1830–211 [180, 101]. In a preliminary investigation based on a small sample of four methanol transitions a $1\text{-}\sigma$ limit of $\Delta\mu/\mu$ at 1×10^{-7} was derived [20], with an indication of a spatial differentiation of the *E*- and *A*-type symmetry species. Here, we present an extended study of μ variation based on 17 measurements of ten different absorption lines of CH_3OH allowing for a quantitative analysis of previously unaddressed underlying systematic effects. This analysis leads to a similar constraint as the one found in [20], but the robustness of this constraint is greatly improved.

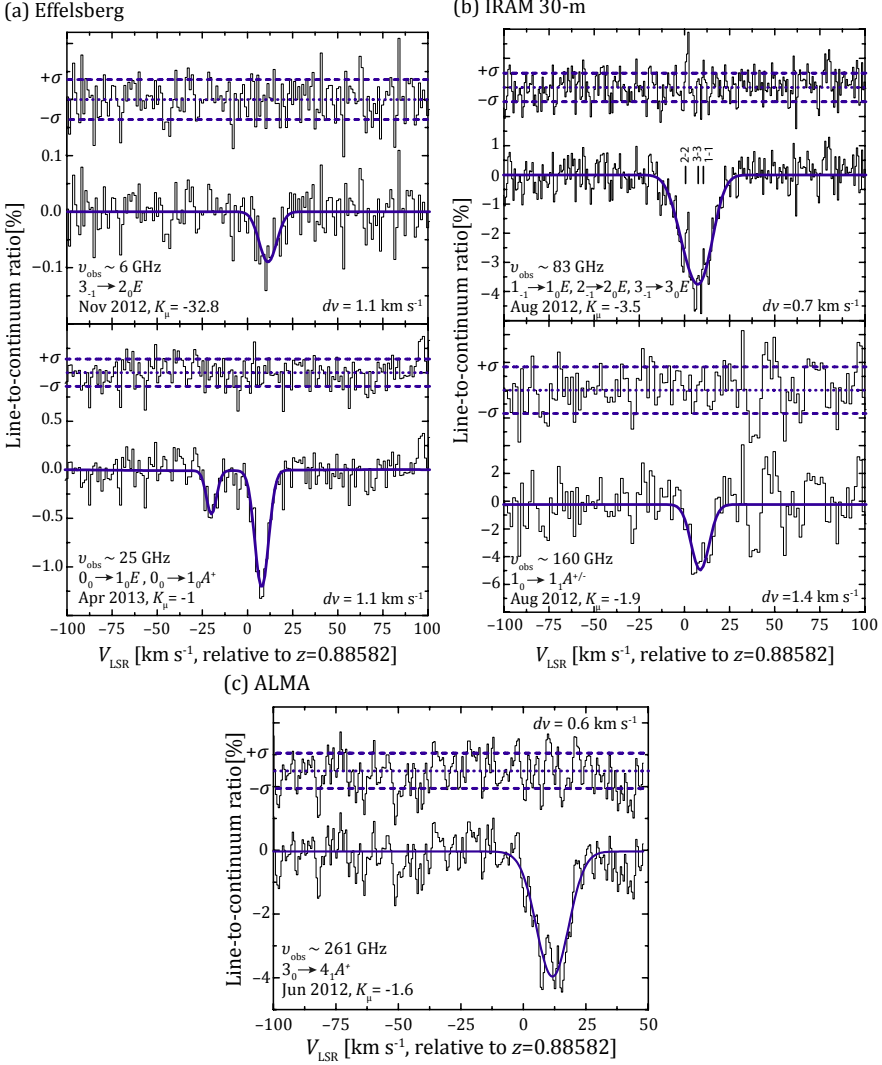


Figure 7.1: Some of the observed methanol transitions toward PKS1830–211 with their approximate observed frequencies ν_{obs} , observation epoch, sensitivity coefficients K_{μ} , and channel spacings dv indicated in each panel for recordings at (a) Effelsberg radio telescope, (b) IRAM 30-m telescope, (c) ALMA array. The intensity is normalized to the total continuum flux, except for (c) where the SW image could be observed exclusively. Gaussian fits to the absorption profiles are displayed in dark blue with residuals shown at the top of each panel.

Methanol absorption spectra were recorded using three different radio telescopes covering a range of 6–261 GHz. The CH₃OH lines in the low-frequency range (detected frequencies < 35 GHz), previously observed in the time slot Dec. 2011–Apr. 2012 [20], were reobserved with the 100-m single-dish Effelsberg radio telescope of the Max-Planck-Institute für Radioastronomie (see Table 7.1). Spectra of the new observations in fall 2012 and spring 2013 are shown in Fig. 7.1(a). The absorption profiles of individual transitions were fitted to single Gaussians, and the line positions and widths were determined on a Local Standard of Rest (LSR) velocity scale, which was centered at $z = 0.88582$.

The Institute de Radio Astronomie Millimétrique (IRAM) 30-m single dish telescope at Pico Veleta (Spain) was used to detect methanol lines in the range 80–165 GHz, using the EMIR receiver in observations during 22–27 August 2012. Fig. 7.1(b) shows the overlapping components of the $1_{-1} - 1_0E$, $2_{-1} - 2_0E$ and $3_{-1} - 3_0E$ transitions at a detection frequency of 83.3 GHz. A fit was performed assuming that relative intensities between the three components are proportional to their expected optical depths. The RADEX radiative transfer model [192] was used to estimate the relative intensities. Also the relative positions of the components were fixed based on the laboratory measurements, and the widths were assumed to be the same. The uncertainty of the combined line position is estimated by varying the relative strengths of the three lines by 10–20% with regard to the RADEX prediction. Also shown in Fig. 7.1 is a recording of the $1_0 - 1_1A^{+/-}$ line at a detection frequency of 160 GHz. In addition the weak $3_0 - 2_1A^+$ line at $\nu_{\text{obs}} \sim 83.0$ GHz was observed with the IRAM 30-m.

An observation of the $3_0 - 4_1A^+$ CH₃OH transition at a frequency of 261 GHz was conducted in June 2012 with the Atacama Large Millimeter/submillimeter Array (ALMA, 20 dishes, 12 m in diameter each; see Fig. 7.1(c)). The angular resolution of the ALMA observations (~ 0.6 arcsec) made it possible to obtain a spectrum toward the south-western image only.

Table 7.1 contains results from the fitted spectra of all methanol lines observed, as well as laboratory frequencies [189, 190, 191, 193, 194] with their uncertainties, and the calculated K_μ coefficients [99]. The quoted optical depths τ are related to the measured absorption line intensities I_ν via $\tau = -\ln(1 - I_\nu/f_c I_{bg})$ where I_{bg} is the total continuum intensity and f_c is the continuum source covering factor. For unresolved single-dish observations, we adopt $f_c = 0.4$ [96] for the SW sightline of PKS1830–211.

7. METHANOL OBSERVATION AT THREE RADIO TELESCOPES

Table 7.1: Summary of the observed methanol lines in PKS1830–211. Listed are the lower and upper energy level quantum numbers, laboratory or rest frequencies ν_{lab} and corresponding uncertainties, fractional uncertainties $\Delta\nu/\nu$, uncertainties in terms of Doppler shift, Δv_D , and corresponding frequencies at redshift $z = 0.88582$. K_μ refers to the sensitivity coefficients (see Eq. 7.1). Fitted line positions V_{LSR} are stated with respect to the Local Standard of Rest (centered at $z = 0.88582$). Uncertainties in position and FWHM width are obtained from Gaussian fits (1 σ). Optical depths τ are fitted from the spectra. In the last column the instrument and the observation period is mentioned. The following abbreviations are used: E. – the Effelsberg 100-m, I. – the 30-m radio telescope at the Pico Veleta, AT. – ATCA, AL. – ALMA, date format – mmmmyy.

Transition	ν_{lab} (GHz)	$\Delta\nu/\nu$	Δv_D (km s $^{-1}$)	$\nu_{z=0.88582}$ (GHz)	K_μ	V_{LSR} (km s $^{-1}$)	Width (km s $^{-1}$)	τ	Obs.
3 $_1$ –2 $_0E$	12.178597(4) ^a	3×10^{-7}	0.1	6.457985	–32.8	9.1 \pm 0.7	18.2 \pm 1.5	0.0024	E. Feb12 ^h
						10.7 \pm 0.7	12.0 \pm 1.2	0.002	E. Nov12
						12.6 \pm 2.0	19.9 \pm 4.5	0.002	E. May13
						7.4 \pm 1.3 ^f	17.0 \pm 2.9 ^f	0.005 ^f	AT. Nov11
0 $_0$ –1 $_0A^+$	48.3724558(7) ^b	2×10^{-8}	0.006	25.6506219	–1.0	8.3 \pm 0.1	12.0 \pm 0.2	0.045	E. Dec11 ^h
						8.8 \pm 0.2	14.8 \pm 0.6	0.03	E. Apr12 ^h
						8.7 \pm 0.2	8.5 \pm 0.6	0.03	E. Mar13
						7.8 \pm 0.3	9.0 \pm 0.7	0.03	E. Apr13
0 $_0$ –1 $_0E$	48.376892(10) ^c	2×10^{-7}	0.06	25.652974	–1.0	8.9 \pm 0.3	18.5 \pm 0.8	0.016	E. Dec11 ^h
						10.4 \pm 0.7	12.5 \pm 1.6	0.011	E. Apr12 ^h
						7.6 \pm 0.6	6.7 \pm 1.3	0.013	E. Apr13
2 $_1$ –1 $_0E$	60.531489(10) ^c	2×10^{-7}	0.06	32.098233	–7.4	9.8 \pm 0.4	20.0 \pm 1.1	0.028	E. Mar12 ^h
						8.0 \pm 0.9 ^f	17.2 \pm 2.0 ^f	0.020 ^f	AT. Sep09
3 $_0$ –2 $_1A^+$	156.602413(10) ^c	6×10^{-8}	0.02	83.042079	–2.7	9.5 \pm 1.5	11.1 \pm 3.8	0.019	I. Aug12
1 $_1$ –1 $_0E$	157.270851(10) ^c	6×10^{-8}	0.02	83.396534	–3.5	10.5 \pm 0.7 ^g	15.4 \pm 0.4 ^g	0.08	I. Aug12
2 $_1$ –2 $_0E$	157.276058(10) ^c	6×10^{-8}	0.02	83.399295	–3.5	"	"	"	I. Aug12
3 $_1$ –3 $_0E$	157.272369(10) ^c	6×10^{-8}	0.02	83.397339	–3.5	"	"	"	I. Aug12

Continued on next page.

Table 7.1 – *continued from previous page.*

Transition	ν_{Lab} (GHz)	$\Delta\nu/\nu$	Δv_D (km s^{-1})	$\nu_{z=0.88582}$ (GHz)	K_μ	V_{LSR} (km s^{-1})	Width (km s^{-1})	τ	Obs.
low-up									
$1_0-1_1 A^{+/-}$	303.36689(5) ^d	2×10^{-7}	0.06	160.86736	-1.9	8.8 ± 1.0	11.7 ± 2.4	0.12	1. Aug12
$3_0-4_1 A^+$	492.278713(50) ^e	1×10^{-7}	0.03	261.042259	-1.6	11.7 ± 0.3	15.1 ± 0.7	0.04	AL. Jun12

^aBreckenridge and Kukolich (1995) [189].

^bHeuvel and Dynammus (1973) [190].

^cMüller *et al.* [191].

^dSastry *et al.* [193].

^eHerbst *et al.* [194].

^fValues from [101], V_{HEL} is converted to V_{LSR} via $V_{\text{LSR}} - V_{\text{HEL}} = 12.432 \text{ km s}^{-1}$.

^gThree components fitted jointly (see text).

^hData used in [20] where the values of the widths were stated as $\text{FWHM}/\sqrt{2}m_2$.

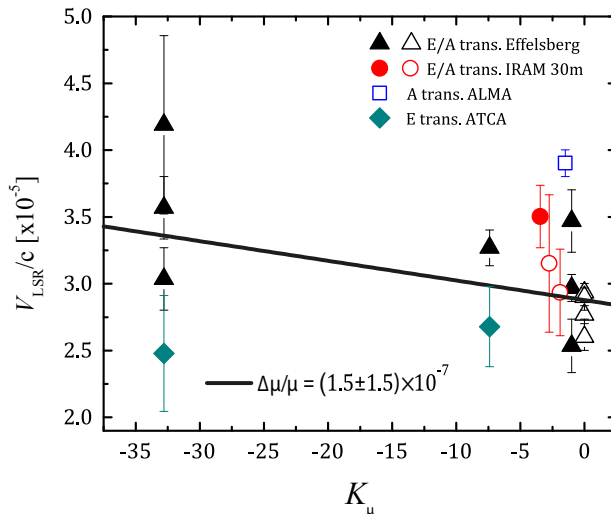


Figure 7.2: The positions of the ten observed methanol lines (represented by V_{LSR}/c with respect to $z = 0.88582$) are plotted versus their sensitivity coefficients, K_μ . Note that some transitions were observed multiple times, hence, 17 data points are displayed. The slope of a straight line fitted to the dataset represents $-\Delta\mu/\mu$. The A transitions observed at Effelsberg are offset from $K_\mu = -1$ to 0 for clarity.

The RADEX code allows us to derive a column density of methanol from the present set of measurements. Assuming a molecular hydrogen density of $2 \times 10^3 \text{ cm}^{-3}$ and a kinetic temperature of 80 K (values discussed in [96],[187], and [195]), FWHM linewidths and optical depths as fitted to observations, and a $T_{\text{CMB}} = 2.728(1+z) = 5.145 \text{ K}$ for the temperature of the cosmic microwave background radiation at $z = 0.88582$, this yields a total column density of $1.6 \times 10^{14} \text{ cm}^{-2}$ (adding E and A type methanol column densities).

All the detected methanol transitions have been included in the analysis. In addition, Table 7.1 includes two data points resulting from observations with the Australia Telescope Compact Array (ATCA), presented in the literature: the $2_{-1}-1_0E$ transition in [180] observed in September 2009, and the $3_{-1}-2_0E$ transition in [101] observed in November 2011. We adopt line positions from the latter work.

The velocities between different transitions are interrelated via $V/c = -K_\mu \times \Delta\mu/\mu$, where c is the speed of light (also see Eq. 7.1). The error bars in the velocity positions reflect the statistical uncertainties from Gaussian profile fitting to the observed spectra. The uncertainty in the laboratory frequencies,

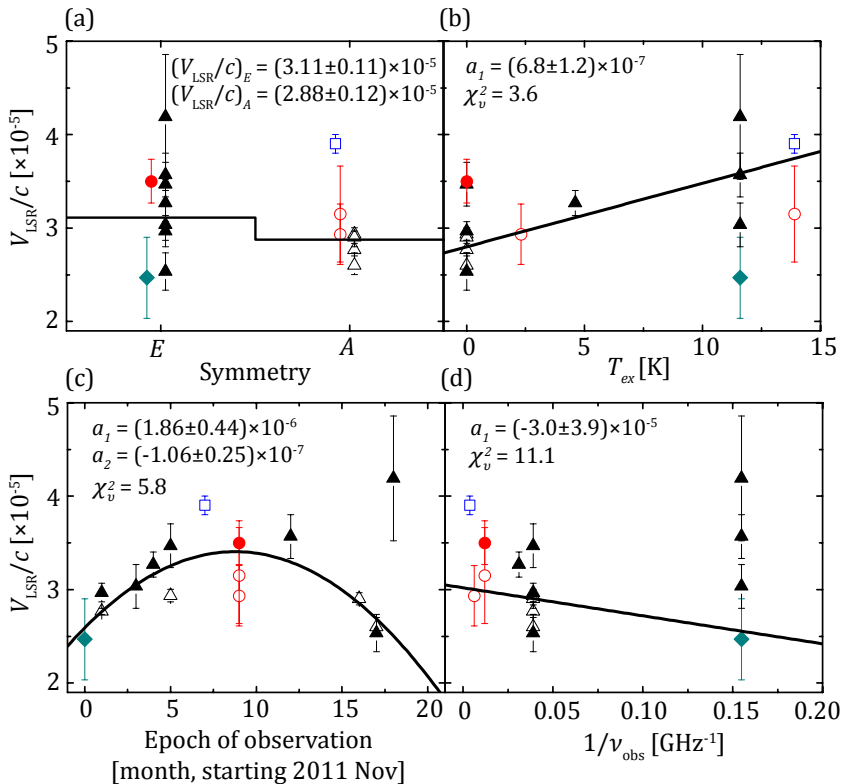


Figure 7.3: The positions of 16 observed methanol absorptions (leaving out the data point measured in 2009) as a function of various parameters: (a) symmetry, (b) excitation temperature of the lower level, (c) epoch of observation, (d) observed frequency. The color coding is the same as in Fig. 7.2. The solid lines show a fit using a linear or quadratic function of form $y = a_0 + a_1x + a_2x^2$.

expressed on a velocity scale in Table 7.1 with Δv_{D} , is small ($<14\%$) compared to the uncertainty obtained from the astrophysical spectra and is treated as negligible. The uncertainties arising in the calibration of the frequency scale at the four observatories is of the order of 20 m s^{-1} or less [196, 197]. The result of the statistical analysis deducing $\Delta\mu/\mu$ is shown in Fig. 7.2. A fit to the 17 data points delivers a constraint of $\Delta\mu/\mu = (1.5 \pm 1.5) \times 10^{-7}$ with a reduced $\chi^2_{\nu} = 10.2$, where the number of degrees of freedom, ν , is 15. The large value of the goodness-of-fit measure χ^2_{ν} indicates that the spread of the data is larger than expected from their errors. As a consequence, the addition of new data to our previous set [20] did not lead to an expected improvement of the con-

straint. Assuming we do not underestimate the errors from the observations, the rather large value of χ_ν^2 suggests an underlying systematic effect that is not taken into account. In the following we address possible candidates.

Chemical segregation. Spatial segregation of molecular species within an absorbing galaxy may mimic or hide a variation of μ . Since we rely on a single molecular species chemical segregation cannot be an issue, however, it may be possible that E and A type methanol are displaced spatially as suggested in [20]. In panel (a) of Fig. 7.3, the data are grouped by their symmetry. The averages of the A and E transitions agree within their uncertainties. Furthermore, a two-dimensional linear regression (LR) analysis with K_μ and E/A symmetry as independent variables results in an increase of χ_ν^2 , if compared to a fit with K_μ alone, thereby ruling out a possible E/A segregation. This new result of the extended study implies that all data pertaining to methanol can be included in a μ variation analysis.

Temperature dependence. The spread in the line positions might be ascribed to an inhomogeneous temperature distribution in the absorbing cloud. In panel (b) of Fig. 7.3, the V_{LSR}/c values are plotted as a function of the excitation energy of the lower level. The solid line shows a linear fit to the data, indicating a correlation between the measured line positions and the excitation energy. When we include the excitation energy as an independent variable in a two-dimensional LR analysis, we find a constraint of $\Delta\mu/\mu = (-1.3 \pm 1.0) \times 10^{-7}$ with $\chi_\nu^2 = 3.4$ where $\nu = 14$. The obtained limit of a time variation of $\Delta\mu/\mu$ changes only marginally when effects of the excitation energy are included, i.e., the $\Delta\mu/\mu$ is not strongly correlated to the excitation energy in our data set, however, the χ_ν^2 is significantly reduced.

Time variability of the background source. The strength of radio absorption lines towards the SW image was found to vary by a factor of ~ 2 in a time span of three years, which was ascribed to the intensity changes in the background continuum source [186]. In particular, observations of an optically thick HCO^+ transition have shown an absorption profile, composed of several components, evolving with time. This phenomenon was explained by morphological changes in the background blazar. Thus, comparing line profiles from various time periods may lead to potential errors in line positions, especially if the velocity structure is underrepresented by the fitting [95]. In panel (c) of Fig. 7.3 we show V_{LSR}/c as a function of observation epoch. An indication of an oscillating behaviour can be found but as we observe (less than) one period of this oscillation we choose to fit a quadratic time dependence instead of a sinusoidal one. A two-dimensional LR analysis with the observation epoch and K_μ as independent variables results in $\Delta\mu/\mu = (0.7 \pm 1.1) \times 10^{-7}$ with $\chi_\nu^2 = 5.6$ with $\nu = 12$. Again, although our data show a dependence on observation epoch, this does not change the resulting limit on a time variation of $\Delta\mu/\mu$ if compared to the one from a K_μ -only fit. In a three-dimensional

analysis where both the time variability and the temperature dependence are taken into account, a constraint of $\Delta\mu/\mu = (-1.0 \pm 0.8) \times 10^{-7}$ is delivered with $\chi_\nu^2 = 2.4$, where $\nu = 11$.

Frequency dependence. Previous studies have shown that the size of the south western image of the PKS1830–211 background blazar changes with frequency [198] and it exhibits a chromatic substructure, i.e. a different apparent position of the core at different frequencies, known as a core-shift effect. In particular, the angular separation $\Delta\theta$ of two sightlines at observed frequencies ν_1 and ν_2 is estimated to be $\Delta\theta = \Omega(1/\nu_1 - 1/\nu_2)$ where $\Omega \sim 0.8$ mas GHz [199]. No correlation is found between V_{LSR}/c and $1/\nu$ (Fig. 7.3(d)) but note that the sensitivity of the lines used in our study follow a $1/\nu$ dependence [99], hence, K_μ and $1/\nu$ are correlated and cannot be fitted simultaneously. According to [199], the core-shift effect in the PKS1830–211 system may introduce a shift of ~ 1 km s $^{-1}$ between lines at $\nu_{\text{obs}} \sim 6$ GHz and higher frequencies, which would translate into an uncertainty in $\Delta\mu/\mu$ of 1×10^{-7} . As it is not possible to estimate the size of this effect based on the current data set, we adopt the latter value as a systematic uncertainty of $\Delta\mu/\mu$. In order to constrain the core-shift effect based on methanol only it would be desirable to add low frequency methanol absorption that have positive or small K_μ . Attempts to observe the $3_0 - 4_{-1}E$ transition at $\nu_{\text{obs}} \sim 19.2$ GHz with $K_\mu = +9.7$ using the Effelsberg telescope were unsuccessful.

In conclusion, we present a test on a possible variation of μ at more than half of the age of the universe using methanol absorption lines detected in a foreground galaxy towards the PKS1830–211 blazar. The methanol method, being the most sensitive probe for time-variations of μ , can only be applied to this object as it is the only place in the far distant universe where the methanol molecule has been detected so far. For this reason we focused all efforts on observing this object and used different telescopes to collect a total of 17 data points for ten different absorption lines from which a statistical constraint of $\Delta\mu/\mu = (1.5 \pm 1.5) \times 10^{-7}$ is derived. The large data set greatly enhances the understanding of previously unaddressed systematic effects and allows for a robust analysis. The suggested systematic on E/A chemical segregation [20] has now been discarded. The analysis reveals that effects pertaining to temperature inhomogeneity of the absorbing cloud and time variability of the background source result in a larger scatter than expected from the error of the individual transitions. By including the underlying systematic effects as independent variables in a multi-dimensional linear regression analysis, we obtain $\Delta\mu/\mu = (-1.0 \pm 0.8_{\text{stat}} \pm 1.0_{\text{sys}}) \times 10^{-7}$. Translated into a rate of change this corresponds to $\dot{\mu}/\mu < 2 \times 10^{-17}$ yr $^{-1}$, which is equally constraining as the bound on a varying constant obtained with the best optical clocks in laboratory experiments [29].

Acknowledgments

This work is supported by the FOM-program “Broken Mirrors & Drifting Constants” and by FOM-projects 10PR2793 and 12PR2972. W.U. and P.J. acknowledge support from the Templeton Foundation, and H.L.B. acknowledges support from NWO via a VIDI grant. The research leading to these results has received funding from the European Commission Seventh Framework Programme (FP/2007-2013) under grant agreement No 283393 (RadioNet3). This paper makes use of the following ALMA data: ADS/JAO.ALMA #2011.0.00405.S. ALMA is a partnership of ESO (representing its member states), NSF (USA) and NINS (Japan), together with NRC (Canada) and NSC and ASIAA (Taiwan), in cooperation with the Republic of Chile. The Joint ALMA Observatory is operated by ESO, AUI/NRAO and NAOJ. On the basis of observations carried out with the IRAM 30-m telescope. IRAM is supported by INSU/CNRS (France), MPG (Germany) and IGN (Spain). Staff of the Effelsberg, IRAM 30-m and ALMA radio telescopes are thanked for their support.

Bibliography

- [1] Dirac, P. A. M. The cosmological constants. *Nature* **139**, 323 (1937).
- [2] Savedoff, M. P. Physical constants in extra-galactic nebulae. *Nature* **178**, 688–689 (1956).
- [3] Dzuba, V. A., Flambaum, V. V. & Webb, J. K. Space-time variation of physical constants and relativistic corrections in atoms. *Phys. Rev. Lett.* **82**, 888–891 (1999).
- [4] Dzuba, V. A., Flambaum, V. V. & Webb, J. K. Calculations of the relativistic effects in many-electron atoms and space-time variation of fundamental constants. *Phys. Rev. A* **59**, 230–237 (1999).
- [5] Thompson, R. I. The determination of the electron to proton inertial mass ratio via molecular transitions. *Astroph. Lett.* **16**, 3 (1975).
- [6] Sturm, S. *et al.* High-precision measurement of the atomic mass of the electron. *Nature* **506**, 467–470 (2014).
- [7] Flambaum, V. V., Leinweber, D. B., Thomas, A. W. & Young, R. D. Limits on variations of the quark masses, QCD scale, and fine structure constant. *Phys. Rev. D* **69**, 115006 (2004).
- [8] Duff, M. J. How fundamental are fundamental constants? *ArXiv e-prints* (2014). 1412.2040.
- [9] Ferreira, M. C., Frigola, O., Martins, C. J. A. P., Monteiro, A. M. R. V. L. & Solà, J. Consistency tests of the stability of fundamental couplings and unification scenarios. *Phys. Rev. D* **89**, 083011 (2014).
- [10] Uzan, J.-P. Varying constants, gravitation and cosmology. *Living Rev. Relat.* **14**, 2 (2011).
- [11] Kaluza, T. Zum Unitätsproblem der Physik. *Sitzungsberichte der Königlich Preussischen Akademie der Wissenschaften (Berlin)* 966–972 (1921).

- [12] Klein, O. Quantentheorie und fünfdimensionale Relativitätstheorie. *Zeitschrift für Physik* **37**, 895–906 (1926).
- [13] Schellekens, A. N. Life at the interface of particle physics and string theory. *Rev. Mod. Phys.* **85**, 1491–1540 (2013).
- [14] Lorén-Aguilar, P., García-Berro, E., Isern, J. & Kubyschin, Y. A. Time variation of G and α within models with extra dimensions. *Class. Quantum Grav.* **20**, 3885–3896 (2003).
- [15] Martins, C. J. A. P., Menegoni, E., Galli, S., Mangano, G. & Melchiorri, A. Varying couplings in the early universe: Correlated variations of α and G . *Phys. Rev. D* **82**, 023532 (2010).
- [16] Bekenstein, J. D. Fine-structure constant: Is it really a constant? *Phys. Rev. D* **25**, 1527–1539 (1982).
- [17] Sandvik, H. B., Barrow, J. D. & Magueijo, J. A simple cosmology with a varying fine structure constant. *Phys. Rev. Lett.* **88**, 031302 (2002).
- [18] Barrow, J., Sandvik, H. & Magueijo, J. Behavior of varying- α cosmologies. *Phys. Rev. D* **65**, 063504 (2002).
- [19] Barrow, J. D. & Magueijo, J. Cosmological constraints on a dynamical electron mass. *Phys. Rev. D* **72**, 043521 (2005).
- [20] Bagdonaite, J. *et al.* A stringent limit on a drifting proton-to-electron mass ratio from alcohol in the early universe. *Science* **339**, 46–48 (2013).
- [21] Bagdonaite, J. *et al.* Robust constraint on a drifting proton-to-electron mass ratio at $z = 0.89$ from methanol observation at three radio telescopes. *Phys. Rev. Lett.* **111**, 231101 (2013).
- [22] Khoury, J. & Weltman, A. Chameleon fields: Awaiting surprises for tests of gravity in space. *Phys. Rev. Lett.* **93**, 171104 (2004).
- [23] Flambaum, V. V. & Shuryak, E. V. How changing physical constants and violation of local position invariance may occur? In Danielewicz, P., Piecuch, P. & Zelevinsky, V. (eds.) *Nuclei and Mesoscopic Physics - WNMP 2007*, vol. 995 of *American Institute of Physics Conference Series*, 1–11 (2008).
- [24] Peik, E. Fundamental constants and units and the search for temporal variations. *Nucl. Phys. B (Proc. Suppl.)* **203**, 18–32 (2010).

-
- [25] Berengut, J. & Flambaum, V. Manifestations of a spatial variation of fundamental constants in atomic and nuclear clocks, Oklo, meteorites, and cosmological phenomena. *Europhys. Lett.* **97**, 20006 (2012).
- [26] Godun, R. *et al.* Frequency ratio of two optical clock transitions in $^{171}\text{Yb}^+$ and constraints on the time-variation of fundamental constants. *Phys. Rev. Lett.* **113**, 210801 (2014).
- [27] Huntemann, N. *et al.* Improved limit on a temporal variation of m_p/m_e from comparisons of Yb^+ and Cs atomic clocks. *Phys. Rev. Lett.* **113**, 210802 (2014).
- [28] Shelkovich, A., Butcher, R. J., Chardonnet, C. & Amy-Klein, A. Stability of the Proton-to-Electron Mass Ratio. *Phys. Rev. Lett.* **100**, 150801 (2008).
- [29] Rosenband, T. *et al.* Frequency ratio of Al^+ and Hg^+ single-ion optical clocks; Metrology at the 17th decimal place. *Science* **319**, 1808–1812 (2008).
- [30] Onegin, M. S., Yudkevich, M. S. & Gomin, E. A. Investigation of the fundamental constants stability based on the reactor Oklo burn-up analysis. *Mod. Phys. Lett. A* **27**, 50232 (2012).
- [31] Olive, K. A. *et al.* Constraints on the variations of the fundamental couplings. *Phys. Rev. D* **66**, 045022 (2002).
- [32] Bahcall, J. N. & Schmidt, M. Does the fine-structure constant vary with cosmic time? *Phys. Rev. Lett.* **19**, 1294 (1967).
- [33] Webb, J. K., Flambaum, V. V., Churchill, C. W., Drinkwater, M. J. & Barrow, J. D. Search for time variation of the fine structure constant. *Phys. Rev. Lett.* **82**, 884–887 (1999).
- [34] Murphy, M. T., Webb, J. K. & Flambaum, V. V. Further evidence for a variable fine-structure constant from Keck/HIRES QSO absorption spectra. *Mon. Not. Roy. Astron. Soc.* **345**, 609–638 (2003).
- [35] Webb, J. K. *et al.* Indications of a spatial variation of the fine structure constant. *Phys. Rev. Lett.* **107**, 191101 (2011).
- [36] King, J. A. *et al.* Spatial variation in the fine-structure constant - new results from VLT/UVES. *Mon. Not. Roy. Astron. Soc.* **422**, 3370–3414 (2012).

- [37] Rahmani, H. *et al.* The UVES large program for testing fundamental physics - II. Constraints on a change in μ towards quasar HE 0027–1836. *Mon. Not. Roy. Astron. Soc.* **435**, 861–878 (2013).
- [38] Whitmore, J. B. & Murphy, M. T. Impact of instrumental systematic errors on fine-structure constant measurements with quasar spectra. *Mon. Not. Roy. Astron. Soc.* **447**, 446–462 (2015).
- [39] Tzanavaris, P., Webb, J. K., Murphy, M. T., Flambaum, V. V. & Curran, S. J. Limits on variations in fundamental constants from 21-cm and ultraviolet quasar absorption lines. *Phys. Rev. Lett.* **95**, 041301 (2005).
- [40] Srianand, R., Gupta, N., Petitjean, P., Noterdaeme, P. & Ledoux, C. Detection of 21-cm, H₂ and deuterium absorption at $z > 3$ along the line of sight to J1337+3152. *Mon. Not. Roy. Astron. Soc.* **405**, 1888–1900 (2010).
- [41] Landau, S. J. & Scóccola, G. Constraints on variation in α and m_e from WMAP 7-year data. *Astron. Astrophys.* **517**, A62 (2010).
- [42] Dent, T., Stern, S. & Wetterich, C. Primordial nucleosynthesis as a probe of fundamental physics parameters. *Phys. Rev. D* **76**, 063513 (2007).
- [43] Meshkov, V. V., Stolyarov, A. V., Ivanchik, A. V. & Varshalovich, D. A. Ab initio nonadiabatic calculation of the sensitivity coefficients for the $X^1\Sigma_g^+ \rightarrow B^1\Sigma_u^+; C^1\Pi_u$ lines of H₂ to the proton-to-electron mass ratio. *Sov. J. Exp. Theor. Phys.* **83**, 303–307 (2006).
- [44] Ubachs, W., Buning, R., Eikema, K. S. E. & Reinhold, E. On a possible variation of the proton-to-electron mass ratio: H₂ spectra in the line of sight of high-redshift quasars and in the laboratory. *J. Mol. Spectrosc.* **241**, 155–179 (2007).
- [45] Bagdonaite, J. *et al.* Limits on a gravitational field dependence of the proton-electron mass ratio from H₂ in white dwarf stars. *Phys. Rev. Lett.* **113**, 123002 (2014).
- [46] Pâris, I. *et al.* The Sloan Digital Sky Survey quasar catalog: tenth data release. *Astron. Astrophys.* **563**, A54 (2014).
- [47] Balashev, S. A. *et al.* Molecular hydrogen absorption systems in Sloan Digital Sky Survey. *Mon. Not. Roy. Astron. Soc.* **440**, 225–239 (2014).
- [48] Jorgenson, R. A., Murphy, M. T., Thompson, R. & Carswell, R. F. The Magellan uniform survey of damped Lyman α systems - II. Paucity of strong molecular hydrogen absorption. *Mon. Not. Roy. Astron. Soc.* **443**, 2783–2800 (2014).

-
- [49] Ivanov, T. I. *et al.* HD as a probe for detecting mass variation on a cosmological time scale. *Phys. Rev. Lett.* **100**, 093007 (2008).
- [50] Salumbides, E. J. *et al.* CO A-X system for constraining cosmological drift of the proton-electron mass ratio. *Phys. Rev. A* **86**, 022510 (2012).
- [51] Hambly, N. C. *et al.* The SuperCOSMOS Sky Survey - I. Introduction and description. *Mon. Not. Roy. Astron. Soc.* **326**, 1279–1294 (2001).
- [52] Hewett, P. C. & Wild, V. Improved redshifts for SDSS quasar spectra. *Mon. Not. Roy. Astron. Soc.* **405**, 2302–2316 (2010).
- [53] Noterdaeme, P., Petitjean, P., Srianand, R., Ledoux, C. & López, S. The evolution of the cosmic microwave background temperature. Measurements of T_{CMB} at high redshift from carbon monoxide excitation. *Astron. Astrophys.* **526**, L7 (2011).
- [54] Noterdaeme, P. *et al.* Excitation mechanisms in newly discovered H₂-bearing damped Lyman- α clouds: systems with low molecular fractions. *Astron. Astrophys.* **474**, 393–407 (2007).
- [55] Reinhold, E. *et al.* Indication of a cosmological variation of the proton-electron mass ratio based on laboratory measurement and reanalysis of H₂ spectra. *Phys. Rev. Lett.* **96**, 151101 (2006).
- [56] King, J. A., Webb, J. K., Murphy, M. T. & Carswell, R. F. Stringent null constraint on cosmological evolution of the proton-to-electron mass ratio. *Phys. Rev. Lett.* **101**, 251304 (2008).
- [57] King, J. A., Murphy, M. T., Ubachs, W. & Webb, J. K. New constraint on cosmological variation of the proton-to-electron mass ratio from Q0528–250. *Mon. Not. Roy. Astron. Soc.* **417**, 3010–3024 (2011).
- [58] Noterdaeme, P., Ledoux, C., Petitjean, P. & Srianand, R. Molecular hydrogen in high-redshift damped Lyman- α systems: the VLT/UVES database. *Astron. Astrophys.* **481**, 327–336 (2008).
- [59] Bagdonaite, J., Ubachs, W., Murphy, M. T. & Whitmore, J. B. Analysis of molecular hydrogen absorption toward QSO B0642–5038 for a varying proton-to-electron mass ratio. *Astroph. J.* **782**, 10 (2014).
- [60] Albornoz Vásquez, D. *et al.* Molecular hydrogen in the $z_{\text{abs}} = 2.66$ damped Lyman- α absorber towards QJ0643–5041. Physical conditions and limits on the cosmological variation of the proton-to-electron mass ratio. *Astron. Astrophys.* **562**, A88 (2014).

- [61] Ledoux, C., Petitjean, P. & Srianand, R. Molecular hydrogen in a damped Ly α system at $z_{abs} = 4.224$. *Astroph. J. Lett.* **640**, L25–L28 (2006).
- [62] Malec, A. L. *et al.* Keck telescope constraint on cosmological variation of the proton-to-electron mass ratio. *Mon. Not. Roy. Astron. Soc.* **403**, 1541–1555 (2010).
- [63] van Weerdenburg, F., Murphy, M. T., Malec, A. L., Kaper, L. & Ubachs, W. First constraint on cosmological variation of the proton-to-electron mass ratio from two independent telescopes. *Phys. Rev. Lett.* **106**, 180802 (2011).
- [64] Ledoux, C., Petitjean, P., Fynbo, J. P. U., Møller, P. & Srianand, R. Velocity-metallicity correlation for high- z DLA galaxies: evidence of a mass-metallicity relation? *Astron. Astrophys.* **457**, 71–78 (2006).
- [65] Noterdaeme, P., Petitjean, P., Srianand, R., Ledoux, C. & Le Petit, F. Physical conditions in the neutral interstellar medium at $z = 2.43$ toward Q2348–011. *Astron. Astrophys.* **469**, 425–436 (2007).
- [66] Bagdonaite, J., Murphy, M. T., Kaper, L. & Ubachs, W. Constraint on a variation of the proton-to-electron mass ratio from H₂ absorption towards quasar Q2348–011. *Mon. Not. Roy. Astron. Soc.* **421**, 419–425 (2012).
- [67] Petitjean, P., Srianand, R. & Ledoux, C. Molecular hydrogen at $z_{abs} = 1.973$ toward Q0013–004: dust depletion pattern in damped Lyman α systems. *Mon. Not. Roy. Astron. Soc.* **332**, 383–391 (2002).
- [68] Srianand, R. *et al.* Search for cold gas in $z > 2$ damped Ly α systems: 21-cm and H₂ absorption. *Mon. Not. Roy. Astron. Soc.* **421**, 651–665 (2012).
- [69] Ledoux, C., Srianand, R. & Petitjean, P. Detection of molecular hydrogen in a near solar-metallicity damped Lyman-alpha system at $z_{abs} \simeq 2$ toward Q0551–366. *Astron. Astrophys.* **392**, 781–789 (2002).
- [70] Tumlinson, J. *et al.* Cosmological concordance or chemical coincidence? Deuterated molecular hydrogen abundances at high redshift. *Astroph. J. Lett.* **718**, L156–L160 (2010).
- [71] Balashev, S. A., Ivanchik, A. V. & Varshalovich, D. A. HD/H₂ molecular clouds in the early universe: The problem of primordial deuterium. *Ast. Lett.* **36**, 761–772 (2010).

-
- [72] Guimarães, R. *et al.* Metallicities, dust, and molecular content of a QSO-damped Ly α system reaching $\log N(\text{HI}) = 22$: An analog to GRB-DLAs. *Astroph. J.* **143**, 147 (2012).
- [73] Petitjean, P., Srianand, R. & Ledoux, C. Molecular hydrogen and the nature of damped Lyman- α systems. *Astron. Astrophys.* **364**, L26–L30 (2000).
- [74] Fynbo, J. P. U. *et al.* Galaxy counterparts of metal-rich damped Ly α absorbers - II. A solar-metallicity and dusty DLA at $z_{\text{abs}} = 2.58$. *Mon. Not. Roy. Astron. Soc.* **413**, 2481–2488 (2011).
- [75] Varshalovich, D. A., Ivanchik, A. V., Petitjean, P., Srianand, R. & Ledoux, C. HD molecular lines in an absorption system at redshift $z = 2.3377$. *Ast. Lett.* **27**, 683–685 (2001).
- [76] Ivanchik, A. V. *et al.* HD molecules at high redshift: the absorption system at $z = 2.3377$ towards Q1232+082. *Mon. Not. Roy. Astron. Soc.* **404**, 1583–1590 (2010).
- [77] Noterdaeme, P. *et al.* A translucent interstellar cloud at $z = 2.69$. CO, H₂, and HD in the line-of-sight to SDSS J123714.60+064759.5. *Astron. Astrophys.* **523**, A80 (2010).
- [78] Cui, J., Bechtold, J., Ge, J. & Meyer, D. M. Molecular hydrogen in the damped Ly α absorber of Q1331+170. *Astroph. J.* **633**, 649–663 (2005).
- [79] Noterdaeme, P., Petitjean, P., Ledoux, C., Srianand, R. & Ivanchik, A. HD molecules at high redshift. A low astration factor of deuterium in a solar-metallicity DLA system at $z = 2.418$. *Astron. Astrophys.* **491**, 397–400 (2008).
- [80] Srianand, R., Noterdaeme, P., Ledoux, C. & Petitjean, P. First detection of CO in a high-redshift damped Lyman- α system. *Astron. Astrophys.* **482**, L39–L42 (2008).
- [81] Ledoux, C., Petitjean, P. & Srianand, R. The Very Large Telescope Ultraviolet and Visible Echelle Spectrograph survey for molecular hydrogen in high-redshift damped Lyman α systems. *Mon. Not. Roy. Astron. Soc.* **346**, 209–228 (2003).
- [82] Noterdaeme, P., Ledoux, C., Srianand, R., Petitjean, P. & Lopez, S. Diffuse molecular gas at high redshift. Detection of CO molecules and the 2175 Å dust feature at $z = 1.64$. *Astron. Astrophys.* **503**, 765–770 (2009).

- [83] Petitjean, P., Ledoux, C., Noterdaeme, P. & Srianand, R. Metallicity as a criterion to select H₂-bearing damped Lyman- α systems. *Astron. Astrophys.* **456**, L9–L12 (2006).
- [84] Dessauges-Zavadsky, M., Calura, F., Prochaska, J. X., D’Odorico, S. & Matteucci, F. A comprehensive set of elemental abundances in damped Ly α systems: Revealing the nature of these high-redshift galaxies. *Astron. Astrophys.* **416**, 79–110 (2004).
- [85] Muzahid, S., Srianand, R. & Charlton, J. A HST/COS survey of molecular hydrogen in DLAs & sub-DLAs at $z < 1$: Molecular fraction and excitation temperature. *ArXiv e-prints* (2014). 1410.3828.
- [86] Kanekar, N., Prochaska, J. X., Ellison, S. L. & Chengalur, J. N. A search for HI 21cm absorption in strong MgII absorbers in the redshift desert. *Mon. Not. Roy. Astron. Soc.* **396**, 385–401 (2009).
- [87] Prochaska, J. X. *et al.* The First Positive Detection of Molecular Gas in a GRB Host Galaxy. *Astroph. J. Lett.* **691**, L27–L32 (2009).
- [88] Krühler, T. *et al.* Molecular hydrogen in the damped Lyman α system towards GRB 120815A at $z = 2.36$. *Astron. Astrophys.* **557**, A18 (2013).
- [89] D’Elia, V. *et al.* VLT/X-shooter spectroscopy of the GRB 120327A afterglow. *Astron. Astrophys.* **564**, A38 (2014).
- [90] Friis, M. *et al.* The warm, the excited, and the molecular gas: GRB 121024A shining through its star-forming galaxy. *ArXiv e-prints* (2014). 1409.6315.
- [91] Xu, S., Jura, M., Koester, D., Klein, B. & Zuckerman, B. Discovery of molecular hydrogen in white dwarf atmospheres. *Astroph. J. Lett.* **766**, L18 (2013).
- [92] Berengut, J. C. *et al.* Limits on the dependence of the fine-structure constant on gravitational potential from white-dwarf spectra. *Phys. Rev. Lett.* **111**, 010801 (2013).
- [93] van Veldhoven, J. *et al.* Decelerated molecular beams for high-resolution spectroscopy. *Eur. J. Phys. D* **31**, 337–349 (2004).
- [94] Flambaum, V. V. & Kozlov, M. G. Limit on the cosmological variation of m_p/m_e from the inversion spectrum of ammonia. *Phys. Rev. Lett.* **98**, 240801 (2007).

-
- [95] Murphy, M. T., Flambaum, V. V., Muller, S. & Henkel, C. Strong limit on a variable proton-to-electron mass ratio from molecules in the distant universe. *Science* **320**, 1611–1613 (2008).
- [96] Henkel, C. *et al.* The density, the cosmic microwave background, and the proton-to-electron mass ratio in a cloud at redshift 0.9. *Astron. Astrophys.* **500**, 725–734 (2009).
- [97] Špirko, V. Highly sensitive ammonia probes of a variable proton-to-electron mass ratio. *J. Phys. Chem. Lett.* **5**, 919–923 (2014).
- [98] Henkel, C., Braatz, J. A., Menten, K. M. & Ott, J. The kinetic temperature of a molecular cloud at redshift 0.9: ammonia in the gravitational lens PKS 1830-211. *Astron. Astrophys.* **485**, 451–456 (2008).
- [99] Jansen, P., Xu, L.-H., Kleiner, I., Ubachs, W. & Bethlem, H. L. Methanol as a sensitive probe for spatial and temporal variations of the proton-to-electron mass ratio. *Phys. Rev. Lett.* **106**, 100801 (2011).
- [100] Levshakov, S. A., Kozlov, M. G. & Reimers, D. Methanol as a tracer of fundamental constants. *Astroph. J.* **738**, 26 (2011).
- [101] Ellingsen, S. P., Voronkov, M. A., Breen, S. L. & Lovell, J. E. J. First cosmological constraints on the proton-to-electron mass ratio from observations of rotational transitions of methanol. *Astroph. J. Lett.* **747**, L7 (2012).
- [102] Jansen, P., Xu, L.-H., Kleiner, I., Bethlem, H. L. & Ubachs, W. Methyl mercaptan (CH_3SH) as a probe for variation of the proton-to-electron mass ratio. *Phys. Rev. A* **87**, 052509 (2013).
- [103] Jansen, P., Kleiner, I., Xu, L.-H., Ubachs, W. & Bethlem, H. L. Sensitivity of transitions in internal rotor molecules to a possible variation of the proton-to-electron mass ratio. *Phys. Rev. A* **84**, 062505 (2011).
- [104] Viatkina, A. V. & Kozlov, M. G. Sensitivity of tunneling-rotational transitions in ethylene glycol to variation of electron-to-proton mass ratio. *J. Mol. Spectrosc.* **300**, 94–98 (2014).
- [105] Ilyushin, V. V. Sensitivity to a possible variation of the proton-to-electron mass ratio of torsion-rotation transitions in acetone (CH_3)₂CO. *J. Mol. Spectrosc.* **300**, 86–93 (2014).
- [106] Augustovičová, L., Soldán, P., Kraemer, W. P. & Špirko, V. Potential microwave probes of the proton-to-electron mass ratio at very high redshifts. *Mon. Not. Roy. Astron. Soc.* **439**, 1136–1139 (2014).

- [107] Kozlov, M. G. Linear polyatomic molecules with Π ground state: Sensitivity to variation of the fundamental constants. *Phys. Rev. A* **87**, 032104 (2013).
- [108] de Nijs, A. J., Ubachs, W. & Bethlem, H. L. Sensitivity of rotational transitions in CH and CD to a possible variation of fundamental constants. *Phys. Rev. A* **86**, 032501 (2012).
- [109] Truppe, S., Hendricks, R. J., Hinds, E. A. & Tarbutt, M. R. Measurement of the lowest millimeter-wave transition frequency of the CH radical. *Astroph. J.* **780**, 71 (2014).
- [110] Ilyushin, V. V. *et al.* Sensitivity to a possible variation of the proton-to-electron mass ratio of torsion-wagging-rotation transitions in methylvamine CH_3NH_2 . *Phys. Rev. A* **85**, 032505 (2012).
- [111] Kozlov, M. G. Sensitivity of microwave transitions in H_2O_2 to variation of the electron-to-proton mass ratio. *Phys. Rev. A* **84**, 042120 (2011).
- [112] Kozlov, M. G., Porsev, S. G. & Reimers, D. Sensitivity of the isotopologues of hydronium to variation of the electron-to-proton mass ratio. *Phys. Rev. A* **83**, 052123 (2011).
- [113] Wiklind, T. & Combes, F. First detection of CO ($J = 0 - 1$) adsorption at cosmological distances ($z = 0.247$). *Astron. Astrophys.* **286**, L9–L12 (1994).
- [114] Wiklind, T. & Combes, F. Molecular absorptions towards the AGN 1504+377. *Astron. Astrophys.* **315**, 86–94 (1996).
- [115] Kanekar, N. *et al.* Constraints on changes in fundamental constants from a cosmologically distant OH absorber or emitter. *Phys. Rev. Lett.* **95**, 261301 (2005).
- [116] Philip, J., Sprengers, J. P., Cacciani, P., de Lange, C. A. & Ubachs, W. Frequency-mixing scheme for the production of tunable narrowband XUV radiation (91–95 nm): application to precision spectroscopy and predissociation in diatomic molecules. *Appl. Phys. B* **78**, 737–743 (2004).
- [117] Salumbides, E. J. *et al.* Improved laboratory values of the H_2 Lyman and Werner lines for constraining time variation of the proton-to-electron mass ratio. *Phys. Rev. Lett.* **101**, 223001 (2008).
- [118] Bailly, D., Salumbides, E., Vervloet, M. & Ubachs, W. Accurate level energies in the EF1, GK1, H1, B1, B'1, J1 Δ g states of H_2 . *Mol. Phys.* **108**, 827–846 (2010).

-
- [119] Ivanov, T. I. *et al.* Fourier-transform spectroscopy of HD in the vacuum ultraviolet at $\lambda = 87\text{--}112$ nm. *Mol. Phys.* **108**, 771–786 (2010).
- [120] Srianand, R., Petitjean, P., Ledoux, C., Ferland, G. & Shaw, G. The VLT-UVES survey for molecular hydrogen in high-redshift damped Lyman α systems: physical conditions in the neutral gas. *Mon. Not. Roy. Astron. Soc.* **362**, 549–568 (2005).
- [121] Ubachs, W., Bagdonaitė, J., Murphy, M. T., Buning, R. & Kaper, L. Search for Cosmological μ -Variation from High-Redshift H₂ Absorption; A Status Report. In Martins, C. & Molaro, P. (eds.) *From Varying Couplings to Fundamental Physics*, 125–137 (Springer, 2011).
- [122] Wendt, M. & Reimers, D. Variability of the proton-to-electron mass ratio on cosmological scales. *Eur. Phys. J. Spec. Top.* **163**, 197–206 (2008).
- [123] Thompson, R. I. *et al.* An observational determination of the proton to electron mass ratio in the early universe. *Astroph. J.* **703**, 1648–1662 (2009).
- [124] Wendt, M. & Molaro, P. Robust limit on a varying proton-to-electron mass ratio from a single H₂ system. *Astron. Astrophys.* **526**, A96 (2011).
- [125] Varshalovich, D. A. & Levshakov, S. A. On a time dependence of physical constants. *Sov. J. Exp. Theor. Phys.* **58**, 237–240 (1993).
- [126] Murphy, M. T., Tzanavaris, P., Webb, J. K. & Lovis, C. Selection of ThAr lines for wavelength calibration of echelle spectra and implications for variations in the fine-structure constant. *Mon. Not. Roy. Astron. Soc.* **378**, 221–230 (2007).
- [127] Murphy, M. T., Webb, J. K. & Flambaum, V. V. Revision of VLT/UVES constraints on a varying fine-structure constant. *Mon. Not. Roy. Astron. Soc.* **384**, 1053–1062 (2008).
- [128] Whitmore, J. B., Murphy, M. T. & Griest, K. Wavelength calibration of the VLT-UVES spectrograph. *Astroph. J.* **723**, 89–99 (2010).
- [129] Bekenstein, J. D. Fine-structure constant variability, equivalence principle, and cosmology. *Phys. Rev. D* **66**, 123514 (2002).
- [130] Wendt, M. & Molaro, P. QSO 0347–383 and the invariance of m_p/m_e in the course of cosmic time. *Astron. Astrophys.* **541**, A69 (2012).
- [131] Ivanchik, A. *et al.* A new constraint on the time dependence of the proton-to-electron mass ratio. Analysis of the Q0347–383 and Q0405–443 spectra. *Astron. Astrophys.* **440**, 45–52 (2005).

- [132] Kanekar, N. Constraining changes in the proton-electron mass ratio with inversion and rotational Lines. *Astroph. J. Lett.* **728**, L12 (2011).
- [133] Salumbides, E. J., Dickenson, G. D., Ivanov, T. I. & Ubachs, W. QED effects in molecules: test on rotational quantum states of H₂. *Phys. Rev. Lett.* **107**, 043005 (2011).
- [134] Malec, A. L. *et al.* VizieR Online Data Catalog: Lyman and Werner molecular hydrogen transitions (Malec+, 2010). *VizieR Online Data Catalog* **740**, 31541 (2010).
- [135] King, J. A. *Searching for variations in the fine-structure constant and the proton-to-electron mass ratio using quasar absorption lines.* Ph.D. thesis (2012).
- [136] Akaike, H. A new look at the statistical model identification. *IEEE Trans. Autom. Control* **19**, 716–723 (1974).
- [137] Edlen, B. Report of the committee on standards of wavelength. *Transactions of the International Astronomical Union, Series B* **12**, 176 (1966).
- [138] Roy, N., Chengalur, J. N. & Srianand, R. A multiwavelength investigation of the temperature of the cold neutral medium. *Mon. Not. Roy. Astron. Soc.* **365**, L1–L5 (2006).
- [139] Cecchi-Pestellini, C., Casu, S. & Dalgarno, A. H₂ excitation in turbulent interstellar clouds. *Mon. Not. Roy. Astron. Soc.* **364**, 1309–1314 (2005).
- [140] Rachford, B. L. *et al.* A far ultraviolet spectroscopic explorer survey of interstellar molecular hydrogen in translucent clouds. *Astroph. J.* **577**, 221–244 (2002).
- [141] Abgrall, H., Roueff, E., Launay, F. & Roncin, J.-Y. The B¹Σ_u⁺ → X¹Σ_g⁺ and D¹Π_u⁺ → X¹Σ_g⁺ band systems of molecular hydrogen. *Can. J. Phys.* **72**, 856 (1994).
- [142] D’Odorico, S. *et al.* Performance of UVES, the echelle spectrograph for the ESO VLT and highlights of the first observations of stars and quasars. In Bergeron, J. (ed.) *Discoveries and Research Prospects from 8- to 10-Meter-Class Telescopes*, vol. 4005 of *Proc. Soc. Photo. Opt. Instrum. Eng.*, 121–130 (2000).
- [143] Griest, K. *et al.* Wavelength accuracy of the Keck HIRES spectrograph and measuring changes in the fine structure constant. *Astroph. J.* **708**, 158–170 (2010).

-
- [144] Chance, K. & Kurucz, R. L. An improved high-resolution solar reference spectrum for earth's atmosphere measurements in the ultraviolet, visible, and near infrared. *J. Quant. Spectrosc. Radiat. Transfer* **111**, 1289–1295 (2010).
- [145] Evans, T. M. & Murphy, M. T. A new method for detecting velocity shifts and distortions between optical spectra. *Astroph. J.* **778**, 173 (2013).
- [146] Barrow, J. D., Sandvik, H. B. & Magueijo, J. Anthropic reasons for nonzero flatness and Λ . *Phys. Rev. D* **65**, 123501 (2002).
- [147] Perlmutter, S. Nobel Lecture: Measuring the acceleration of the cosmic expansion using supernovae. *Rev. Mod. Phys.* **84**, 1127–1149 (2012).
- [148] Schmidt, B. P. Nobel Lecture: Accelerating expansion of the universe through observations of distant supernovae. *Rev. Mod. Phys.* **84**, 1151–1163 (2012).
- [149] Riess, A. G. Nobel Lecture: My path to the accelerating universe. *Rev. Mod. Phys.* **84**, 1165–1175 (2012).
- [150] Ratra, B. & Peebles, P. J. E. Cosmological consequences of a rolling homogeneous scalar field. *Phys. Rev. D* **37**, 3406–3427 (1988).
- [151] Carroll, S. M. Quintessence and the rest of the world: suppressing long-range interactions. *Phys. Rev. Lett.* **81**, 3067–3070 (1998).
- [152] Damour, T. & Dyson, F. The Oklo bound on the time variation of the fine-structure constant revisited. *Nucl. Phys. B* **480**, 37–54 (1996).
- [153] Jansen, P., Bethlem, H. L. & Ubachs, W. Perspective: Tipping the scales: Search for drifting constants from molecular spectra. *J. Chem. Phys.* **140**, 010901 (2014).
- [154] Riechers, D. A. *et al.* A dust-obscured massive maximum-starburst galaxy at a redshift of 6.34. *Nature* **496**, 329–333 (2013).
- [155] Molaro, P. *et al.* UVES radial velocity accuracy from asteroid observations. I. Implications for fine structure constant variability. *Astron. Astrophys.* **481**, 559–569 (2008).
- [156] Levshakov, S. A. *et al.* An upper limit to the variation in the fundamental constants at redshift $z = 5.2$. *Astron. Astrophys.* **540**, L9 (2012).
- [157] Thompson, R. I., Martins, C. J. A. P. & Vielzeuf, P. E. Constraining cosmologies with fundamental constants - I. Quintessence and K-essence. *Mon. Not. Roy. Astron. Soc.* **428**, 2232–2240 (2013).

- [158] Brax, P. Environmental variation of constants in screened modified theories of gravity. *Phys. Rev. D* **90**, 023505 (2014).
- [159] Brans, C. & Dicke, R. H. Mach's principle and a relativistic theory of gravitation. *Phys. Rev.* **124**, 925–935 (1961).
- [160] Barrow, J. D. & Lip, S. Z. W. Generalized theory of varying alpha. *Phys. Rev. D* **85**, 023514 (2012).
- [161] Barrow, J. D. Cosmological bounds on spatial variations of physical constants. *Phys. Rev. D* **71**, 083520 (2005).
- [162] Scóccola, C. G., Mosquera, M. E., Landau, S. J. & Vucetich, H. Time variation of the electron mass in the early universe and the Barrow-Magueijo model. *Astroph. J.* **681**, 737–746 (2008).
- [163] Calmet, X. & Fritzsche, H. The cosmological evolution of the nucleon mass and the electroweak coupling constants. *Eur. Phys. J. C* **24**, 639–642 (2002).
- [164] Magueijo, J., Barrow, J. D. & Sandvik, H. B. Is it e or is it c ? Experimental tests of varying α . *Phys. Lett. B* **549**, 284–289 (2002).
- [165] Will, C. M. The confrontation between general relativity and experiment. *Living Rev. Relat.* **17**, 4 (2014).
- [166] Ferrell, S. J. *et al.* Investigation of the gravitational-potential dependence of the fine-structure constant using atomic dysprosium. *Phys. Rev. A* **76**, 062104 (2007).
- [167] Fortier, T. M. *et al.* Precision atomic spectroscopy for improved limits on variation of the fine structure constant and local position invariance. *Phys. Rev. Lett.* **98**, 070801 (2007).
- [168] Blatt, S. *et al.* New limits on coupling of fundamental constants to gravity using ^{87}Sr optical lattice clocks. *Phys. Rev. Lett.* **100**, 140801 (2008).
- [169] Abgrall, H., Roueff, E., Launay, F., Roncin, J. Y. & Subtil, J. L. The Lyman and Werner band systems of molecular hydrogen. *J. Mol. Spectrosc.* **157**, 512–523 (1993).
- [170] Komasa, J. *et al.* Quantum electrodynamics effects in rovibrational spectra of molecular hydrogen. *J. Chem. Theory Comput.* **7**, 3105–3115 (2011).
- [171] Dickenson, G. D. *et al.* Fundamental vibration of molecular hydrogen. *Phys. Rev. Lett.* **110**, 193601 (2013).

-
- [172] Salumbides, E. J., Bagdonaite, J., Abgrall, H., Roueff, E. & Ubachs, W. H₂ Lyman and Werner band lines and their sensitivity for a variation of the proton–electron mass ratio in the gravitational potential of white dwarfs. *Submitted*. (2014).
- [173] Xu, S., Jura, M., Koester, D., Klein, B. & Zuckerman, B. Elemental compositions of two extrasolar rocky planetesimals. *Astroph. J.* **783**, 79 (2014).
- [174] Abgrall, H., Roueff, E. & Drira, I. Total transition probability and spontaneous radiative dissociation of B, C, B' and D states of molecular hydrogen. *Astron. Astrophys. Suppl. Ser.* **141**, 297–300 (2000).
- [175] Koester, D. *et al.* High-resolution UVES/VLT spectra of white dwarfs observed for the ESO SN Ia Progenitor Survey. III. DA white dwarfs. *Astron. Astrophys.* **505**, 441–462 (2009).
- [176] Thompson, S. E., Clemens, J. C., van Kerkwijk, M. H. & Koester, D. High-resolution spectroscopy of the pulsating white dwarf G29-38. *Astroph. J.* **589**, 921–930 (2003).
- [177] Silvotti, R., Pavlov, M., Fontaine, G., Marsh, T. & Dhillon, V. The ZZ Ceti instability strip as seen by VLT-ULTRACAM. *Mem. Soc. Astron. Ital.* **77**, 486 (2006).
- [178] Smolin, L. Cosmological natural selection as the explanation for the complexity of the universe. *Phys. A* **340**, 705–713 (2004).
- [179] Lin, C. C. & Swalen, J. D. Internal rotation and microwave spectroscopy. *Rev. Mod. Phys.* **31**, 841–891 (1959).
- [180] Muller, S. *et al.* Molecules at $z = 0.89$. A 4-mm-rest-frame absorption-line survey toward PKS 1830–211. *Astron. Astrophys.* **535**, A103 (2011).
- [181] Lovas, F. J. NIST recommended rest frequencies for observed interstellar molecular microwave transitions-2002 revision. *J. Phys. Chem. Ref. Data* **33**, 177–355 (2004).
- [182] Jauncey, D. L. *et al.* An unusually strong Einstein ring in the radio source PKS1830–211. *Nature* **352**, 132–134 (1991).
- [183] Lidman, C. *et al.* The redshift of the gravitationally lensed radio source PKS 1830–211. *Astroph. J. Lett.* **514**, L57–L60 (1999).
- [184] Wiklind, T. & Combes, F. The redshift of the gravitational lens of PKS1830–211 determined from molecular absorption lines. *Nature* **379**, 139–141 (1996).

- [185] Chengalur, J. N., de Bruyn, A. G. & Narasimha, D. HI and OH absorption at $z = 0.89$. *Astron. Astrophys.* **343**, L79–L82 (1999).
- [186] Muller, S. & Guélin, M. Drastic changes in the molecular absorption at redshift $z = 0.89$ toward the quasar PKS 1830–211. *Astron. Astrophys.* **491**, 739–746 (2008).
- [187] Menten, K. M. *et al.* Submillimeter water and ammonia absorption by the peculiar $z \simeq 0.89$ interstellar medium in the gravitational lens of the PKS 1830–211 system. *Astron. Astrophys.* **492**, 725–730 (2008).
- [188] Leurini, S. *et al.* Methanol as a diagnostic tool of interstellar clouds. I. Model calculations and application to molecular clouds. *Astron. Astrophys.* **422**, 573–585 (2004).
- [189] Breckenridge, S. M. & Kukolich, S. G. Precise laboratory measurements of methanol rotational transition frequencies in the 5 to 13 GHz region. *Astroph. J.* **438**, 504–505 (1995).
- [190] Heuvel, J. E. M. & Dymanus, A. Hyperfine structure of CH₃OH. *J. Mol. Spectrosc.* **45**, 282–292 (1973).
- [191] Müller, H. S. P., Menten, K. M. & Mäder, H. Accurate rest frequencies of methanol maser and dark cloud lines. *Astron. Astrophys.* **428**, 1019–1026 (2004).
- [192] van der Tak, F. F. S., Black, J. H., Schöier, F. L., Jansen, D. J. & van Dishoeck, E. F. A computer program for fast non-LTE analysis of interstellar line spectra. With diagnostic plots to interpret observed line intensity ratios. *Astron. Astrophys.* **468**, 627–635 (2007).
- [193] Sastry, K. V. L. N., Lees, R. M. & De Lucia, F. C. Microwave and submillimeter-wave spectra of CH₃OH. *J. Mol. Spectrosc.* **103**, 486–494 (1984).
- [194] Herbst, E., Messer, J. K., De Lucia, F. C. & Helminger, P. A new analysis and additional measurements of the millimeter and submillimeter spectrum of methanol. *J. Mol. Spectrosc.* **108**, 42–57 (1984).
- [195] Muller, S. *et al.* A precise and accurate determination of the cosmic microwave background temperature at $z = 0.89$. *Astron. Astrophys.* **551**, A109 (2013).
- [196] Levshakov, S. A. *et al.* Searching for chameleon-like scalar fields with the ammonia method. II. Mapping of cold molecular cores in NH₃ and HC₃N lines. *Astron. Astrophys.* **524**, A32 (2010).

- [197] van der Tak, F. F. S., Müller, H. S. P., Harding, M. E. & Gauss, J. Hyperfine structure in the $J = 1 - 0$ transitions of DCO^+ , DNC , and HN^{13}C : astronomical observations and quantum-chemical calculations. *Astron. Astrophys.* **507**, 347–354 (2009).
- [198] Guirado, J. C. *et al.* Dual-frequency VLBI observations of the gravitational lens system PKS 1830–211. *Astron. Astrophys.* **346**, 392–396 (1999).
- [199] Martí-Vidal, I. *et al.* Probing the jet base of the blazar PKS 1830-211 from the chromatic variability of its lensed images. Serendipitous ALMA observations of a strong gamma-ray flare. *Astron. Astrophys.* **558**, A123 (2013).

Publication list

- *Constraint on a variation of the proton-to-electron mass ratio from H_2 absorption toward quasar Q2348–011.*
Bagdonaite, J., Murphy, M. T., Kaper, L. & Ubachs, W.
Mon. Not. Roy. Astron. Soc. **421**, 419-425 (2012).
- *A stringent limit on a drifting proton-to-electron mass ratio from alcohol in the early universe.*
Bagdonaite, J., Jansen, P., Henkel, C., Bethlem, H. L., Menten, K. M. & Ubachs, W.
Science **339**, 46-48, (2013).
- *Robust constraint on a drifting proton-to-electron mass ratio at $z = 0.89$ from methanol observation at three radio telescopes.*
Bagdonaite, J., Dapra, M., Jansen, P., Bethlem, H. L., Ubachs, W., Muller, S., Henkel, C. & Menten, K. M.
Phys. Rev. Lett. **111**, 231101 (2013).
- *Analysis of molecular hydrogen absorption toward QSO B0642–5038 for a varying proton-to-electron mass ratio.*
Bagdonaite, J., Ubachs, W., Murphy, M. T. & Whitmore, J. B.
Astroph. J. **782**, 10 (2014).
- *Limits on a gravitational field dependence of the proton–electron mass ratio from H_2 in white dwarf stars.*
Bagdonaite, J., Salumbides, E. J., Preval, S. P., Barstow, M. A., Barrow, J. D., Murphy, M. T. & Ubachs, W.
Phys. Rev. Lett. **113**, 123002 (2014).
- *Constraint on a varying proton–electron mass ratio 1.5 billion years after the Big Bang.*
Bagdonaite, J., Ubachs, W., Murphy, M. T. & Whitmore, J. B.
Accepted for publication in Phys. Rev. Lett. (2015).

Additional publications (not part of the thesis)

- *Search for cosmological μ -variation from high-redshift H_2 absorption; A status report.*
Ubachs, W., Bagdonaite, J., Murphy, M. T., Buning, R. & Kaper, L.
In: From Varying Couplings to Fundamental Physics (pp. 125–137).
Springer Berlin Heidelberg. (2011).
- *CO A–X system for constraining cosmological drift of the proton–electron mass ratio.*
Salumbides, E. J., Niu, M. L., Bagdonaite, J., de Oliveira, N., Joyeux, D., Nahon, L. & Ubachs, W.
Phys. Rev. A **86**, 022510 (2012).
- *Galaxy counterparts of metal-rich damped Ly- α absorbers – The case of J205922.4–052842.*
Hartoog, O. E., Fynbo, J. P. U., Kaper, L., De Cia, A., & Bagdonaite, J.
Mon. Not. Roy. Astron. Soc. **447**, 2738 (2015).
- *The inhomogeneous ISM toward PKS 1830–211 SW – A detailed view on molecular gas at a look-back time of 7.5 Gyr.*
Schulz, A., Henkel, C., Menten, K. M., Muller, S., Muders, D., Bagdonaite, J. & Ubachs, W.
Astron. Astrophys. **574**, A108 (2015).
- *Constraints on changes in the proton–electron mass ratio using methanol lines.*
Kanekar, N., Ubachs, W., Menten, K. M., Bagdonaite, J., Brunthaler, A., Henkel, C., Muller, S., Bethlem, H. L. & Dapra, M.
Accepted for publication in Mon. Not. Roy. Astron. Soc. Lett. (2015).
- *H_2 Lyman and Werner band lines and their sensitivity for a variation of the proton–electron mass ratio in the gravitational potential of white dwarfs.*
Salumbides, E. J., Bagdonaite, J., Abgrall, H., Roueff, E. & Ubachs, W.
Submitted (2014).

Summary

The standard model (SM) of particle physics is a theory with remarkable predictive power. One great example of its success is the recent discovery of the Higgs boson. However, at the same time the SM is incompatible with general relativity – a theory tested and trusted just as much. Furthermore, certain ad hoc features maintained by the SM indicate that its explanatory insights are not as broad and exhaustive as one would hope. One of the features that looks arbitrary is the number and the values of the free parameters of the SM or so-called fundamental constants. These constants include the masses of elementary particles and the strengths of the forces of nature which combined govern the chemical complexity of our universe. What is probably most unsettling is that the values of constants can only be measured experimentally and any attempts to derive them from first principles have so far proven unsuccessful. Is it simply nature’s last word or does it mean that the particular principles are yet to be discovered? Driven by this question, various propositions have been made where in alternate universes constants would take different values. In the meantime, the specific values of the fundamental constants featured by our universe continue to be the subject of great experimental scrutiny.

In this thesis, we explore the most basic question one can ask about a constant: is it actually constant? In particular, the focus of the present work is on the proton–electron mass ratio μ whose constancy is probed via spectroscopic measurements of sensitive transitions in molecular hydrogen (H_2) and methanol (CH_3OH) found in distant galaxies and in white dwarf atmospheres.

Most of the thesis (Chapters 2–4, 6, and 7) is based on astronomical observations of molecular clouds at intermediate-to-high redshifts which correspond to lookback times of 7.5 to 12.4 billion years. Cold gaseous material in the sightlines to distant quasars will absorb light at specific wavelengths according to the redshift and the chemical species present. The overall redshift z of a given absorption system is shared among all the transitions. Regarding the sensitive molecular species, individual transitions may show additional distinctive shifts due to a variation of μ . Hence, we can uncover a relative constraint of $\Delta\mu/\mu$ by comparing a relative pattern of H_2 or CH_3OH transitions observed in the astronomical sources to a corresponding pattern found under local μ .

At redshifts $z > 2$, the rovibronic H_2 transitions with rest-frame wavelengths in the ultraviolet range ($\lambda_0 < 115 \text{ nm}$) are shifted into the optical win-

dow accessible with the Ultraviolet and Visual Echelle Spectrograph mounted on the Very Large Telescope. Chapter 2 presents an analysis of an H₂ absorption system at $z_{\text{abs}} = 2.43$, observed toward the quasar Q2348–011. The H₂ absorption profile exhibits seven velocity features, which, for an H₂ absorber, is unusually complex. The selected 32 transitions were modeled simultaneously with the surrounding and overlapping Lyman- α forest which consists of multiple transitions arising in neutral hydrogen clouds in the same line of sight. A comprehensive fitting method was applied allowing for parameter tying based on known molecular physics. The profiles were modeled using the VPFIT software by fitting the data with multiple Voigt profiles. The study resulted in a $\Delta\mu/\mu$ limit of $(-0.68 \pm 2.78) \times 10^{-5}$ which, although not as constraining, is in agreement with other $\Delta\mu/\mu$ limits obtained at that redshift range.

In Chapters 3 and 4, the same methodology as in Chapter 2 was applied to two different H₂ absorbers observed, respectively, at $z_{\text{abs}} = 2.66$ toward quasar B0642–5038, and at $z_{\text{abs}} = 4.22$ toward quasar J1443+2724. The B0642–5038 absorber exhibits a much simpler absorption profile with a single velocity feature. A relatively high number of transitions (111) was included in the analysis which resulted in a final constraint of $\Delta\mu/\mu = (12.7 \pm 6.2) \times 10^{-6}$. At the accuracy level of several parts per million, the result was found to be sensitive to a number of different systematic effects, most notably to the long range wavelength distortions discovered in the Ultraviolet and Visual Echelle Spectrograph. A correction of the wavelength scale was implemented based on spectral analysis of asteroids and solar twins. The correction reduced the significance of a 3- σ non-zero $\Delta\mu/\mu$ which was obtained initially and increased the systematic uncertainty.

Detected at $z_{\text{abs}} = 4.22$, the H₂ absorber toward J1443+2724 allowed us to obtain the highest redshift direct $\Delta\mu/\mu$ measurement so far. An analysis of 89 H₂ transitions, which are each seen in two velocity features, yielded a $\Delta\mu/\mu$ limit of $(-9.5 \pm 7.6) \times 10^{-6}$. Altogether, the results presented in Chapters 2–4, which focus on high redshift H₂ absorbers, do not provide evidence for varying μ .

Chapter 5 is based on Galactic observations of white dwarfs, which are the compact remnant cores of low-mass stars. Detection of H₂ in their atmospheres (observed with the Hubble Space Telescope/Cosmic Origins Spectrograph) allowed to test for a possible μ dependence on gravity. A much higher temperature than in cold intergalactic clouds prompted sensitivity coefficient calculations for transitions from higher vibrational levels. A novel fitting method was applied where all the observed lines (close to a thousand per spectrum) were modeled by invoking only five free parameters in total. The analysis of the white dwarf GD133 yielded a constraint of $\Delta\mu/\mu = (-2.7 \pm 4.7) \times 10^{-5}$ for a gravitational potential ten thousand times stronger than that on the Earth. The white dwarf G29–38, with an even stronger gravitational poten-

tial, yielded $\Delta\mu/\mu = (-5.8 \pm 3.8) \times 10^{-5}$.

In Chapters 6 and 7, a galaxy at redshift $z = 0.89$ toward PKS1830–211 is investigated to put a $\Delta\mu/\mu$ constraint at a stringent 10^{-7} accuracy level. Although being less numerous compared to a typical H_2 spectrum, the detected methanol absorption lines offer a huge advantage of enhanced sensitivity to μ variation. The sensitive rotational CH_3OH transitions are redshifted into the radio range from 0.1 to 5.0 cm. They were initially observed with the Effelsberg telescope (Chapter 6), later adding more observations from the Institut de Radio Astronomie Millimétrique 30-m telescope and the Atacama Large Millimeter/submillimeter Array (Chapter 7). The combined results are presented in Chapter 7, where various systematic effects are explored such as chemical segregation, excitation temperature, frequency dependence and time-variability of the background source. The study resulted in a constraint of $\Delta\mu/\mu = (-1.0 \pm 0.8_{\text{stat}} \pm 1.0_{\text{sys}}) \times 10^{-7}$. In conclusion, the radio measurements of methanol transitions at a lookback time of 7.5 billion years show no indication of varying μ .

Samenvatting

Zoektocht naar een verandering van de proton–electron massaverhouding via waterstof- en methanolmolekulen

Het Standaardmodel van de natuurkunde is een theorie met een uitzonderlijke voorspellingskracht. Een groots voorbeeld van haar succes is de recente ontdekking van het Higgs deeltje. Tegelijkertijd is het Standaardmodel onverenigbaar met de Algemene Relativiteitstheorie – een theorie die evenzeer veelvuldig getest is. Bovendien bevat het Standaardmodel enkele ad hoc veronderstellingen die aangeven dat de verklarende inzichten niet zo breed en uitputtend zijn als men zou hopen. Een van de aspecten die willekeurig lijken is het aantal en de waarden van de vrije parameters in het Standaardmodel, de zogenaamde natuurconstanten. Deze constanten bepalen de massa's van de elementaire deeltjes en de sterkte van de verschillende natuurkrachten, die in combinatie de chemische complexiteit van ons universum bepalen. Waarschijnlijk het meest verontrustend is dat de waarden van de natuurconstanten slechts gemeten kunnen worden en dat alle pogingen om een theoretische onderbouwing te vinden, zijn gestrand. Is dit eenvoudigweg het laatste woord van de natuur, of betekent het dat er nog diepere lagen te ontdekken zijn? Gedreven door deze vraag zijn verschillende suggesties gedaan, bijvoorbeeld dat er andere universa zouden bestaan, waarin de natuurconstanten andere waarden aannemen. Intussen worden de specifieke waarden van de fundamentele constanten onderworpen aan de meest stringente experimentele toetsen.

In dit proefschrift wordt de meest fundamentele vraag gesteld over een natuurconstante: is deze werkelijk constant? In het bijzonder ligt de nadruk van de voorliggende studie op de proton-electron massaverhouding μ , wier constantheid getoetst wordt via spectroscopische metingen aan gevoelige overgangen in moleculair waterstof (H_2) en methanol (CH_3OH). Deze worden waargenomen in ver weg gelegen melkwegstelsels en in atmosferen van witte dwergen.

Een belangrijk deel van dit proefschrift (Hoofdstukken 2-4, 6 en 7) is gebaseerd op astronomische waarnemingen van moleculaire wolken bij matige tot hoge roodverschuiving, corresponderend met een terugkijktijd van 7.5 tot 12.4 miljard lichtjaar. Koud gasvormig materiaal in de gezichtslijn naar ver weg gelegen quasars absorberen licht bij specifieke golflengtes corresponderend met

de roodverschuiving en het soort molecuul. De roodverschuiving z van een gegeven absorptiesysteem is hetzelfde voor alle spectrale overgangen. Voor wat betreft de gevoeligheid van moleculen voor een verandering van μ : individuele overgangen ondergaan een specifieke verschuiving; de mate van verschuiving hangt af van het soort molecuul, de betreffende overgang en de waarde van $\Delta\mu$. Zo kunnen we een relatieve limitering van $\Delta\mu/\mu$ bepalen door een patroon van H_2 of CH_3OH lijnen, die worden waargenomen in sterrenkundige bronnen, te vergelijken met een patroon gemeten bij een lokale waarde van μ .

Bij roodverschuivingen van $z > 2$ worden rovibronische overgangen in H_2 met laboratorium golflengtes in het ultraviolet ($\lambda_0 < 115$ nm) verschoven naar het optische venster dat toegankelijk is voor het UVES instrument op de ESO Very Large Telescope. In Hoofdstuk 2 wordt een analyse van het absorptiesysteem in de gezichtslijn naar de quasar Q2348–011 bij roodverschuiving $z = 2.43$ geanalyseerd. Het H_2 absorptieprofiel bestaat uit zeven afzonderlijke snelheidscomponenten, die het absorptiespectrum zeer complex maken. De geselecteerde 32 overgangen zijn gemodelleerd, samen met de overlappende lijnen in het woud van lijnen behorend bij atomair waterstof in dezelfde gezichtslijn. Een omvattende fitprocedure is toegepast, die het mogelijk maakt parameters vast te leggen uit bekende molecuulfysika. De lijnprofielen worden gemodelleerd met de VPFIT software waarin lijnen aan Voigt-profielen worden aangepast. Het resultaat van de studie geeft een limiet voor $\Delta\mu/\mu$ op de waarde $(-0.68 \pm 2.78) \times 10^{-5}$, in overeenstemming met andere limieten bepaald bij deze roodverschuiving.

In Hoofdstukken 3 en 4 wordt dezelfde methodologie toegepast op twee andere H_2 -absorptiesystemen, namelijk die bij roodverschuiving $z = 2.66$ in de richting van quasar B0642–5038, en die bij $z = 4.22$ in de richting van J1443+2724. Het systeem in de richting van B0642–5038 kent een eenvoudig absorptieprofiel met een enkele snelheidscomponent. Een relatief groot aantal overgangen (111) is meegenomen in de analyse resulterend in een uiteindelijke limiet van $\Delta\mu/\mu = (12.7 \pm 6.2) \times 10^{-6}$. Op het nauwkeurighedsniveau van enkele delen per miljoen is dit resultaat gevoelig voor een aantal systematische effecten in de analyse, vooral die van een langgolvlige verstoring in de ijking van de UVES spectrograaf. Een correctie van de golflengteschaal werd geïmplementeerd, gebaseerd op ijkmetingen aan asteroiden en sterren gelijkend op de zon. Deze correctie zorgt er voor dat een initieel verkregen 3- σ effect wordt gecompenseerd.

Het H_2 absorptiesysteem in de richting van J1443+2724, waargenomen bij $z = 4.22$, stelt ons in staat een limitering op $\Delta\mu/\mu$ te bepalen bij de hoogste roodverschuiving tot dusverre. Uit een analyse van 89 H_2 lijnen, die worden waargenomen als twee snelheidscomponenten, volgt een limiet op $\Delta\mu/\mu$ van $(-9.5 \pm 7.6) \times 10^{-6}$. Al met al geven deze resultaten over H_2 absorptiesystemen bij hoge roodverschuiving, als gepresenteerd in Hoofdstukken 2-4, geen

aanwijzing voor een variërende waarde van μ .

Hoofdstuk 5 handelt over waarnemingen van witte dwergen in ons melkwegstelsel. Een witte dwerg is de uitgebrande compacte kern van een lage-massa ster zoals de zon. Waarneming van H_2 in hun atmosfeer, in dit geval met de Cosmic Origins Spectrograph aan boord van de Hubble Space Telescope, maakt het mogelijk om het effect van een afhankelijkheid van μ op een zwaartekrachtsveld te meten. De veel hogere temperatuur in de dwergster-atmosfeer, in vergelijking met de koude intergalactische wolken, vereiste een berekening van gevoeligheidscoëfficiënten van overgangen in H_2 uit hogere vibratieniveaus. Ook werd een nieuwe fitprocedure toegepast waarin alle waargenomen lijnen (wel duizend per spectrum) gemodelleerd werden met slechts 5 parameters. De analyse van de witte dwerg GD133 leverde een limitering van $\Delta\mu/\mu$ van $(-2.7 \pm 4.7) \times 10^{-5}$ in een gravitatiepotentiaal tienduizend keer zo sterk als op aarde. De witte dwerg G29–38, met een zelfs sterker zwaartekrachtsveld, leverde een limitering op van $\Delta\mu/\mu$ van $(-5.8 \pm 3.8) \times 10^{-5}$.

In Hoofdstukken 6 en 7 wordt een melkwegstelsel bij roodverschuiving $z = 0.89$ in de richting van PKS1830–211 bestudeerd met als resultaat een limitering op het niveau van 10^{-7} . Hoewel minder spectraallijnen worden waargenomen dan in een typisch H_2 -spectrum, hebben de methanol absorptielijnen het enorme voordeel van hun grote gevoeligheid voor μ -variatie. De gevoelige CH_3OH rotatielijnen zijn roodverschoven in het radiogebied tussen 0.1 en 5.0 cm. De lijnen werden in eerste instantie waargenomen met de Effelsberg radiotelescoop (Hoofdstuk 6). Later werden meer lijnen toegevoegd uit waarnemingen op de 30m telescoop van IRAM en de ALMA radio telescoop. De gecombineerde resultaten worden in Hoofdstuk 7 gepresenteerd, waarin ook systematische effecten worden behandeld als gevolg van chemische inhomogeniteit, excitatietemperatuur, frequentieafhankelijkheid en variabiliteit van de radiobron in de achtergrond. Deze studie resulteert in een limitering van $\Delta\mu/\mu$ van $(-1.0 \pm 0.8_{\text{stat}} \pm 1.0_{\text{sys}}) \times 10^{-7}$. Concluderend kan gesteld worden dat de radiowaarnemingen aan methanol bij een terugkijktijd van 7.5 miljard jaar geen indicatie verschaffen voor een variatie van μ .

Acknowledgments

It's my greatest pleasure to start the acknowledgments by thanking my PhD advisor Wim Ubachs. Wim, during the past four years we spent working together, unknowingly, you put all my future bosses in risk of never meeting the high standards I now have for a boss. Thanks for your never-failing encouragement, lessons on science and on writing about science, and for believing in me more than I myself dared to. Warm thanks to my co-advisor Lex Kaper who has supported me in all matters from my day one in Amsterdam. Thanks also to Michael Murphy, my advisor from Melbourne, who tried and, I want to believe, succeeded to make my research better.

I'm grateful to Freek van Weerdenburg and Adrian Malec for teaching me how to deal with our special friend, VPFIT. Special thanks to Christian Henkel for introducing me both to radio astronomy and to the controls of the Effelsberg telescope. Big thanks to Paul Jansen for methanol. I'm grateful to Rick Bethlem for the experience of writing and thinking together from which I'm sure I benefited much more than him. Thanks to Nissim Kanekar, Sebastien Muller, and Karl Menten for sharing their knowledge about radio astronomy with me. Thanks to Simon Preval, Martin Barstow, and John Barrow for an efficient collaboration on the white dwarf paper. I'm glad I had a couple of chances to work with Edcel Salumbides whose positive and professional outlook I always admire. Thanks to Olga Hartoog for introducing me to spectroscopy with the X-Shooter. I would like to thank Mario Dapra for his company and I wish him many bright quasars. Thanks to our secretary Marja Herronen who helped me an uncountable number of times. Thanks to Thijs Rotteveel for producing the cover design.

I'd like to thank the VU University Amsterdam and the Foundation for Fundamental Research on Matter for the financial support of my research. Also, I feel very lucky I had a chance to do observations or use data from several telescopes, including the Very Large Telescope of the European Southern Observatory, the Effelsberg radio telescope, the Institute de Radio Astronomie Millimétrique 30-m telescope, the Atacama Large Millimeter/submillimeter Array, and the Hubble Space Telescope. Not only everything was free of charge but all the facilities have great support teams who can save one a lot of time and trouble. I'm very grateful for all the technical support I have received.

I'd like to take the opportunity to express my gratitude to my ex-colleagues

from the Center for Physical Sciences and Technology in Vilnius for the first experience of ‘doing astronomy’. I’d also like to thank my past and present fellow students and staff from the VU University of Amsterdam, Department of Physics and Astronomy. Thanks to you, I learned a lot more about lasers and lab work than I ever thought I would. I wish you all the best in your future work and research.

My PhD would have been very different and much more difficult if not for the many colleagues who became my good friends. Among many other things, I’d like to thank Alan for trying to figure out Fokke & Sukke with me (although I’m afraid they’re still beyond us). Thanks to Itan for deciding to share an office with me and for the friendship outside the university. Thanks to Thomas for the many nicknames, laughs and lunches. I wish to thank Jonas, Astrid, Cesar and Alicia for all the warm memories that never fail to put a smile on my face. I’m grateful to Remy for stopping by and making life much more fun. Thanks to my friends from the biophysics department for the fun and nerdy breaks from work. Thanks to Anna for her caring friendship that started in Melbourne and continues across one or the other ocean. Last but not least, I’m glad that during my PhD I wasn’t the only woman in the group and, what’s more, the other woman was Marina Quintero Pérez who has been a wonderful friend to me.

For many beautiful moments I want to thank my friend Simona who, fortunately to me, happened to move to Amsterdam at a similar time and we have been jointly looking for our way in every sense. Thanks also to my other Lithuanian friends in Lithuania and in the world. It always feels genuine and fulfilling as we pick up the conversation where it was left off no matter how much time has passed.

I want to thank my parents and my brother for always being there for me. Thanks to Jonathan for ceaselessly supporting me on all fronts.

Finally, thanks to my uncle Robertas who instilled many nerdy things into my (then) young and uncontaminated mind: ‘Learn English, learn how to program, and study physics. Now why don’t we go and look for some meteorites?’ You can’t say no to such an invitation, can you? I couldn’t, and I believe this thesis is a result of those early inspirations.

